NOTICE

AVIS

The quality of this microform is heavily dependent upon the quality of the original thesis submitted for microfilming. Every effort has been made to ensure the highest quality of reproduction possible.

If pages are missing, contact the university which granted the degree.

Some pages may have indistinct print especially if the original pages were typed with a poor typewriter ribbon or if the university sent us an inferior photocopy.

Reproduction in full or in part of this microform is governed by the Canadian Copyright Act, R.S.C. 1970, c. C-30, and subsequent amendments.

La qualité de cette microforme dépend grandement de la qualité de la thèse soumise au microfilmage. Nous avons tout fait pour assurer une qualité supérieure de reproduction.

S'il manque des pages, veuillez communiquer avec l'université qui a conféré le grade.

La qualité d'impression de certaines pages peut laisser à désirer, surtout si les pages originales ont été dactylographiées à l'aide d'un ruban usé ou si l'université nous a fait parvenir une photocopie de qualité inférieure.

La reproduction, même partielle, de cette microforme est soumise à la Loi canadienne sur le droit d'auteur, SRC 1970, c. C-30, et ses amendements subséquents.

Canada

Laser Spectroscopic Studies of Hafnium Ions
Confined in a Paul Trap

Wenzheng Zhao, B. Sc. M. Sc

Physics Department
McGill University
Montreal, Canada

A thesis submitted to the Faculty of Graduate Studies and Research
in partial fulfillment of the requirements for the degree of
Doctor of Philosophy

Canada

To my wife, Lili,

for her love

Abstract

A Paul trap has been constructed for laser spectroscopic studies of the isotope shifts (IS) and hyperfine structures (hfs) of radioactive isotopes. With a sample placed near the inner surface of the ring electrode, the target atoms are evaporated by a Nd:YAG laser pulse, and then selectively ionized inside the trap by a synchronized dye laser pulse through resonance ionization spectroscopy (RIS). A cw beam from a ring dye laser is used to probe the ions, and laser-induced fluorescence (LIF) is monitored for spectroscopic measurements. The stored ions can also be analyzed by the ion-ejection time-of-flight spectrum. With an ultra-high vacuum base pressure, Hf ion storage times of one hour can be readily achieved by introducing H_2 as a buffer gas. It is demonstrated that with a very dilute sample, Hf ions can be accumulated in the trap through successive heating and RIS pulses. Through LIF measurements, both the ion cooling time and the dependence of the mean ion kinetic energy on the RF phase and trap operating conditions have been studied. A phase-locked counting technique has been applied to improve the spectroscopic resolution. The hfs of ^{177}Hf and ^{179}Hf with the transition $a\,^2D_{3/2} - z\,^4F^{\circ}_{5/2}$ ($\lambda = 340$ nm) in HfII has been studied with a resolution of about 1 GHz, and their hfs A and B constants have been deduced. The IS of the radioactive ^{172}Hf has been carried out with a sample containing 7×10^{11} ^{172}Hf atoms. Based on the observation of the laser-induced formation of HfH, a new spectroscopic method capable of selectively suppressing the ion population of a particular contaminant isotope has been developed to enhance the ^{172}Hf signal-to-noise ratio. Deduced changes of mean-square nuclear charge radii in Hf, together with the existing data in the literature, are discussed and compared with theoretical variations obtained from Finite-Range Droplet Model calculations.

Résumé

Un piège de Paul a été construit pour étudier les déplacements isotopiques et la structure hyperfine d'isotopes (shf) radioactifs. Les atomes cibles sont évaporés par un laser pulsé Nd:YAG à partir d'un échantillon placé près de la surface interne de l'électrode annulaire et sont ensuite ionisés selectivement par un laser pulsé synchrone par spectroscopie à ionisation résonante (SIR). Un laser en boucle à colorant et à faisceau continu est utilisé pour étudier les ions, la fluorescence induite par le laser (FIL) est utilisée pour les mesures spectroscopiques. Les ions enmagasinnés peuvent aussi être analysés par leur spectre de temps de vol par éjection d'ions. Le système est installé dans une chambre à ultra haut vide. Les ions HF peuvent être facilement capturés pour plus d'une heure en utilisant de l'H_2 comme gaz tampon. Il est démontré qu'avec un échantillon dilué, les ions HF peuvent être accumulés dans le piège par réchauffement et impulsions SIR successifs. Le temps de refroidissement des ions ainsi que l'influence de la phase RF et des conditions d'opération du piège sur l'énergie cinétique moyenne ont été étudié par FIL. Une technique de comptage en phase a été utilisée pour améliorer la résolution spectroscopique. La shf du ^{177}Hf et du ^{179}Hf pour les transitions $a\,^2D_{3/2} - z\,^4F^o_{5/2}$ ($\lambda = 340$ nm) du HfII a été étudié avec une résolution d'environ 1 GHz et leurs constantes de shf A et B ont été déduites. L'étude du DI de l'isotope radioactif ^{172}Hf a été conduite sur un échantillon de 7×10^{11} ^{172}Hf atomes. Sur la base de l'observation de la formation de HfH par induction laser, une nouvelle méthode spectroscopique capable de diminuer selectivement la population d'un isotope contaminant particulier a été developpée pour améliorer le rapport signal sur bruit du ^{172}Hf. Les changements déduits du rayon carré moyen du Hf, combinné avec la littérature existante, sont discutés et comparé avec les variations théoriques du modèle à goutelette à rayon d'action limité.

Claim of Originality

1. Built a unique RFQ (or Paul) trap for laser spectroscopic studies of hyperfine structures (hfs) and isotope shifts (IS) of radioactive isotopes, with the new feature of element-selective ion injection, i. e. only ions of one particular element can be loaded into the trap. In addition, coupling the laser-induced fluorescence measurement and the ion-ejection time-of-flight detection in the same setup has seldom been seen in the literature.

2. Achieved accumulation of ions of a specific element in the RFQ trap from a weak source. This makes it possible to investigate radioactive isotopes of various elements.

3. Investigated kinematics of confined ions in an RFQ trap by LIF and achieved the following new results. (1). The ion cooling time has been directly measured. No or little experimental work has been reported on this subject. The ion cooling time measurement has also been suggested to be a means to study ion-molecule collisions. (2). Systematic studies have been carried out to investigate the RF phase-dependence of the ion momentum spread. The studies suggest that the statistical temperature of an ion cloud, defined by the ion motion at zero RF phase, be relatively constant and slightly higher than the room temperature. However the RF micro-motion of the ions depends strongly on the trap operating conditions. The results are useful to clarify the definition of "ion temperature" currently used in the literature. (3). The effect of space charge on the ion kinematics at different RF phases has been studied. It was found that space charge will modify the shape of the phase-space diagram at different RF phases. The momentum spread at zero RF phase is relatively constant, but the mean kinetic energy of the ions increases with increasing the number of ions trapped.

4. Extracted hfs A and B constants of hafnium isotopes ^{177}Hf and ^{179}Hf for the transition $5d6s^2(a\,^2D)$ ($J = 3/2$) — $5d6s(a\,^3D)6p$ ($z\,^4F°$) ($J = 5/2$) in HfII.

No hfs result in HII has been reported before. The extracted electromagnetic fields at the nucleus provide new atomic data which can be used for the future measurement of nuclear moments of radioactive Hf isotopes through hfs studies of the same transition.

5. Successfully measured radioactive ^{172}Hf with only 20 ions inside the trap. The IS between ^{172}Hf and ^{178}Hf has been deduced reliably. The deduced $\delta < r^2 >^{172,178}$ has updated a previous measured value, revealing a smooth change of nuclear charge radii in Hf isotopes. Previously, a change of the deformation at ^{174}Hf had been inferred.

6. Developed an isotope-selective suppression technique based on our observation of the laser-induced chemical formation of HfH ions due to collisions between H_2 buffer gas and Hf ions in an excited metastable state. This new spectroscopic method has been successfully applied to the measurement of ^{172}Hf. Also the HfH has been found to be able to dissociate with the irradiation of laser beams.

Acknowledgments

I understand that progress of my thesis is inseparable from the contributions of other people, whose efforts I would like to acknowledge. It is a pleasure to express my deepest gratitude to my supervisor Professor Jonathan Lee for his persistent support and guidance in this project. I appreciate his discovery-oriented attitude toward the experimental work. He is quick-minded, and full of good ideas in the experiment. Even while on sabbatical leave in France, he maintained close contact with me and the project. I would also like to thank him for all his concerns to other aspects of my life. My deepest gratitude is also reserved for my co-supervisor Professor John Crawford for his support and guidance through this work. Especially during the absence of my supervisor, he provided me with invaluable help in the project. His help in other different aspects is also acknowledged.

My special thanks goes to Dr. Fritz Buchinger, Dr. Stephan Fedrigo, Dr. Sidney Gulick and Professor Jacques Pinard (Laboratoire Aimé Cotton, Orsay, France). Without their contributions to the project, my progress would have been greatly retarded. I gained a lot from many helpful discussions with them. It is beneficial to share their knowledge and experience. I am grateful for the careful proofreading of my thesis by Dr. Sidney Gulick, which is helpful for my writing the thesis in a second language. I would like thank Dr. Yufeng Ji for his contribution in the initial stage. I would also like to thank Dr. O. Coustantinescu and Dr. M. Hussonois (Institut de Physique Nucléaire, Orsay, France) for their preparation of the ^{172}Hf radioactive sample.

The research has been done in Foster Radiation Laboratory. People here are together like in a big family. I wish to thank Director Jean Barrette for much advice both in my experiment and in my thesis writing, as well as for his concerns with every student of the Laboratory; Professor Bob Moore for his expertise in ion traps; Professor Tommy Mark for his encouragement. My work received technical support from Steve Kecani and Leo Nikkinen, who are without peer in machining work and electronic techniques, respectively. I admire their experience, and would

like to thank them for their assistance. I would also like to thank Stella Laieff for all her help. Acknowledgments are due to many of my fellow graduate students in Foster Radiation Laboratory. In particular, I should thank Roger Lacasse for his translating the abstract of this thesis to French, and for his help in using PAW program for data analysis.

During my PhD studies I was awarded the Carl Reinhardt McGill Major Fellowship and the Alexander McFee Fellowship. I would like to thank Dr. Carl Reinhardt and Dr. Alexander McFee for their great generosity, and their support to my studies.

I also would like to thank my parents, grandparents and my parents-in law for their encouragement and support in my studies. I am indebted to them for their sacrifice suffered for me.

Finally, I must thank my lovely wife Lili, for her love. Without her persistent support and encouragement throughout my studies, I could have accomplished nothing. I also would like to thank her for taking care of me and boosting my morale when some frustrating times occurred. It was due to her great sacrifice that I could more concentrate on my studies and research. I should also thank my lovely son. His unexpected progress often stimulates my spirit.

Contents

List of Tables

List of Figures

Chapter 1

Introduction

Since the first laser was built in the early 1960's, laser applications in various fields have grown very rapidly. Especially after tunable dye lasers of high monochromaticity and high intensity were developed in the early 1970's, spectroscopic studies of atomic transitions started a new era, capable of providing very high precision measurements. Such progress has enabled the laser to play a very important role in nuclear physics studies during the past twenty years. As the nucleus is an inseparable part of an atomic system, much information about nuclei can be obtained by studying the atomic system. One of the very active fields of research is to measure hyperfine structure (hfs) and isotope shifts (IS) over a long chain of isotopes for certain elements. Such measurements are very useful for studies of the systematic variations of the ground state nuclear structures, and are able to give us information about nuclear magnetic and electric moments, nuclear spin and nuclear shapes, all of which are key input parameters for nuclear-model calculations.

So far, about 500 isotopes of more than 30 elements have been investigated in long isotopic chains. Review of the development in laser spectroscopic studies of hfs and IS of radioactive isotopes can be found in references [1, 2, 3] and systematic variations of nuclear charge radii have been compiled in [4]. Most of the experiments were carried out at ISOLDE, CERN using collinear laser spectroscopy, a method independently proposed by Kaufman and Wing [5, 6] in 1976. ISOLDE can deliver many kinds of mass separated short-lived isotopes with adequate intensity for laser spectroscopic studies. In collinear laser spectroscopy, a fast ion beam, or its neutral-

ized atom beam from ISOLDE, interacts with a superposed laser beam, allowing laser spectroscopic studies of isotopes far off stability. Furthermore, the velocity bunching effect can greatly reduce the Doppler width [1], and the relatively long interaction time compared with that in atomic beam laser spectroscopy can enhance the detection sensitivity. Besides collinear laser spectroscopy, on-line resonance ionization spectroscopy (RIS) has been applied in Saint Petersburg to a large number of radioactive rare-earth isotopes [7]. However for those elements which can not be produced as ion beams of adequate intensities, different methods must be developed. One of the approaches to overcome the difficulty is through RIS of laser desorbed radioactive samples to study the "daughter" nuclei from nuclear decay. Such a method has been applied to the studies of the radioactive isotopes of the noble metals Au and Pt performed by McGill University and the University of Mainz [8, 9]. This method still requires an adequate isotopic beam of the "mother" nuclei.

At present, there remain many elements which have not been investigated by laser spectroscopy in a long isotopic chain. The problems we are faced with fall into three categories. First it is very difficult to study light elements for various reasons [10]. Second, refractory elements can not be easily produced in isotope separator. This makes it hard to do systematic studies over that region. Third, transuranium elements constitute another unexplored interesting region due to low production rate. For studies of the nuclides produced at low rates, or from refractory elements, laser spectroscopy employing a radio-frequency quadrupole (RFQ or Paul) ion trap could be more suitable. The RFQ trap was invented in 1958 by Paul [11]. It is a convenient and useful device capable of storing charged particles for extended periods within an isolated space, using a relatively weak confining electric field. This unique characteristic allows a wide range of applications in various scientific fields. In particular, since these confined ions can interact continuously with an externally applied electromagnetic field such as that of a laser beam or an RF source, the Paul trap offers an environment for experiments that require extreme precision or sensitivity. With its inherent sensitivity, only a small number of trapped ions is needed for a measurement. Detection of a single confined ion has been demonstrated [12], and very precise

frequency measurements of atomic transitions have been performed [13, 14, 15]. A survey of work in the field of the physics of trapped ions can be found in [16, 17].

Although laser spectroscopic studies have been performed in traps since early 1977 [18], such measurements on radioactive isotopes have not been started until recently. The first candidates have been radioactive Hf and Th isotopes [19, 20]. In these works, the isotopes were introduced into a Paul trap by evaporating the samples on a tantalum wire and ionizing them by an electron beam. The ions were stored for an extended period of time in the trap and probed by an incident laser beam or beams. For the Th ions, sub-Doppler resolution was obtained by using a two-step excitation scheme. A drawback of this approach is that electron beam ionization is non-selective and many kinds of contaminant ions can be produced and trapped at the same time due to a poor mass selectivity of the Paul trap. With a weak source, it could be difficult to inject a sufficient number of ions of interest into the trap for spectroscopic measurements.

In this work, our goal was to develop a system employing an RFQ trap for laser spectroscopic studies of radioactive elements. First of all, a new method for ion production and accumulation inside the trap has been introduced. A Nd:YAG laser is used to desorb the target material and subsequently the RIS process is employed to selectively ionize atoms of a specific element directly inside a trap. Both ion-ejection time-of-flight detection and laser-induced fluorescence (LIF) measurement have been incorporated in the setup. The whole system must be maintained in an ultra-high vacuum system in order to have a long ion storage time.

Our ion injection method was first tested as an efficient way to load Mg^+ ions from the impurities of $CaCO_3$ in our early experiment [21]. Later with improved storage time of trapped ions, it was proved that with successive laser pulses, ions of interest can be accumulated inside trap from a weak or dilute source. In principle, this new ion injection method would make it possible to perform laser spectroscopic studies of many un-investigated isotopes including both refractory and transuranium elements.

In most laser spectroscopic work, the spectral resolution in RFQ traps is lim-

ited by Doppler broadening due to the ion motion under the driving RF field. This problem can be partly solved by a modulated laser beam used by Rink *et al.* to excite the ions at a certain RF phase to improve the spectral resolution [19]. In our work, a simple way to suppress the spectral linewidth by a coincident counting technique has been implemented and compared to the laser modulation method. In the course of improving optical resolution, many studies have been done to understand the trapped ion kinematics. The ion cooling time with a buffer gas has been measured. The space charge effect at different RF phases has been observed by the phase-selective LIF method. And systematic studies of the spectral linewidth reveal some important properties of the ion motion inside the trap.

Several factors were considered when Hf was chosen as a candidate in my research. Hafnium, as a refractory element, is a well deformed element, lying in a very interesting mass region for nuclear physics studies. In particular, a unique isomer ^{178}Hf^{m2} ($T_{1/2}$ =31 y) with high nuclear spin I=16 is very interesting for nuclear studies. Recently a lot of efforts have been made to study this isomer [22, 23] in our collaboration. In the production of ^{178}Hf^{m2}, some other Hf radioactive isotopes were also produced. Through international collaboration, it was possible for us to get radioactive Hf samples to test our setup. Furthermore, there were no published results measuring ^{177}Hf and ^{179}Hf hyperfine splitting in Hf ionic states. Some new estimates of the electromagnetic field at the nucleus through hfs studies could be expected from our work.

In our experiment, stable Hf isotopes were studied first, including the hfs studies of ^{177}Hf and ^{179}Hf of the transition $a\,^2D_{3/2} - z\,^4F^o_{5/2}$ ($\lambda = 340$ nm) in HfII. Then a sample containing 7×10^{11} atoms of radioactive isotope ^{172}Hf was used to further prove the feasibility of our setup for radioactive isotope studies. In addition, during our laser spectroscopic studies, it was very interesting to have observed a laser-induced chemical process leading to the formation of HfH. Based on this fact, selective suppression of contaminant stable Hf isotopes was developed and successfully applied in the measurement of ^{172}Hf to enhance the weak ^{172}Hf signal.

In this thesis the experimental setup will be described in Chapter 2, followed

by three chapters on the development of the experimental methods and some new results concerning spectroscopic techniques and trapped ion kinematics. Chapter 3 is about the general operation of the system; Chapter 4 the development of the isotope-selective suppression method; Chapter 5 the Doppler width reduction. Starting from Chapter 6, three consecutive chapters will present the results about hfs of ^{177}Hf and ^{179}Hf isotopes; the measurement of radioactive ^{172}Hf isotope and the resultant changes of nuclear charge radii in Hf. The thesis ends with the conclusions in Chapter 9. Appendix A gives some parameters in the Finite-Range Droplet Model for calculating mean-square nuclear charge radii.

Chapter 2

Experimental Apparatus

In this chapter our experimental setup is discussed. After some knowledge of RFQ traps, the layout of the experiment setup followed by detailed description about each individual unit will be presented.

2.1 Introduction to RFQ Traps

A quadrupole field is characterized by its linear dependence on the co-ordinate position. In the Cartesian co-ordinates x, y and z

$$E = E_0 \left(\lambda x i + \sigma y j + \gamma z z \right) \tag{2.1}$$

where λ, σ and γ are weighting constants, E_0 is a position-independent factor which may be a function of time, and i, j and k are the unit vectors in the x, y and z directions, respectively. The field is subject to the restraints imposed by Laplace's equation

$$\nabla \cdot E = 0 \tag{2.2}$$

so that

$$\lambda + \sigma + \gamma = 0 \tag{2.3}$$

In a quadrupole ion trap,

$$\lambda = \sigma, \gamma = -2\lambda \tag{2.4}$$

The potential ϕ can be expressed by

$$\phi = -\frac{1}{2} E_0 \lambda (x^2 + y^2 - 2z^2) \tag{2.5}$$

6

In order to produce such a field, the quadrupole ion trap device consists of three electrodes of three-dimension-rotational symmetry, illustrated in Fig. 2.1. The two
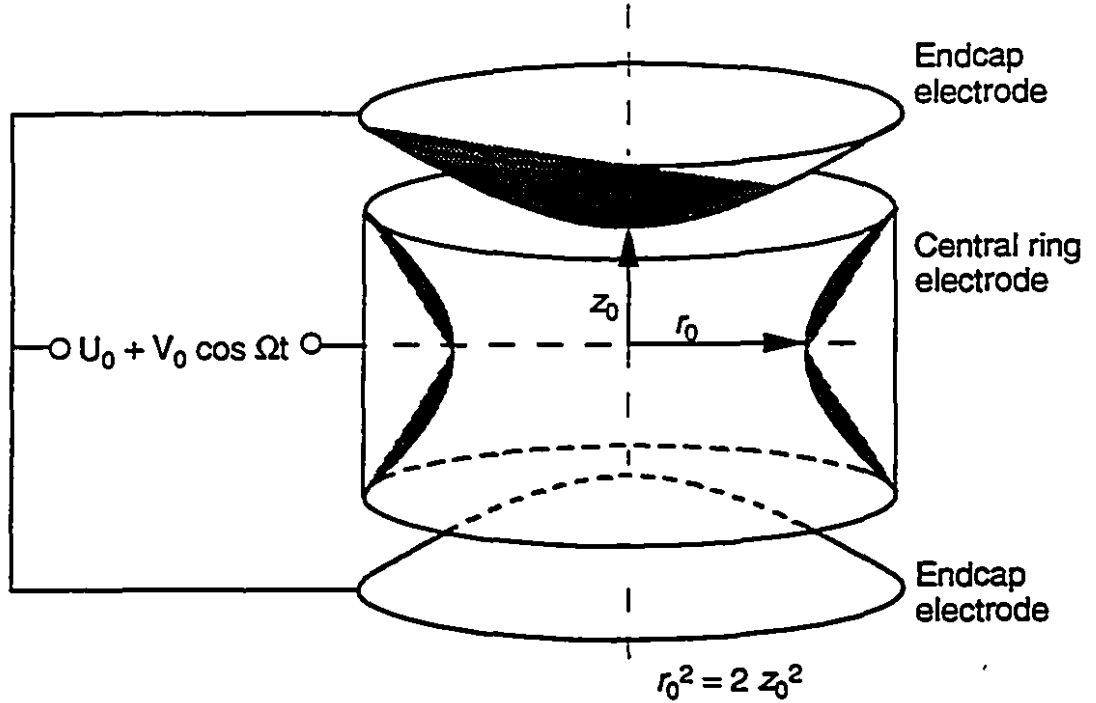
Figure 2.1: An RFQ trap.

"end-caps" and the ring electrode have cross-sections in the rz plane which are complementary hyperbolae. Typically (but not necessarily), $r_0^2 = 2z_0^2$, in which $2z_0$ is the separation along the z-axis between the two endcap electrodes. A Paul or RFQ trap operates under pure electric radio-frequency quadrupole field. Frequently, it is convenient to operate the RFQ trap with the end-caps grounded, so that only a single potential $U(t)$ need be applied to the ring (see Fig 2.1)

$$U(t) = U_0 + V_0 \cos\Omega t \qquad (2.6)$$

where Ω is the angular frequency of the RF voltage, U_0 is the dc voltage, and V_0 is the amplitude of the RF voltage. Thus the potential in the trap could be more properly represented as

$$\phi = \frac{U(t)(x^2 + y^2 - 2z^2)}{2r_0^2} + \frac{U(t)}{2} \qquad (2.7)$$

The equations of motion are given by $m\ddot{r} = eE_r$ and so on. That is

$$\ddot{z} - (2e/mr_0^2)(U_0 + V_0\cos\Omega t)z = 0 \tag{2.8}$$

$$\ddot{r} + (e/mr_0^2)(U_0 + V_0\cos\Omega t)r = 0 \tag{2.9}$$

Defining trapping parameters

$$a_z = -2a_r = -\frac{8eU_0}{mr_0^2\Omega^2} = -\frac{4eU_0}{mz_0^2\Omega^2} \tag{2.10}$$

and

$$q_z = -2q_r = \frac{4eV_0}{mr_0^2\Omega^2} = \frac{2eV_0}{mz_0^2\Omega^2} \tag{2.11}$$

and expressing time in terms of the parameter ξ where $\xi = \Omega t/2$, both equations of motion reduce to the general form

$$\frac{d^2u}{d\xi^2} + (a_u - 2q_u\cos 2\xi)u = 0 \tag{2.12}$$

where u represents either r or z.

These equations are of Mathieu type and an understanding of quadrupole ion trap demands some knowledge of the properties of the Mathieu equation. Simple analytical expressions for the solutions of this equation are not available. Solutions to the equation can be expressed in the form

$$u(\xi) = \alpha e^{\mu\xi}\sum_{n=-\infty}^{\infty} C_{2n}e^{2in\xi} + \alpha' e^{-\mu\xi}\sum_{n=-\infty}^{\infty} C_{2n}e^{-2in\xi} \tag{2.13}$$

The parameters α and α' depend on the initial conditions, C_{2n} and μ independent of these conditions but depend only on a_u and q_u [24, 25]. The term μ is referred to as the characteristic exponent and its value determines the type of the solution to the Mathieu equation. There are two type of solutions, one stable and one unstable. The stable trajectories of ions come from solutions where $\mu = i\beta$ is purely imaginary and β is not a whole number.

Fig. 2.2 shows a stability diagram in the a_z-q_z plane of the Mathieu equation for simultaneous confinement of ions in the r and z directions. The lines are contours of constant β; the stable region is bounded by the limiting values $\beta_{z,r} = 1, 0$ and contains the (a_u, q_u) area in which μ is purely imaginary. There is thus a wide range
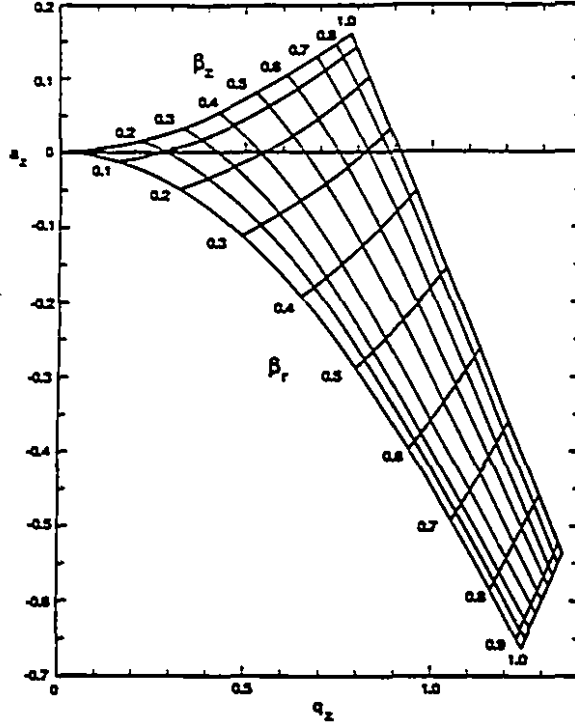
Figure 2.2: Mathieu stability diagram in three dimensions.

of a_u and q_u conditions where ions formed within the quadrupole ion trap might be expected to have stable trajectories and remain trapped indefinitely unless their trajectories are perturbed by collisions.

In the stable region, ion trajectories may be expressed as a linear combination of sine and cosine elliptic series

$$u(\xi) = A \sum_{n=-\infty}^{\infty} C_{2n} \cos(2n + \beta_u)\xi + B \sum_{n=-\infty}^{\infty} C_{2n} \sin(2n + \beta_u)\xi \qquad (2.14)$$

For small a_u and q_u, the the amplitudes of higher-frequency components are small compared with those at the fundamental ($n=0$) frequency ω_0

$$\omega_{u,0} = \beta_u(\Omega/2), \qquad \beta_u = \left(a_u + \frac{q_u^2}{2}\right)^{1/2} \qquad (2.15)$$

The high-frequency oscillating terms in the ion trajectory may therefore be neglected if β_u is small, and the resulting ion trajectory may be written simply as

$$u(t) \approx A \cos\omega_{u,0}t + B \sin\omega_{u,0}t \qquad (2.16)$$

9

We can see that it satisfies the equation

$$\frac{d^2 u}{dt^2} + \omega_{u,0}^2 u = 0 \tag{2.17}$$

The above two equations describe simple harmonic oscillation along the u-axis, a trajectory followed by a particle subject to a potential that varies quadratically with u. For a single ion trapped in a Paul trap, the approximate experienced field can be derived from a pseudopotential, Φ_0, which comes from the static potential from both dc voltage and average effect of the RF voltage. We may calculate the pseudopotential, Φ_0 [26, 27]

$$
\begin{aligned}
\Phi_0(x, y, z) &= \frac{m}{2e}\left(\frac{\Omega}{2}\right)^2 \left(a_r + \frac{q_r^2}{2}\right)(x^2 + y^2) \\
&\quad + \frac{m}{2e}\left(\frac{\Omega}{2}\right)^2 (-2a_r + 2q_r^2)z^2 + \text{constant} \tag{2.18} \\
&= D_r \frac{r^2}{r_0^2} + D_z \frac{z^2}{z_0^2} + \text{constant} \tag{2.19}
\end{aligned}
$$

in which

$$D_r = \frac{mr_0^2}{2e}\left(\frac{\Omega}{2}\right)^2 \left(a_r + \frac{q_r^2}{2}\right) \tag{2.20}$$

and

$$D_z = \frac{mz_0^2}{2e}\left(\frac{\Omega}{2}\right)^2 (-2a_r + 2q_r^2) \tag{2.21}$$

D_r and D_z represent the pseudopotential well depth in the radial and axial directions, respectively.

2.2 Experimental Setup

2.2.1 Apparatus Layout

The general experimental layout is schematically shown in Fig. 2.3. The trap is placed inside an ultra-high vacuum chamber. In the trap electrodes, holes have been drilled for laser beams to pass through as well as for ion ejection and photon collection. A sample target is placed close to the inner edge of the bottom hole in the ring electrode. Pulses from a Nd:YAG laser pass through the top hole and vaporize the sample material into the trap center. Synchronized RIS laser pulses pass through the

10
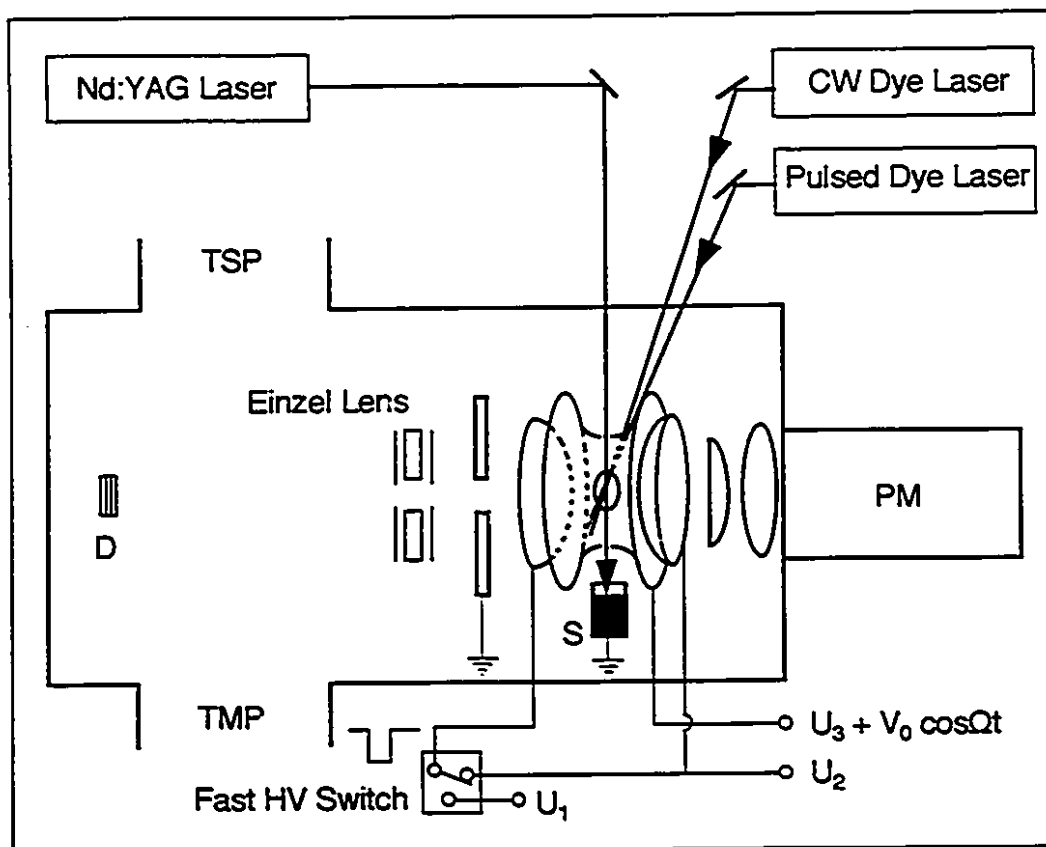
Figure 2.3: Schematic diagram of the experimental set up, S: Target with sample; D: Micro-channel Plate Detector; PM: Photomultiplier; TSP: Titanium Sublimation Pump; TMP: Turbo-molecular Pump; L: Optical lenses. The RIS and cw laser beams are perpendicular to the YAG beam and pass through the horizontal pair of holes.

horizontal holes on the ring electrode and selectively ionize a chosen element. Due to the electric potential applied to the electrodes, ions within a certain charge-to-mass ratio range will follow various stable trajectories and be trapped.

On one side of the ion trap, there is an ion-ejection time-of-flight detection system. Trapped ions can be extracted by applying a negative pulse on the extraction electrode. They are focused by an Einzel lens before hitting the micro-channel plate (MCP) detector. The time-of-flight spectrum registered gives information about the mass distribution of the trapped ions. On the other side of the trap, there are lenses and optical filters as well as a photomultiplier for fluorescence detection. A cw dye

laser beam, passing through the horizontal holes, can be used to probe the trapped ions. By scanning the cw dye laser wavelength across a resonance transition, the laser-induced fluorescence spectrum of the trapped ions can be obtained. With sufficient spectral resolution, it is possible to measure hyperfine structures and isotope shifts.

The whole vacuum chamber is made of stainless steel, which is bakeable to 400°C. The system is pumped by a turbo-molecular pump (TMP), supplemented by a titanium sublimation pump (TSP). The base pressure is better than 5×10^{-8} Pa after one day bakeout at 200°C. The system can also allow to feed clean buffer gas into the chamber.

In the following sections, a detailed description of different parts in our setup will be given.

2.2.2 The RFQ Trap

The RFQ trap and its electronic driving circuit are illustrated in Fig. 2.4. The trap
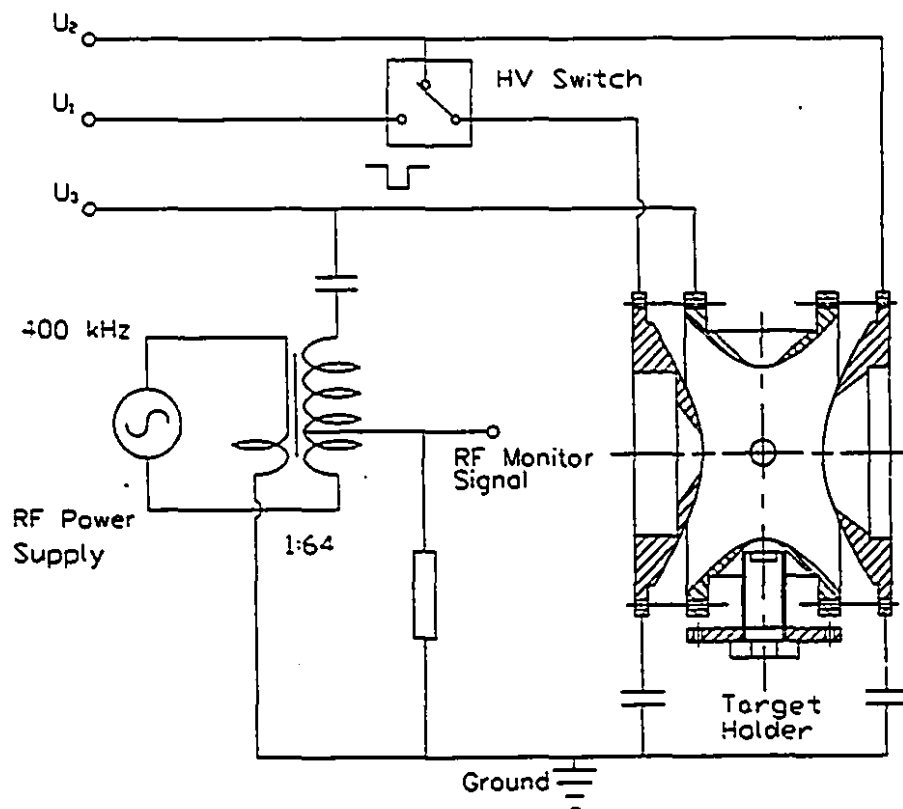
Figure 2.4: Trap assembly and its electronic driving circuit diagram.

12

consists of three main electrodes of hyperbolic shape: a central ring of radius $r_0 = 20.3$ mm and two end-caps separated by $2z_0 = 28.7$ mm ($r_0 = \sqrt{2}\,z_0$). On the ring electrode, four holes of 6.4 mm diameter are bored along the radial directions perpendicular to each other to let the laser beams pass through. Holes are also bored along the axial direction in the end-caps. For the ion extraction, a hole 10 mm in diameter is drilled in the center of one of the endcaps. For the fluorescence photon collection, a large solid angle is necessary. A hole 26 mm in diameter is drilled on the other endcap. These holes in the endcaps are then covered by stainless steel mesh to preserve the hyperbolic shape of the electrodes.

The trap assembly is normally floated about 900 V above ground potential to facilitate the ion-ejection time-of-flight detection. For such a purpose, three different dc outputs U_1, U_2 and U_3 are produced through a series of resistance dividers by using a dc power supply. To operate the RFQ trap, a suitable radio-frequency voltage $V_0 \cos\Omega t$ as well as a dc bias $U_0 = U_3 - U_2$ need to be applied to the ring electrode, where RF voltage is coupled with the dc voltage U_3 through a capacitor. U_0 can be adjusted to be either positive or negative, which together with the RF amplitude V_0 will determine the trap parameters a_z and q_z given by eqn. (2.10) and eqn. (2.11). Here U_1 is only used for ion extraction, described in section 2.2.5. In the system, the electronic components are placed outside the vacuum chamber. All three trap electrodes of the ion trap are separately connected to ultrahigh vacuum feedthroughs using stainless steel wires.

Typically, the trap is operated at an RF voltage with a peak amplitude V_0 of 440 V at frequency of 400 kHz and a dc offset voltage of 15 volts. This gives a trap pseudopotential well depth of about 13 eV for the axial motion and 18 eV for the radial motion for hafnium ions. The schematic diagram for the RF voltage supply is also shown in Fig. 2.4. The output from the RF power amplifier (EIN 325LA 50W/50Ω) is coupled to a transformer with a ferrite core to produce the RF voltage needed. On the primary side there is only one turn. 64 turns have been wound on the secondary side. An RF signal after the first turn in the secondary side is used to monitor the RF voltage and phase.

It should be mentioned that the circuit on the secondary side of the transformer is an *LC* resonant circuit. The inductance *L* comes from the transformer coil. The capacitor *C* is from the trap itself as well as the coaxial cable connecting the output of the transformer and the ring electrode. In resonance the equivalent impedance reaches a maximum, resulting in a high gain for the output voltage of the transformer. The length of the coaxial cable has been chosen so that the resonance frequency is around 400 kHz.

In Fig. 2.4 the target holder is also shown. The sample is located very close to the inner surface of the ring electrode and is maintained at ground potential. This arrangement prevents unwanted ions produced by laser desorption from entering the trap.

2.2.3 Ultra-High Vacuum System

Fig. 2.5 shows the vacuum system. The main vacuum chamber consists of two 6-way 8″ (20.3 cm) crosses sealed with Conflat flanges. The chamber is pumped by a turbo-molecular pump (Balzers TPU180H) with a pumping speed 180 L/s backed by a mechanical pump (Leybold-Heraeus D16A). From the manufacturer's specifications, the ultimate pressure of this pump can reach below 1×10^{-8} Pa.

In addition, a Mini titanium ball from Varian is installed in the vacuum system to effectively pump the residual reactive gases. When the titanium ball is heated at a high electric current (about 45 A), the sublimated titanium atoms coat the surface of the inner wall of the vacuum chamber. When the active molecules in the chamber collide with this fresh titanium coating, they react with the titanium and the produced compounds stick to the wall [28]. At room temperature, a typical pumping speed per square centimeter of titanium sublimation surface for O_2 is 10 L/s. In our design the net pumping speed for active gases is over 1000 L/s, considering that the usable speed is reduced by the conductance between the pumping area and the location of the work.

The stainless steel buffer gas inlet lines are also shown in Fig 2.5. A research grade hydrogen with purity (99.9995%) is used in our experiment as the buffer gas.

14
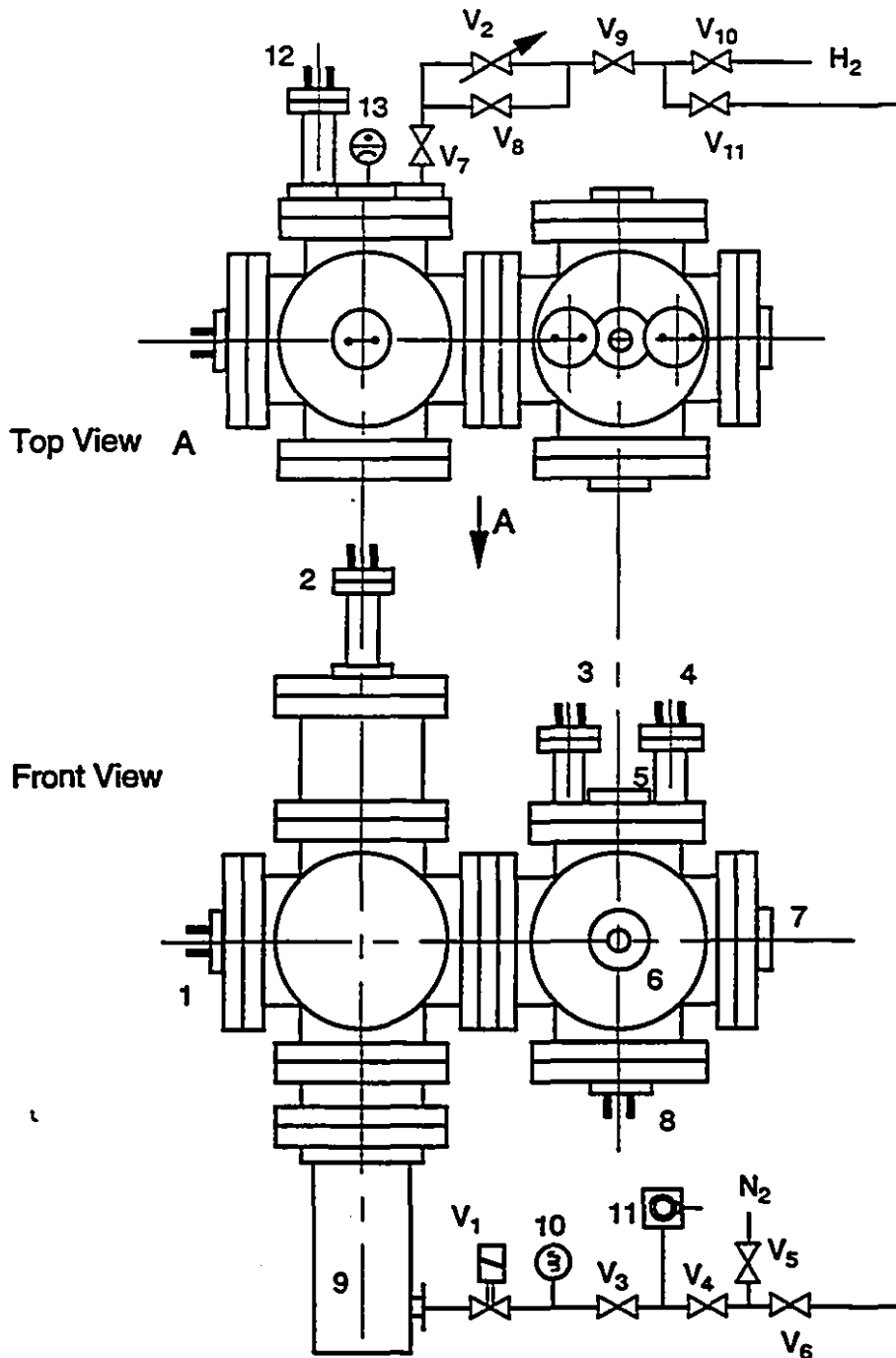
Figure 2.5: Vacuum pumping and buffer gas feeding system. 1. FT for MCP; 2. FT for TSP; 3. FT for internal lamps; 4. FT for thermal couple; 5. VP for Nd:YAG laser; 6. VP for RIS laser and cw laser; 7. VP for photon collection; 8. FT for trap; 9. TMP; 10. TC gauge; 11. MP; 12. FT for RGA; 13. Vacuum Gauge, where FT = feedthroughs and VP = viewport.

The chamber can be pumped all the way up to the high pressure gas regulator valve by the turbo-molecular pump, with valve V11 closed. To introduce the buffer gas, valve V8 is closed and the buffer gas can feed through the needle valve V2. The buffer gas line is also used to purge dry nitrogen when the system needs to be shut down.

Inside the vacuum chamber, all the metal pieces are made of stainless steel and the insulators are made of machinable ceramic. The material of the optical lenses used is fused silica. When screws are used to fix different components, blind holes have been avoided. All the parts in this system including viewports are bakeable to 450 C°. The turbo-molecular pump can be baked to 100°C with the supplied heat jacket. In fact the turbo-molecular pump itself is a weak point for bakeout. The rotor temperature should not exceed 200°C due to radiation from the vacuum chamber during the bakeout. Before the system was assembled, all the pieces were cleaned with acetone and alcohol. Then most of them were preheated in the air at 275 C° for about 10 hours to reduce the outgassing of the stainless steel surfaces [28].

The system can be baked both outside and inside. The outside baking employs heating tapes. Five 500-Watt heating tapes are wrapped onto aluminum sheet which is directly put onto the outside of the vacuum chamber in order that the heating energy may be more uniformly distributed. Another sheet of aluminum foil is wrapped outside to cover the heating tapes to reduce the heat radiation loss. The applied voltage to the heating tapes is adjusted by a Variac. Inside the vacuum chamber, four 300-Watt halogen lamps have been installed. The lamps serve not only as an inside heating source, but also as a light source to illuminate the target. The voltage applied to the lamps is also adjustable. Another inside heating source is the titanium ball, which can be set at a stand-by condition during the bakeout with only an infinitesimal sublimation of titanium.

Pumping down the system starts with turning on the turbo-molecular pump and mechanical pump simultaneously. When the turbo-molecular pump accelerates to the normal speed, the pressure is about 2×10^{-3} Pa. The system is gradually heated and is kept at 200 °C for bakeout. Baking the system with a hydrogen pressure of

10^{-3} Pa has found to accelerate the outgassing of the system. When the system reaches 200 °C, the hydrogen buffer gas can be fed into the vacuum chamber. After about 12 hours, heating is removed and at the same time the hydrogen feeding is stopped. The system will have a pressure below 5×10^{-8} Pa after about four-hour cooling down. When the base pressure has been achieved, the titanium sublimation pump can be applied with an electric current of 45 Amp for about 30 min to produce a fresh coating of titanium on the surrounding inner surface of the vacuum chamber. This coating will remain active for many hours, since our base pressure is so low.

When the system was first baked without introducing any buffer gas, a residual gas analyzer showed that the main residual gases inside the system were H_2, H_2O, CO, and some CO_2. These are typical outgases from a stainless steel surface [28].

2.2.4 Laser System

There are several lasers in our setup. A Nd:YAG laser is used as a desorption laser to evaporate the sample materials. Subsequently a pulsed dye laser pumped by an Excimer laser is used to resonantly ionize the atoms of interest with high efficiency. The probing beam from a cw ring dye laser pumped by an Ar^+ laser excites the confined ions and yields a LIF measurement.

JK Lasers System 2000 Nd:YAG laser provides the heating source to vaporize the target material. The laser produces an infrared (1.06 μm) pulse of about 10 ns. A rotatable polarizer is mounted outside the laser to attenuate the laser pulse energy. After focusing with a suitable lens, the laser beam passes through the top vacuum sapphire viewport and hits the target material. A video camera is mounted to monitor the position of the laser spot on the target substrate.

The pulsed dye laser (Lambda FL2002) is pumped by a XeCl excimer laser (Lambda EMG201MSC). The pulse energy of the pump laser can be as high as 400 mJ with wavelength 308 nm. Using various dyes, the pulsed dye laser can produce coherent laser radiation at any wavelength from 340 nm to near-infrared with pulse energy of a few times 10 mJ. The tuning range can be extended into the ultraviolet (uv) by using frequency doubling crystals, with a conversion efficiency about 10%.

17

The size of the laser beam is about 3 mm in diameter when it reaches the trap system. Two sapphire viewports are used for laser beams to enter into and exit from the system.

Since the Nd:YAG laser desorbed atoms take time to reach the trap center for laser photoionization, the trigger of the excimer laser should be delayed for a suitable time interval after the Nd:YAG Q-switch pulse. A master trigger generator plus four-channel delay unit has been built for our experiment to control the lasers as well as ion ejection. All the output triggers are synchronized to the RF signal to permit study of RF phase-sensitive process. In our setup, a master trigger goes to the Nd:YAG flash lamp and its repetition rate can be adjusted from 0.5 Hz to 10 Hz. Two delayed synchronized outputs are sent to trigger the Nd:YAG Q-switch and the excimer laser.

The Coherent CR-699-21 ring dye laser is pumped by a Coherent Innova CR-12 Ar^+ ion laser. In laser spectroscopic measurement of the confined ions in the trap, the ionic transition is investigated. Therefore, cw uv laser radiation produced through second harmonic generation (SHG) is often required. Internal frequency doubling can enhance the SHG efficiency because of higher fundamental laser power density inside the ring dye laser cavity. Fig. 2.6 schematically shows the cw laser diagram
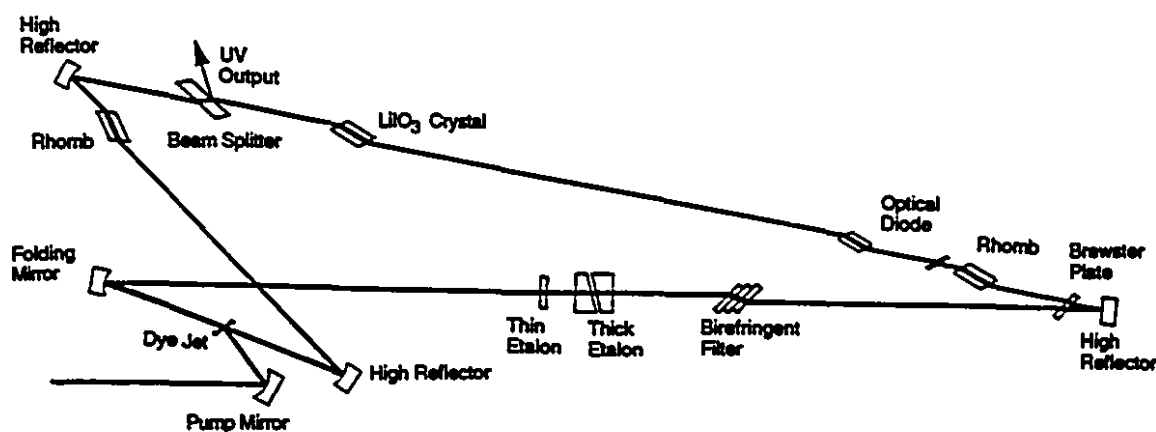
Figure 2.6: A cw laser schematic diagram with an intra-cavity frequency doubler.

including the intra-cavity frequency doubler. The uv laser beam produced from the

frequency doubler reflects from the beam splitter, and can further be separated from the remaining fundamental laser light by prisms.

For our Hf experiments, cw uv laser radiation with wavelength of 340 nm is needed. This radiation is produced using a DCM dye and $LiIO_3$ doubling crystal. The dye recipe used is prepared with the following procedures: (1) dilute 1.0 gram DCM in 400 ml Benzyl Alcohol; (2) mix 500 ml ethylene glycol with 200 ml glycerol; (3) add 350 ml of the dye mixture into the ethylene glycol mixture; (4) circulate the dye mixture in the dye module utility. In the first three steps, the solution needs to be mixed very well with an ultra-sonic agitator in order to achieve a good performance of the ring dye laser. Use of DCM laser dye with the $LiIO_3$ doubling crystal provides a tuning range from 318 nm to 350 nm with output uv power about 4 mW. The typical size of the laser beam at our trap system is about 2 mm in diameter.

An LM 0202 laser modulator makes it possible to produce laser pulses synchronized with the RF phase in order to investigate the phase-locked excitation. To modulate the laser light to excite the ions within a very short interval (100 ns) at a specific RF phase, a fast HV switch synchronized with the RF signal is used.

2.2.5 Ion Extraction and Detection System

For observation of the ions inside the trap, ion ejection from the trap and time-of-flight detection has been designed in our system. This provides a convenient way to examine the mass distributions inside the trap.

As discussed before, the trap assembly is floated about 900 V above ground potential. When a negative pulse is applied to the extraction endcap, the ions inside the trap are accelerated toward the extraction endcap. Passing through the mesh hole in the endcap, they further accelerate under the electric field between the ground plate and the endcap (see Fig. 2.3). Afterward the ions are focused by the Einzel Lens and drift toward the micro-channel plate detector. The distance between the trap center and the detector is about 40 cm. Ions with different masses will reach the micro-channel plate at different times, yielding a time-of-flight spectrum. The signal from the detector goes through a preamplifier ($\times 10$) and the output is recorded by

a digital scope.
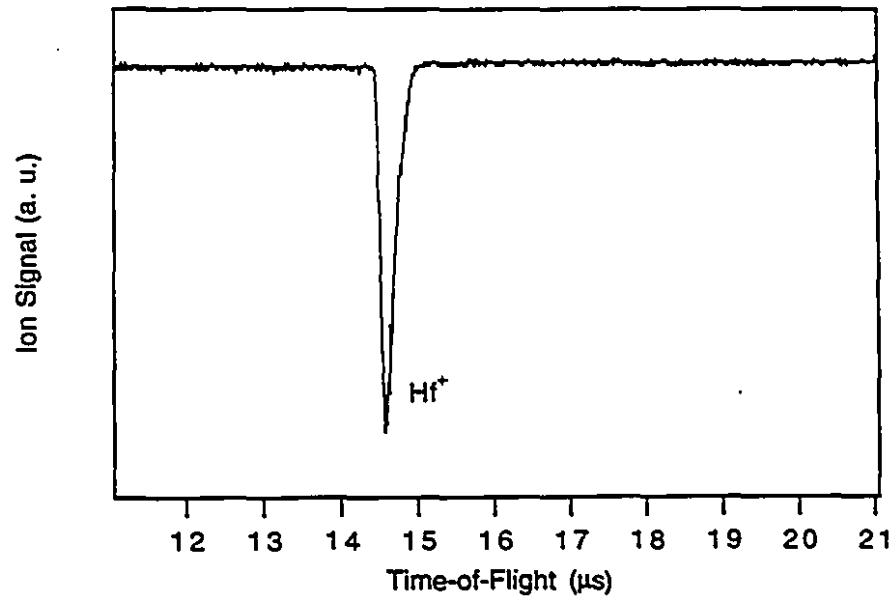
Figure 2.7: Typical time-of-flight spectrum of ejected hafnium ions.

Two micro-channel plates are stacked in the detector. In the mechanical design, the plates are held in place by three ceramic rods on the sides together with two metal plates on the both ends. Typically $U = 1.5$ kV is applied to the detector, and half of this voltage is across each micro-channel plate. The typical gain of the detector is about 10^6. A single ion produces a short pulse (less than 10 ns) with an area about 20 pVs. Thus the number of ions trapped can be estimated from the area of the ejected time-of-flight signals.

A time delay unit is used to control the time interval between the ion injection and ion extraction. The end of this time interval initiates a phase-locked ejection pulse, which triggers a high voltage switch and produces a negative pulse on the endcap. The ejection timing with respect to the RF phase is found to greatly affect the time-of-flight spectrum due to the interaction between the extraction and RF fields inside the trap [29]. Therefore, the timing of the phase-locked ejection trigger pulse should be first adjusted to optimize the time-of-flight spectrum.

Fig. 2.7 is a typical time-of-flight spectrum. It is a hafnium ion signal extracted

after the ions have stayed in the trap for 1 second. The typical spectrum resolution ($M/\Delta M$) is about 60, which is good enough for our purpose. This medium resolution is limited by the fact that our time-of-flight drift zone is very short. In addition, the initial ion cloud has a certain distribution in space, resulting in an initial energy spread in the extracted ions.

2.2.6 Laser-Induced Fluorescence Counting and Data Acquisition

The LIF detection is the core of the setup, since the final goal is to study the isotope shifts and hyperfine structures from the LIF spectrum. For fluorescence detection, signal to background ratio is always important. This has been kept in mind in designing the fluorescent collection system—to increase the photon counting signal and suppress the background count.

An RCA 8850 photomultiplier (PM) is used to detect the fluorescent light. The PM is placed outside the ultrahigh vacuum chamber, 200 mm away from the trap center. The photocathode of this photomultiplier is 45 mm in diameter. Two synthetic fused silica lenses make up the photon collection system. One is a plano-convex lens of 40 mm in diameter with focal length f= 50 mm and the other is symmetry-convex lens of 50 mm in diameter with $f = 75$ mm (at wavelength 546.1 nm). The optical components have been drawn to scale in Fig. 2.8. In the design, the first lens is put as close as possible to the trap center, resulting in a solid angle of 6%. The position of the second lens has been optimized through computation, so that photomultiplier cathode can receive all that passes through the first lens, emitted from the trap central region with 6 mm in size.

The background usually comes from two sources. One is the scattering light from the laser beam, and the other is due to the photomultiplier dark current. Typically a voltage of about 1.6 kV is applied between the anode and the photocathode. The dark current counting rate of the photomultiplier is about 180 cps.

In our Hf work, cw uv radiation at 340 nm is used to excite the transition $5d6s^2(a\,^2D)$ ($J = 3/2$) — $5d6s(a\,^3D)6p$ ($z\,^4F^\circ$) ($J = 5/2$) in HfII. The optical

21
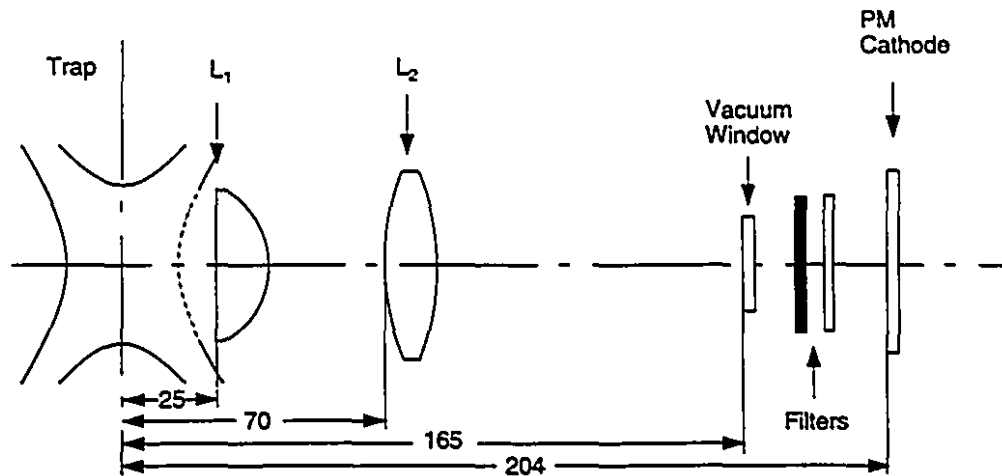
Figure 2.S: Fluorescence photon collection system.

excitation scheme for HfII has been given in Fig. 2.9. There are two strong photon de-exciting channels from the z $^4\mathrm{F}^\circ$ level to the two metastable states $5d6s^2$ ($a\,^2\mathrm{D}$) ($J = 5/2$) and $5d^2(a\,^3\mathrm{F})6s$ ($a\,^4\mathrm{F}$) ($J = 3/2$) with wavelengths of 380 nm and 388 nm respectively. Hydrogen buffer gas can effectively quench these metastable states back to the ground state, so that the excitation cycle can be repeated. A filter from Oriel Corp. (Filter 59463) is used to suppress the scattering photons from the incident cw uv light. A UG5 filter suppresses all the visible background. The filter transmission efficiency curves are given in Fig. 2.10.

A schematic diagram of the data acquisition system is shown in Fig. 2.11. In the LIF measurement, the wavemeter can read the laser wavelength to an accuracy of 0.01 cm^{-1}. A confocal etalon (150 MHz) and spectrum analyzer (1500 MHz) are used to check the laser performance and calibrate the laser scanning range. The cw uv beam is guided into the trap center to probe the trapped ions. The laser modulator permits phase-locked excitation as discussed in section 2.2.4

The de-excitation fluorescence photon signal from the photomultiplier passes a preamplifier and a fast amplifier. The output is then sent to a discriminator. The photon count output is send to a CAMAC counter model. RF synchronized inhibit

22
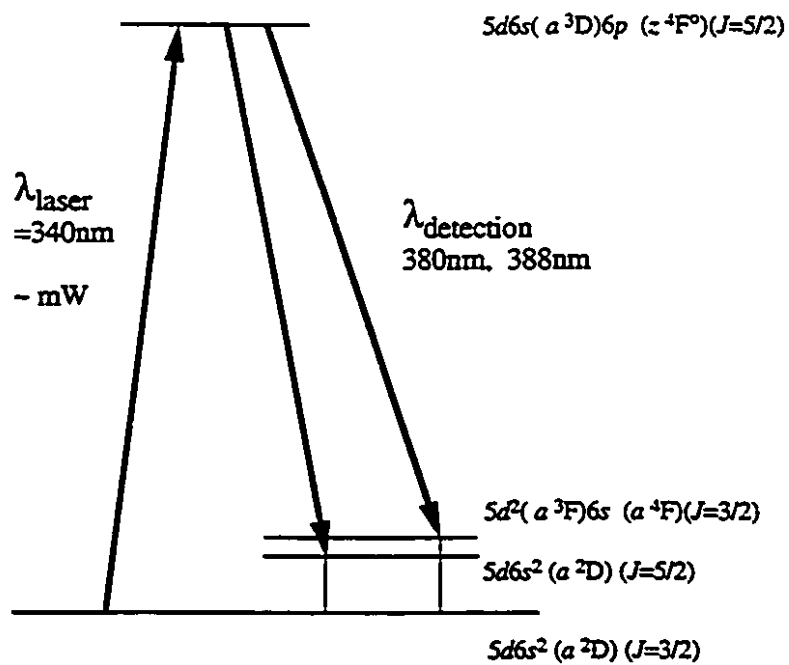
Figure 2.9: Laser excitation scheme in HfII.
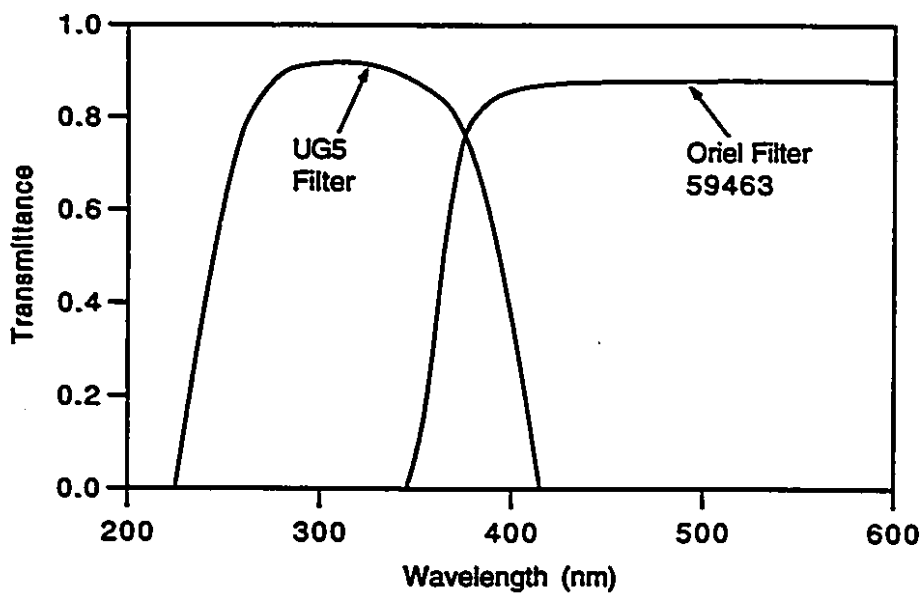
Figure 2.10: Transmission efficiency curves of optical filters.
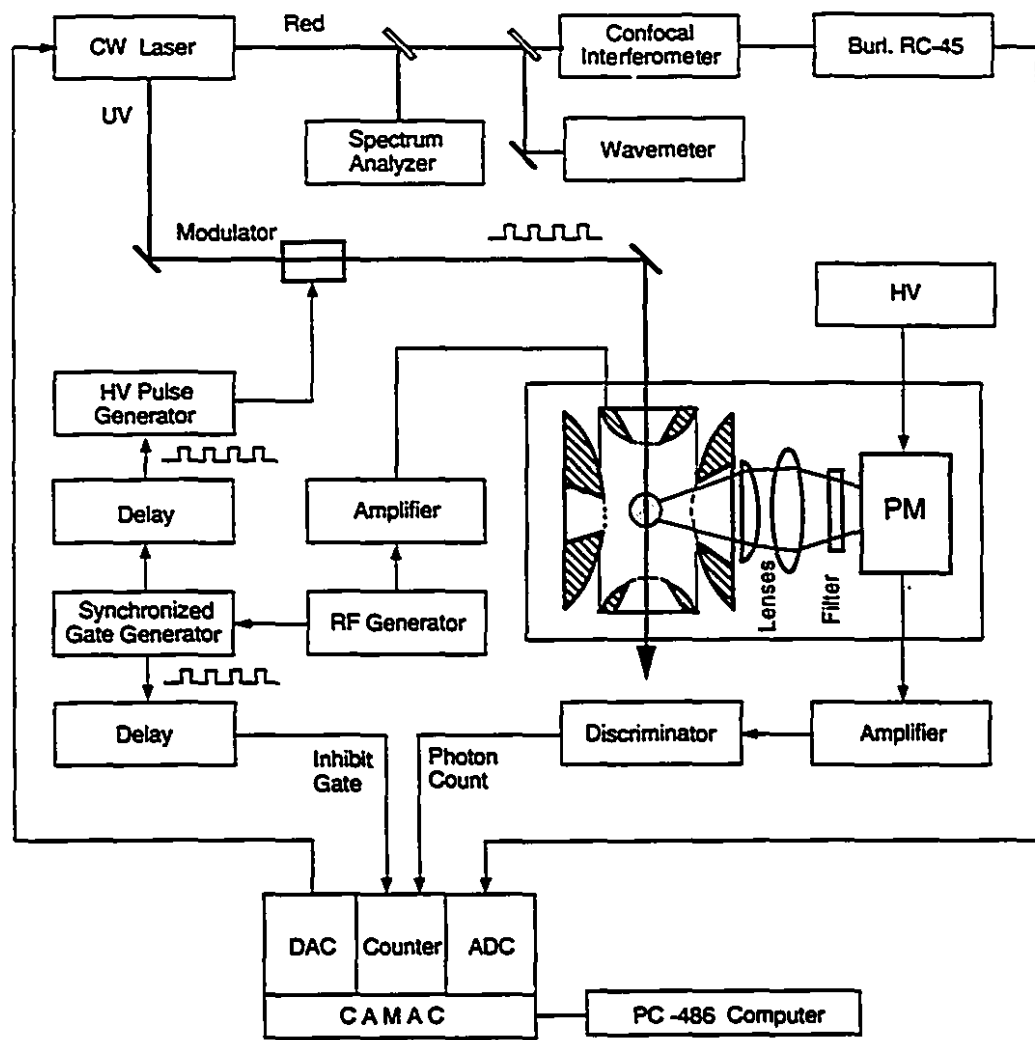
Figure 2.11: Schematic diagram for laser spectroscopic measurement with trapped ions.

signals allow phase-locked coincidence counting measurements. The CAMAC system is controlled by a PC-486 computer. Besides the counter module, the computer also controls an ADC and a DAC module. The DAC output gives a stepped dc voltage to drive the scanning of the cw laser. Between each step, there is a time delay, which is usually set to be 125 ms. This delay time can be changed when needed. The ADC module is used for recording the interference patterns from the confocal etalon, which provides a calibration curve for the scanning range. At each step the ADC output and photon counts are displayed on the screen. The laser scan can be repeated many times. The photon counts and the ADC data for each scan are stored as a file. The program also records the sum of all the individual scans.

Chapter 3

Ion Storage and Detection

In the previous chapter, the features of the experimental apparatus have been presented. The internal ion production through Nd:YAG and RIS pulses is expected to efficiently load the ions of interest into the trap. Then the trapped ions can be detected by either ion ejection time-of-flight spectrum or LIF measurement. In this chapter, the performance of the system from the ion injection to ion detection will be examined. Some interesting results including ion accumulation and buffer gas cooling will be presented.

3.1 Ion Production

3.1.1 Nd:YAG Desorption

In our ion injection scheme, a Nd:YAG laser beam (1.06 μm) is used to evaporate neutral Hf atoms out of the target substrate, then the desorbed atoms can be resonantly ionized and trapped. Generally the laser desorption process depends on the laser intensity on the target substrate. At high laser intensity ($\geq 10^9$ W/cm^2), micro plasmas are created and a large part of the material taken out of the surface is ionized. At a slightly lower laser flux (10^6 W/cm$^2 - 10^8$ W/cm^2), the desorbed material is mostly in the neutral atomic or molecular form. In our studies, the goal of laser desorption is to get as many neutral Hf atoms out of a target substrate as possible while avoiding direct produced contaminant ions.

In the experiment, three different kinds of targets have been used, such as metallic hafnium foil, HfO$_2$ powders and trace quantities of HfCl$_4$ (lower to 10^{12}

molecules). It is trivial to desorb Hf atoms out of a metallic foil. In the other two cases the samples are deposited on a substrate. Since hafnium is a refractory element, it requires a relatively high laser intensity to efficiently desorb neutral Hf atoms from the samples deposited on the substrate. However the threshold for the ion production from the target substrate itself is generally lower. Therefore the substrate material needs to be chosen so that it has a high threshold for plasma production. In our experiments we have tried stainless steel and graphite substrates. It has been found that the threshold for plasma production is much higher for graphite than for stainless steel. In the studies of dilute Hf samples, graphite substrates were always used.

Even though the graphite substrate has a higher threshold, it has been found the threshold for producing carbon cluster ions is still lower than that for efficient neutral hafnium desorption. In order to increase the laser power to vaporize the Hf atoms and repel the directly produced contaminant ions away from the trap, the target substrate is kept at ground potential while the trap assembly is floated about 900 V above the ground.

Two methods are used in the experiment to examine whether the Nd:YAG laser power is at a suitable level. One way is to check the RF monitor signal. If too many background ions are produced by laser desorption, the RF voltage will be distorted due to a big change of the effective load in the RF circuit. The other way is to monitor the micro-channel plate signals just after the Nd:YAG pulse. A burst of signal will appear when the trapping condition is killed. To maximize the Hf atom desorption, the Nd:YAG laser power need to be kept just below the threshold above which the trapping condition can not maintain.

The desorption laser intensity can be adjusted by directly changing the laser pulsed energy, laser repetition rate or focusing condition. The output power of the Nd:YAG laser can be adjusted by varying the discharge voltage displayed in the laser control panel. In addition, the rotatable polarizer can be used to attenuate the infrared Nd:YAG laser pulse energy. It has been found that the focusing condition of the laser beam is very critical. A weakly focused desorption laser beam on the target can allow more laser power to be used while keeping the same threshold. In this way

27

more neutral Hf atoms can be desorbed out of the target substrate. But it is very hard to monitor the Nd:YAG laser spot on the target with the weak focusing. When working with a radioactive sample, we need to know where the laser hits the target to avoid destroying the sample before any measurement can be done. A compromised focusing condition has been used in our experiments to deal with the radioactive ^{172}Hf sample.

3.1.2 Resonance Ionization

Resonance ionization spectroscopy is a very sensitive and selective photoionization method [30, 31, 32]. In RIS, atoms from a specific element are brought up by one or a series of resonant transitions to a high-lying excited state from which they can be ionized by further excitation to a level beyond the ionization limit. The excitation between the discrete states is easily saturated because of the high excitation cross-section around 10^{-14} cm^2. But the final ionization step is a discrete state to continuum transition, which has a much smaller cross-section even in the most favorable cases where we can tune the ionizing laser to arrive at an auto-ionizing state in the continuum. Higher laser pulse energy of the final step is usually needed to enhance the ionization efficiency.

The RIS scheme of Hf is shown in Fig. 3.1. To produce Hf ions through the RIS process, the pulsed dye laser (with dye LC5400) pumped by the excimer laser is used. A uv laser pulse with wavelength 271 nm after the frequency doubling is for the first excitation step a ^{3}F$_2$ ($E = 0$ cm^{-1}) — z ^{5}P$_1^\circ$ ($E = 36949.29$ cm^{-1}). The green fundamental beam of about 10 mJ per pulse is used as the second ionization step. The ionization level of HfI has been determined as 55 047.9(3) cm^{-1} by double-resonance, field ionization spectroscopy [33]. Our RIS laser beams excite the Hf atom only 376 cm^{-1} above the ionization threshold, which is the free-electron energy E_e after the resonance ionization. From [34], it is known that the photoionization cross-section is inversely proportional to the square root of the free-electron energy

$$\sigma \propto \frac{\hbar \omega_2}{c \left[2 m_e E_e\right]^{1/2}} \tag{3.1}$$

28
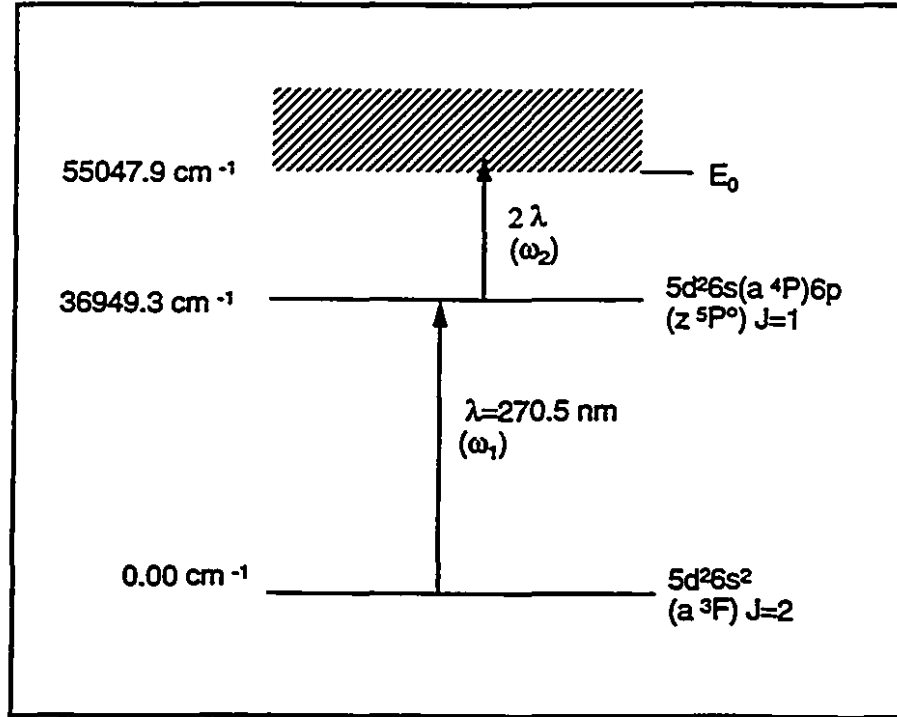
Figure 3.1: Hf resonance ionization scheme used in the experiment.

where m_e is the electron mass. From eqn (3.1), it can be expected that the ionization efficiency is high since the final continuous state is just above the ionization limit.

In the laser desorption and RIS, after the neutral atoms are desorbed out of the target, some will move into the trap. A delay between the RIS laser and the YAG laser pulses is necessary to allow the atoms to travel from the target substrate to the trap center. By adjusting the delay time and monitoring the output from the MCP detector, the maximum ion production was found to correspond to a delay of about 25 μs between the triggers of the excimer laser and Nd:YAG Q-switch.

From the manufacturer's specifications, the pulsed dye laser linewidth is about 6 GHz. Therefore, the frequency doubled uv light will have a linewidth of 12 GHz. Furthermore, the resonance excitation transition can be broadened by the strong laser power. With the uv pulse energy 0.5 mJ, the resonance width is found as wide as 0.01 nm (40 GHz), which will cover the transition frequencies of different Hf

isotopes. When dealing with a radioactive Hf isotope, we don't need to worry about the isotope shift for RIS. On the other hand, this could be a drawback of our ion injection method, since it can select elements of interest, but not distinguish between isotopes.

3.2 Ion Storage Time and Chemical Reaction inside the Trap

In our approach, the ions are created inside the trap along the RIS laser beam path with well defined thermal velocities. These ions occupy only a small phase-space volume, and will be trapped with a high efficiency. Since the ions are produced only via the element selective RIS process, a cloud of pure Hf ions can be expected to be stored inside the trap. Ideally, an ion pursuing a stable orbit within the trap will continue to do so indefinitely. However, in an actual system an ion is expected to suffer collisions with other ions and neutral background particles in the trap. In this work, factors affecting the ion lifetime have been studied and some measures have been taken to assure a long storage time, which can make it possible to accumulate ions from a weak source. In the experiment, time-of-flight detection is used to investigate the storage time. After the ions were loaded into the trap, they were allowed to stay in the trap for a certain time. Then ejected time-of-flight spectra gave us information about the mass distribution of ions inside the trap.

To achieve long storage time, an ultra-high vacuum system in the chamber is essential to reduce ion-molecule collisions. Before a thorough bakeout process, our system could achieve a base pressure of 10^{-6} Pa. Under these conditions, the Hf ion storage time was less than one minute. The time-of-flight spectrum showed that within this period, most of the Hf ions were converted into heavier molecular ions, presumably HfO, HfOH and HfO_2 ions, through ion-molecule collisions inside the trap. This chemical reactive process is very common for many elements. We have found similar reactions for elements such as Th, Ba and Ta ions, though Cs ions, because of their noble gas configuration, are much less reactive and can remain unchanged for a much longer time.

30

After the vacuum system was baked out thoroughly at 200°C, a base pressure of less than 5×10^{-8} Pa was readily obtained. At the base pressure, time-of-flight spectra obtained after more than one hour of storage time showed predominantly pure Hf ions, with only small contaminant of HfO and HfOH ions. However the number of ions trapped decreases with time. Fig. 3.2 gives us the ion signals versus the time
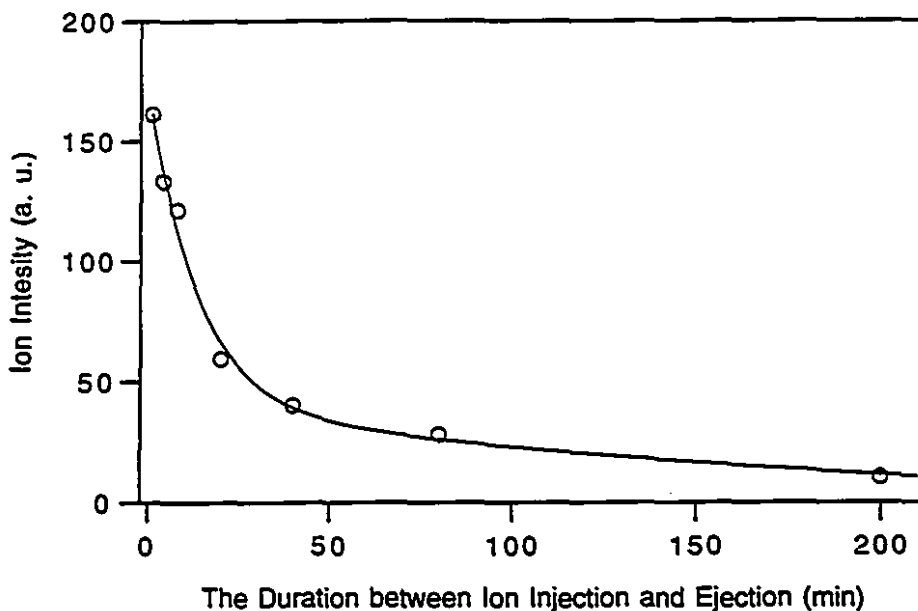
Figure 3.2: Ejected Hf^+ ion intensity after certain storage time. Each time it started from a fully loaded trap. The measurement was done at the base pressure less than 5×10^{-8} Pa.

interval between the ion loading and ion extraction. It is found that the number of ions in the trap decays with a fast time constant $\tau = 14$ min followed by a slow component longer than $\tau = 4$ hours. This indicates that without buffer gas cooling, the ions may be lost from the trap due to interactions with residual gas molecules as well as the RF heating effect. The fast decay can be explained by an "evaporating cooling" process [35], in which the most energetic ions are lost from the trap and the kinetic energy of the remaining ion cloud decreases.

For ion cooling purposes, any light gas, such as H_2 and He, would do the job. However hydrogen as a diatomic molecule is also very effective to quench the low-

31

energy metastable states for laser spectroscopic measurements. Therefore hydrogen is used as a buffer gas in our experiment. When first introduced with a pressure of 10^{-3} Pa, the hydrogen buffer gas was found to accelerate the conversion of Hf^+ into heavier molecular ions, limiting the storage time of pure Hf^+ to minutes. The RGA shows a big increase of the content of H_2O, CO, CO_2. Efforts to purify the feeding hydrogen gas made little improvement. The increase of contaminants can be explained by the fact that the hydrogen gas can desorb some gases from the inner walls of the vacuum chamber. With this clue we have found an efficient way to clean the vacuum chamber by baking the vacuum chamber under a hydrogen pressure of about 10^{-3} Pa. The trap storage time can be further improved by operating the Ti sublimation pump, and by switching off all vacuum gauges. After the above procedures, the residual gas contents were greatly suppressed. However we have found that while a trap operated with hydrogen buffer gas can store ions for several days, chemical processes caused by ion-molecule collisions still limit the effective Hf ion half-life to about one hour with our present setup. Fig. 3.3 shows typical time-of-flight spectra after a short time (1s) and a long time (40 min) of ion storage. It indicates that while ions are staying in the trap some of the Hf ions will be converted into heavier molecules due to chemical reactions of Hf with the residual reactive gases in the vacuum chamber. It should be mentioned that the effective storage time of Hf^+ in the trap is not improved if helium is used as the buffer gas.

3.3   Ion Accumulation

In studies of radioactive isotopes, the sample provided is often very dilute. With each ion production sequence of Nd:YAG desorption followed by RIS pulses, the number of ions produced can be very low. It would be very useful if ions could be accumulated in the trap from repeated laser pulses. With hydrogen buffer gas (10^{-3} Pa) to cool the ions produced, the phase-space volume of trapped ions can be reduced in a few tens of milliseconds through buffer gas collisions (see section 3.4). Therefore the ions produced from subsequent laser pulses should be trapped until all the phase space volume has been occupied. In our previous work [21], we have suggested that this
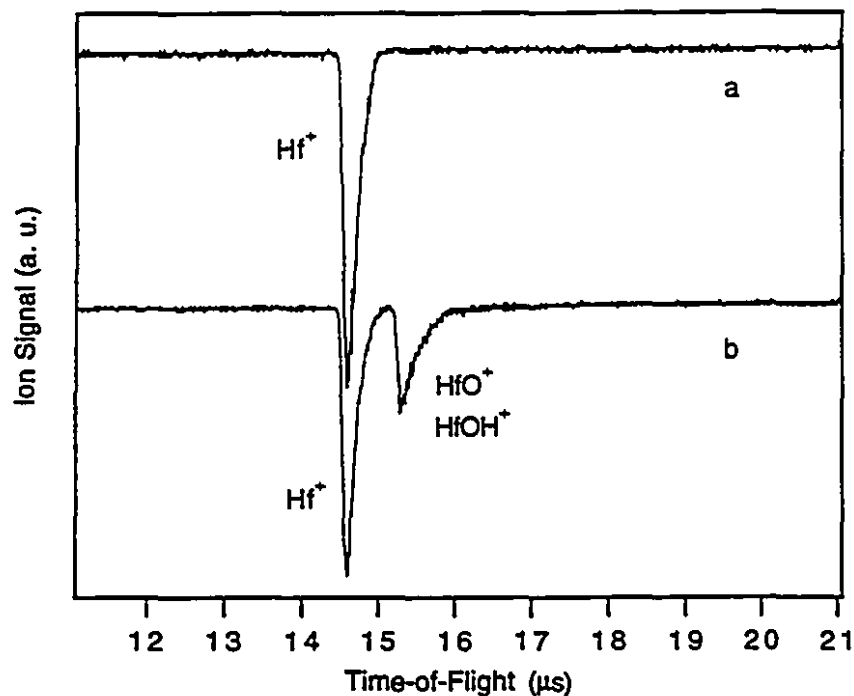
Figure 3.3: Time-of-flight spectra of ejected ions, (a): after stored in the trap for 1 s, (b): after stored in the trap for 40 minutes. The hydrogen buffer gas pressure is 10^{-3} Pa. The time-of-flight spectrum after long ion storage shows that some of Hf ions have converted to heavier molecules due to chemical reactions of Hf ions with residual reactive gases in the vacuum chamber.

ion injection method should be applicable to a very weak source.

Ion accumulation from a weak source has been tried. Optical detection of the trapped ions, as a non-destructive method, has been used to monitor the ion accumulation process. For LIF detection of Hf ions, the optical excitation scheme as shown in Fig. 2.9 is used. The cw laser beam needs first to be tuned at 340 nm, corresponding to the ionic transition $a\,^2$D ($J = 3/2$) — $z\,^4$F° ($J = 5/2$) of one of the Hf isotopes, for example, ^{178}Hf. The LIF photons are detected by the photomultiplier.

A dilute source was prepared by putting a drop of methanol solution containing about 10^{14} HfCl$_4$ molecules onto a graphite substrate surface, which is 6 mm in diameter. By using repeated Nd:YAG desorption and RIS pulses, the ion accumulation from successive shots is demonstrated in Fig. 3.4. The LIF from the ions inside the trap was continuously monitored while the ions were produced by heating and
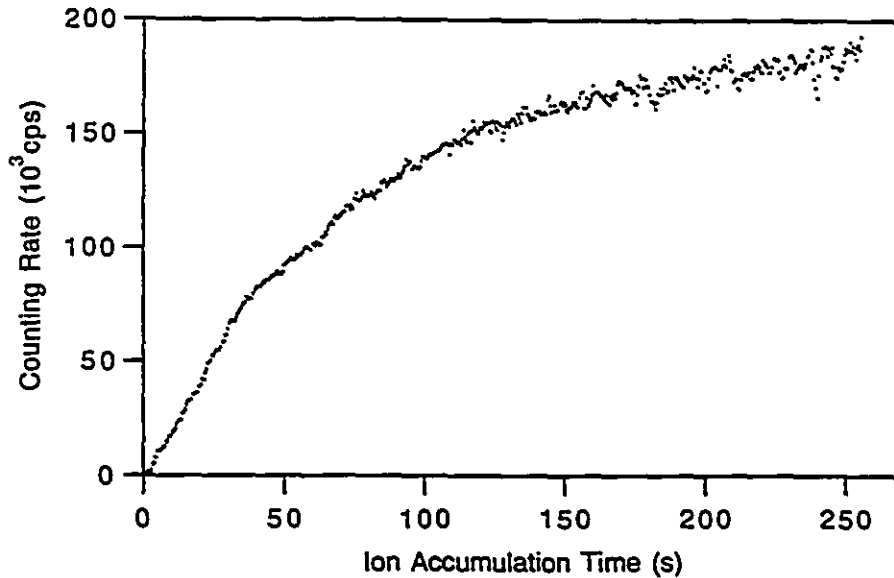
Figure 3.4: The laser-induced fluorescence versus the ion accumulation time. The Nd:YAG laser and the pulsed dye laser operated at a repetition rate of 2 Hz. The buffer gas pressure was 9×10^{-4} Pa.

RIS laser shots. The experimental data indicate that the number of ions trapped first increases with the number of shots and gradually reaches a saturation level. With the sample described above, the saturated level corresponds to a few 10^4 ions. However with more dilute samples (10^{12}), the maximum number of ions that can be accumulated in the trap is often much lower. This is not surprising, since in the accumulation process a burst of neutral particles produced by each heating pulse is delivered towards the center of the trap; this can destabilize the stored Hf ions through collisions. The eventual maximum number of accumulated ions is therefore governed by the relative ion production and ion leakage rate.

3.4 Buffer Gas Cooling Time

Light gases are often used as a buffer gas to cool down the ions in the ion trap. Reduction of the ion energy by a factor of three could be achieved [36]. However, little or no experimental work has been reported measuring buffer gas cooling time.

34

In this work, efforts have been made to measure the ion cooling time. Such studies can provide valuable information to understand the ion cooling mechanism, and would be useful for designing and operating Paul trap-related transportation and collection systems. In addition, the measurement of ion cooling time can also help to study ion-molecule collisions.

In the experiment, the Hf ions are created instantaneously along the RIS laser beam path. Their initial trajectories occupy a large spatial volume of the trap, and through collisions with the buffer gas molecules, the ions are cooled and subsequently migrate towards the center of the trap. We have experimentally measured this cooling time. With the cw dye laser tuned to the resonant wavelength and probing only the center of the trap, the increase of the LIF counting rate after the RIS pulse has been monitored. The increase of the LIF counting rate after a RIS pulse has the form

$$1 - exp(-t/\tau) \tag{3.2}$$

where τ can be interpreted as the ion cooling time. A typical counting rate variation with hydrogen pressure at 4.2×10^{-3} Pa is shown in Fig. 3.5(a). The cooling time thus deduced at different buffer gas pressures is shown in Fig. 3.5(b), indicating an inverse proportionality with the buffer gas pressure. This suggests that the cooling rate (τ^{-1}) varies linearly with the buffer gas density, thus the collision frequency. As discussed in [37], prior to equilibrium, the overall effect of collisions with light buffer gases is to lower the mean kinetic energy of the ions, and the RF heating effect during the initial cooling process will be small. Assuming that the fractional energy loss per collision is determined by the mass ratio $m(H_2)/m(Hf)$ [38, 39], the cooling rate can be approximated by

$$\tau^{-1} = R \ m(H_2)/m(Hf) = n_b v \sigma \ m(H_2)/m(Hf) \tag{3.3}$$

where R is the collision rate, n_b is the buffer gas density, v is the mean relative velocity between ions and molecules and σ is the collision cross section. From Fig. 3.5(b), we can see that at a hydrogen pressure of 5×10^{-3} Pa the cooling time is about 50 ms, resulting in a collision rate R of 1780/s. Now a collision cross section of Hf$^+$ ions relative to hydrogen molecules can be estimated. Hydrogen molecules at 300 K have
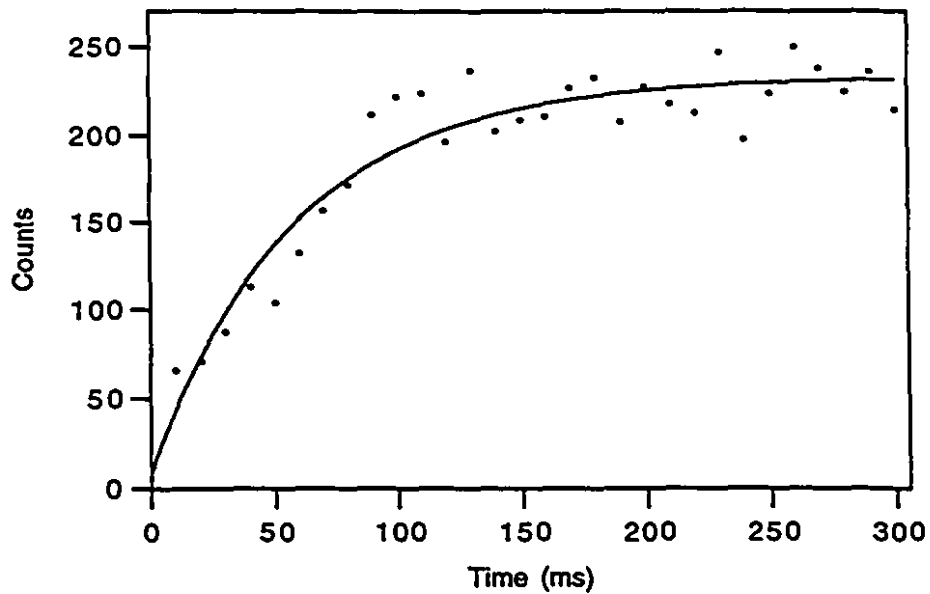
(a). Observed LIF counts increase with time due to the hydrogen buffer gas cooling at a pressure of 4.2×10^{-3} Pa.
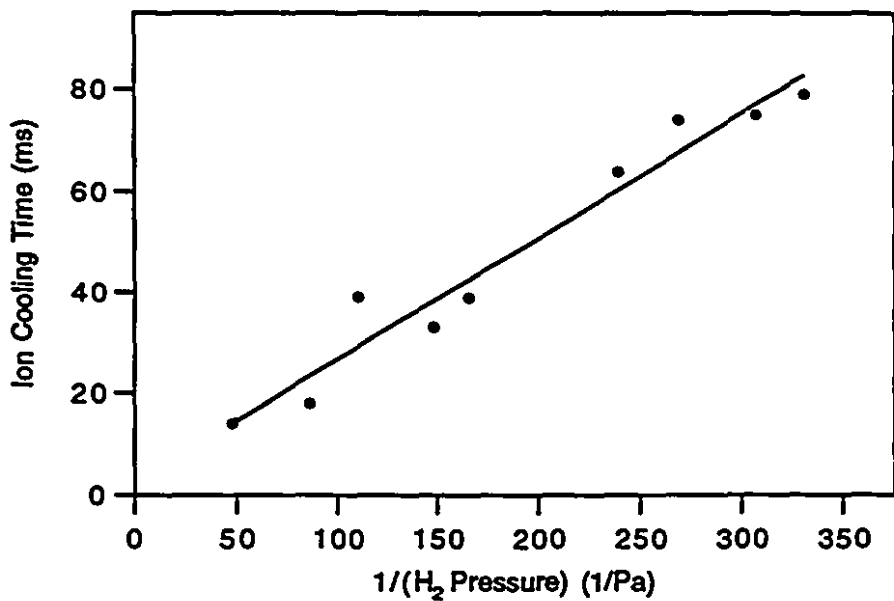
(b). Ion cooling times at different buffer gas pressures.

Figure 3.5: Ion cooling times at different buffer gas pressures.

a mean velocity of 1.8×10^5 cm/s and a density n_b of 1.2×10^{12} /cm^3. The effective trap depth of our present system is 13 eV. Before cooling, Hf$^+$ ions should have an energy of 1.3 eV [36] and a velocity of the order of 10^5 cm/s. Since the hydrogen velocity is bigger than the velocity of Hf$^+$ ions, the mean relative velocity does not vary much during the cooling down process and v is assumed to be 2×10^5 cm/s. The experimental results thus yield a cross section σ of 8×10^{-15} cm^2. This value can be compared with the calculated classical ion-molecule collision cross section of hydrogen gas relative to Ba$^+$, which is 7×10^{-15} cm^2 [40].

3.5   Summary

It has been found that chemical reactions between hafnium ions and residual gas molecules is an important factor limiting ion storage times. In our setup, hafnium ion storage times of longer than one hour have been achieved. It is long enough for the ion accumulation and the spectroscopic measurement. With repeated Nd:YAG laser desorption and RIS laser pulses, the ions of interest can be successfully accumulated inside the trap from a dilute source. This is a big step toward laser spectroscopic studies of radioactive isotopes. Furthermore, the buffer gas cooling times in the trap has been measured for the first time. This is an important parameter for the studies of kinematics of the trapped ions.

Chapter 4

Laser-Induced Chemical Reaction and Isotope-Selective Suppression

While continuously monitoring LIF of the confined Hf ions with the cw uv laser, it was found that the photon counting rate suffered from a fast decay much shorter than the ion storage time in the trap. In this chapter, we will present our experimental observations and our deduction that this decay is due to optically induced chemical reaction of Hf ions with hydrogen buffer gas molecules to form HfH^+. This can result in a decrease of pure Hf ions inside the trap available for laser spectroscopic measurements. It has also been found that the HfH molecules can be dissociated by uv laser irradiation. Based on these observations, an isotope-selective suppression method has been developed, which can be used to enhance weak signals in laser spectroscopic measurements.

4.1 Optical Pumping-Induced HfH^+ Formation

During laser spectroscopic measurement with the trapped ions, a laser beam is continuously interacting with the ion cloud. It is different from the laser spectroscopy of atom beams or ion beams, in which the interaction time is quite short and fresh species are continuously being supplied for interaction with the laser beams. Here the fresh species refer to those atoms or ions which are susceptible for laser excitations. In the ion trap, long interaction between laser light and the confined ions can change the population distribution dramatically, even if there is a very weak branch which

can "trap" the Hf$^+$ in some forms of metastable states. Therefore, optical pumping effect in the trap could become an important aspect. In this work we have observed a chemical reaction channel to form HfH$^+$ when the hafnium ions are continuously irradiated by resonance probing cw uv beam. This light-induced chemical process can have a strong influence on the LIF signals observed from the trapped Hf ions.

4.1.1 Experiment Evidence for HfH Formation

Using LIF to observe the ion accumulation has been presented in section 2.2.6. In principal, we can also observe the storage time of Hf$^+$ ions in the trap by monitoring the LIF continuously. This provides a nondestructive method to see how the number of ions of interest are changing with the time. Such measurements have been carried out and some interesting phenomena related to a laser-induced chemical process have been observed.

In the experiment, an enriched ^{178}HfO$_2$ sample was used. After ^{178}Hf$^+$ ions were loaded into the trap, the cw uv light was switched on to continuously excite those Hf$^+$ ions. The LIF counts were recorded and Fig. 4.1 displays a typical result, indicating a fast drop in the first few minutes ($\tau = 1.7$ min) followed by a slow component ($\tau = 52$ min). The slow decay is related to the ion storage time which is limited by the chemical reactions of Hf$^+$ ions with the residual gas contaminants as discussed in section 3.2. The nature of the fast decay is not immediately apparent. Additional experiments were then carried out.

First when monitoring the LIF counting rate in the fast decay region, instead of continuous irradiation, the cw laser light was blocked for certain periods of time. The counting rate does not drop during the period the cw laser light is blocked as shown in Fig. 4.2. From this, one can conclude that the decrease in the signal is optical pumping related. On the other hand, the laser light was blocked during the slow decreasing period. The LIF counting rate continues to decrease, as shown in Fig. 4.3. If the fast decay of the LIF signal is due to the ions pumped to some long-lived metastable states in Hf$^+$, a certain amount of ions in those states should be quenched back to the ground state by collisions with hydrogen buffer gas during the
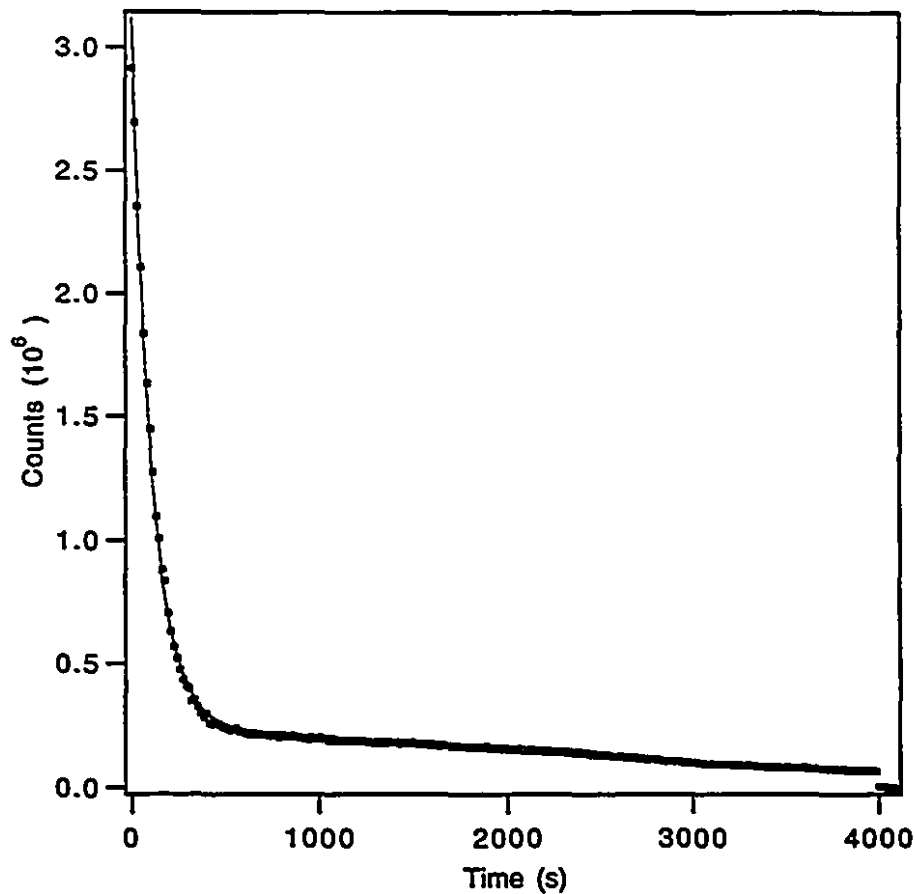
Figure 4.1: Typical fluorescence decay with a continuous resonance uv excitation.

period of the blockage of cw uv beam. The absence of quenching through collision implies that the effect is not due to a long-lived metastable state in Hf^+.

These observations strongly suggest that this fast drop in LIF signal be due to the conversion of Hf^+ to other kinds of molecular ions induced by laser excitation. The time-of-flight spectra of the extracted ions, with and without undergoing laser excitation, were then obtained and are shown in Fig. 4.4. The upper trace is from the trapped Hf ions which were produced in the trap and left in there without undergoing excitation by $\lambda = 340$ nm. The leading peak is due to Hf ions, and the second peak is corresponding to hafnium oxides as discussed in section 3.2. The lower trace of
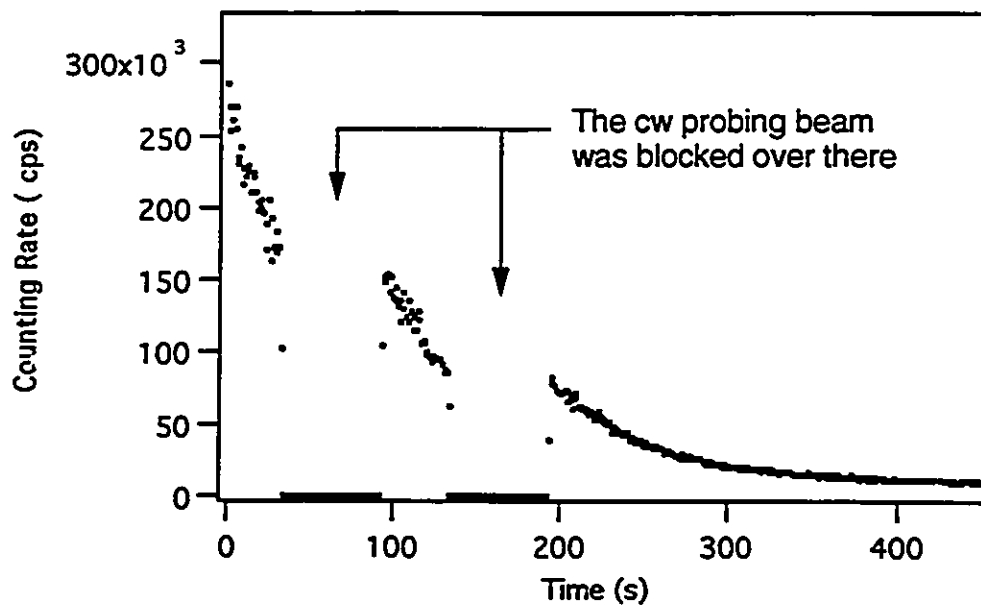
Figure 4.2: Effect of blocking the probing uv laser beam during the fast decay of the de-exciting fluorescence.
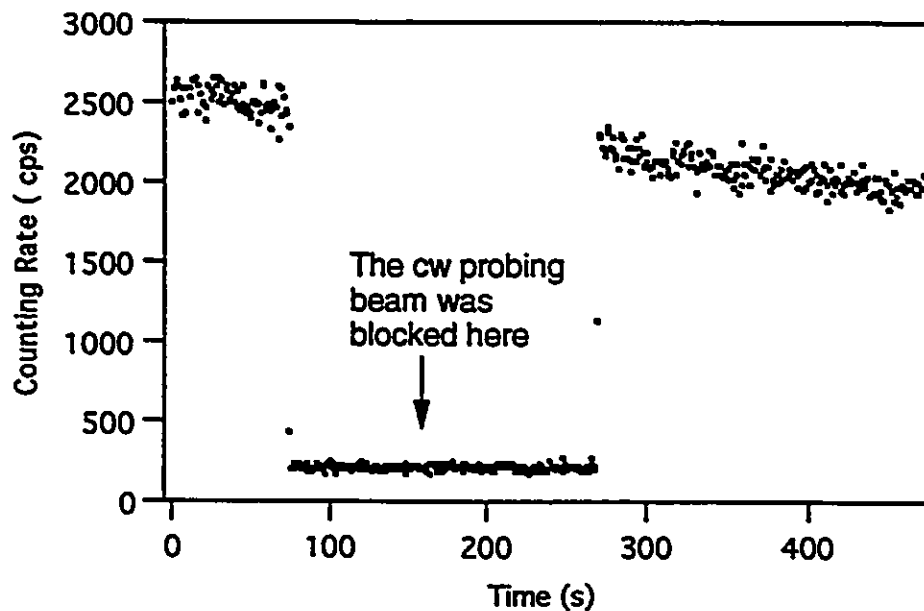
Figure 4.3: Effect of blocking the probing uv laser beam during the slow decay of the de-exciting fluorescence.

41

Fig. 4.4 is from a sample of ions which kept in the trap for the same time (3 min) but excited resonantly when inside the trap. After three-minute resonant uv irradiation, the centroid of the mass peak corresponding to that of Hf$^+$ has actually shifted by about one atomic mass unit to the heavier side as demonstrated in Fig. 4.4. It is
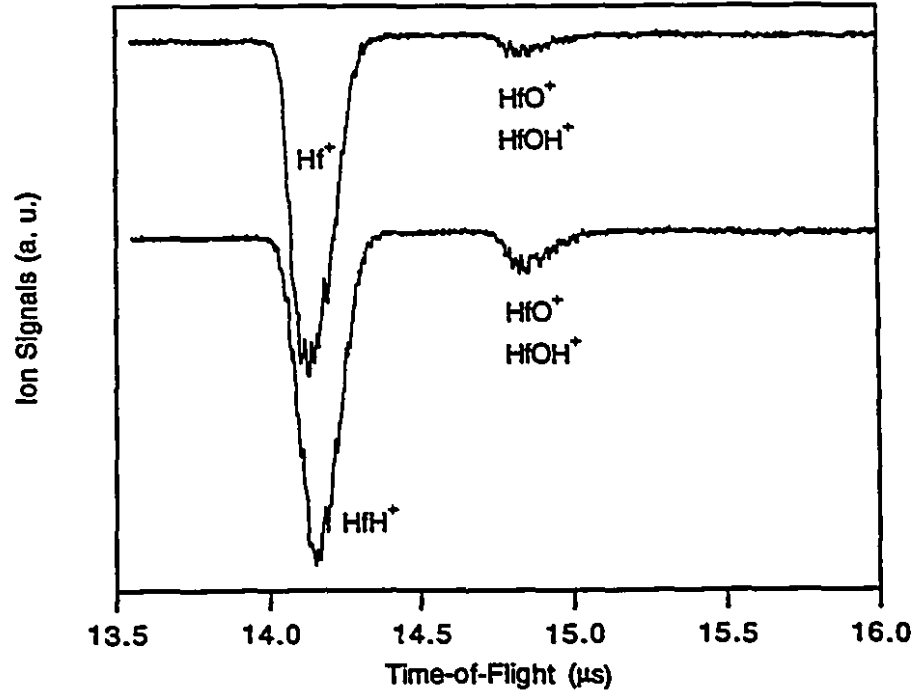
Figure 4.4: Time-of-flight spectra of ejected ions, with (the lower trace) and without (the upper trace) undergoing optical pumping. After three-minute resonance uv irradiation, Hf ions convert into heavier HfH ions.

the formation of HfH$^+$ molecules with laser excitation that is responsible for the loss of the pure Hf$^+$ when the ions are continuously irradiated by resonance cw probing light. This continuous excitation results in a fair amount of HfH ions staying in the trap.

4.1.2   Estimation of the Chemical Reaction Rate

If the formation of HfH ions is a non-reversible process, one would expect the LIF to drop to zero with the fast decay time constant. However as shown in Fig. 4.1, the LIF

signals drop rapidly and reach a a non-zero level after a few minutes with the resonant uv irradiation. This suggests that in the LIF measurements, there must be a process involving HfH molecular dissociation. In our previous experiment (Fig. 4.3), it seems that collisions with the buffer gas has no effect on the dissociation of the molecules. Naturally we would expect that cw probing laser beam could induce HfH molecular dissociation. This can be tested by detuning the cw laser off the resonance frequency. In the experiment, the Hf^+ ions were first irradiated by resonant excitation. When the fluorescence counting rate reached a steady level, the cw uv laser light was detuned off the resonance frequency, and a few minutes later, returned back in its resonance frequency. The LIF counting rate variation is shown in Fig. 4.5. It can be
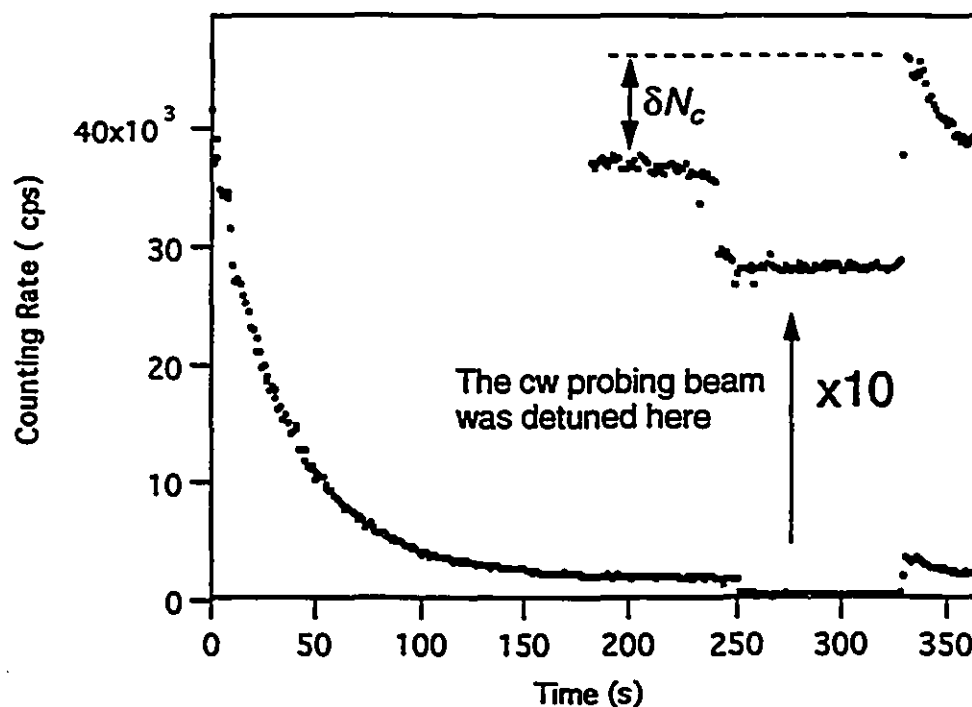
Figure 4.5: Demonstration of HfH molecule dissociation induced by detuned cw uv laser beam.

seen that after the non-resonant uv irradiation, an increase of fluorescence signals was actually observed. This is due to the optically induced dissociation of the HfH^+ molecules. It is this non-resonant photon dissociation coupled with the laser-induced

chemical reaction to form HfH that results in a non-zero level in the decay of LIF signals. The process can be schematically shown in Fig. 4.6
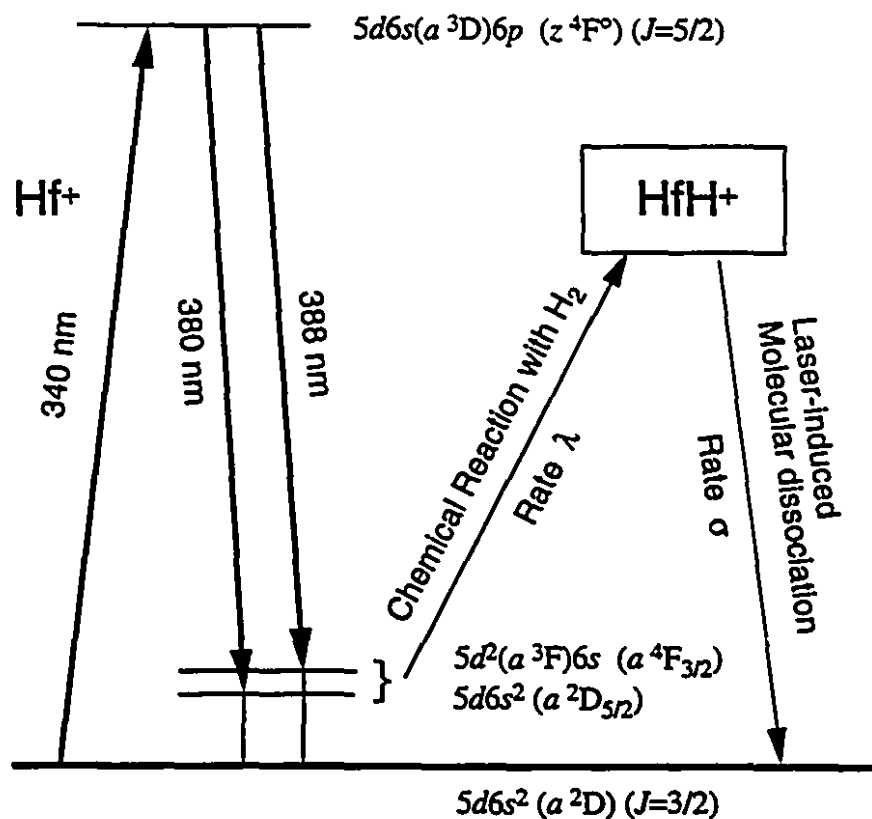
Figure 4.6: Diagram illustrating laser-induced chemical formation of HfH and its dissociation.

After excitation to the $5d6s(a^3D)6p$ state, the Hf ions de-excite mainly to the ground state and the lower lying metastable states $5d6s^2$ (a^2D) $(J = 5/2)$ and $5d^2(a^3F)6s$ (a^4F) $(J = 3/2)$. The ions in these metastable states can be quenched by H_2 collisions. As an alternative, the collisions with the H_2 molecules can also lead to the formation of a HfH molecule, a process described by

$$Hf^{+(*)}(5d^26s, 5d6s^2(J = 5/2)) + H_2 \rightarrow HfH^+ + H \qquad (4.1)$$
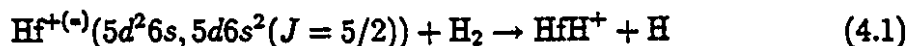
At the same time, the cw probing uv irradiation can non-resonantly dissociate the HfH^+

$$HfH^+ + h\nu \rightarrow Hf^+ + H \qquad (4.2)$$

44
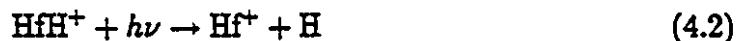
The formation rate of HfH as well as the molecular dissociation rate can be estimated from the time dependence of the fluorescence signal (see Fig. 4.1), which is proportional to the number of pure Hf ions in the trap. Let $N(t)$ represent the number of ions in the trap at time t, and λ pumping rate to form HfH, σ the cw uv photon dissociation rate. Then

$$dN = -N\lambda dt + (N(0) - N)\sigma dt \qquad (4.3)$$

The first term on the right side of eqn. (4.3) accounts for the ion loss due to HfH formation and the second term is due to possible dissociation of HfH by the cw-uv light used for excitation. Since our storage times for the ions in the trap without laser excitation is in the order of one hour, N_0 as the number of ions in the trap at $t=0$, is assumed to be constant during the fast decay. Thus

$$N(t) = \frac{\sigma N(0)}{\lambda + \sigma} + \frac{\lambda N(0)}{\lambda + \sigma} e^{-(\lambda+\sigma)t} \qquad (4.4)$$

From a fit of eqn.(4.4) to the experimental data, λ and σ can be found $\lambda = 0.0088$ s^{-1} and $\sigma = 0.00086$ s^{-1}. This result implies that laser-induced dissociation is one order of magnitude less important than laser-induced formation of HfH$^+$.

The HfH formation rate is much smaller than the collisional quenching rate from the metastable states to the Hf ground state, as will be shown in the following. The quenching rate can be estimated from the fluorescence photon yield at a fixed time. Typically 10 photons per second per ion are detected when saturating the optical transition from the Hf ground state. With an estimated detection efficiency of 1%, this translates into 1000 photons emitted per second per ion in the trap. Since between subsequent emissions the ions have to be quenched, a lower limit for the quenching rate of Hf by H_2 in the order of $\tau^{-1} = 1000$ s^{-1} is found. This yields a ratio $R = 1/(\tau\lambda) \approx 10^5$.

4.2   Laser-Induced Molecular Dissociation

The incident cw uv laser light in fact has two effects on the ions. One is to resonantly excite the ions from the ground state to the excited state. The other process is that it

non-resonantly interacts with HfH ions through photon chemical process to dissociate them to Hf^+ again. To further illustrate the optical dissociation, the pulsed dye laser pulses were used to dissociate the HfH^+ molecular ions. The result is show in Fig. 4.7.
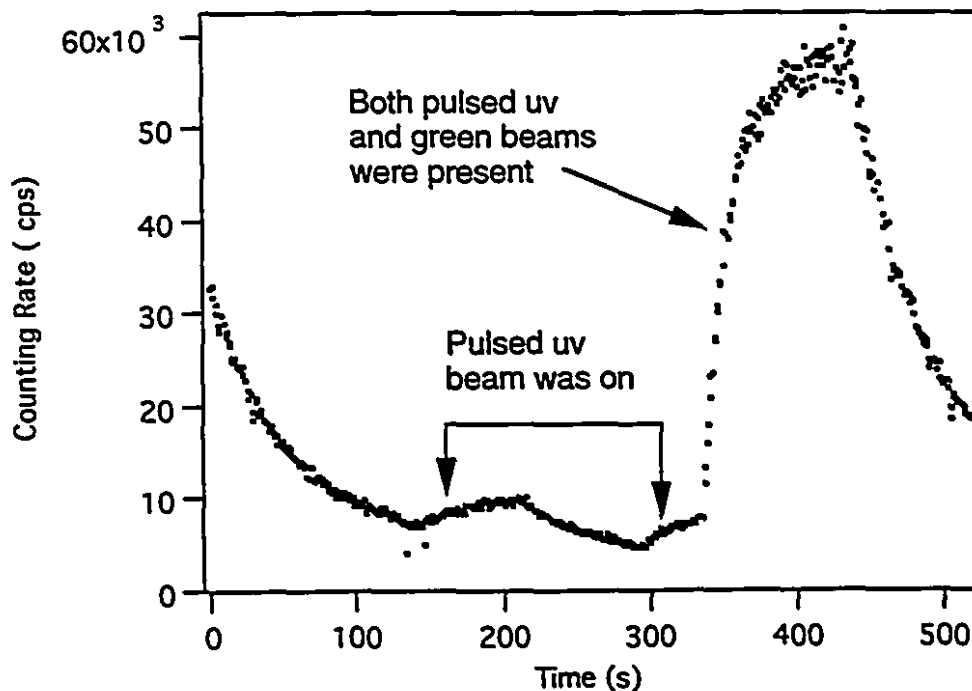
Figure 4.7: Observed strong HfH molecule dissociation induced by pulsed laser beams.

After the fluorescence counting rate dropped to the steady level, the excimer laser was switched on and the pulsed uv beam alone passed through the center of the trap, as was originally set for the resonance ionization of Hf atoms. The LIF counting rate gradually increased when the pulsed uv light was shining on the ion cloud. Then the pulsed uv beam was switched off and the LIF signals started to drop again due to optical pumping. When both the uv and green fundamental pulses were used, the LIF increased very fast then reached the saturation level. The photon dissociation rate with the pulsed laser system is large enough to overcome the effect of the cw laser-induced HfH formation. The full fluorescence signal could be restored through

46

the interaction of HfH ions with the pulsed dye laser beams. We can say that the ions have been totally recuperated by using the combined uv plus green pulsed laser beams. On the other hand, when using green light alone the photon dissociation effect is hardly to be seen. Further experimentation shows that the dissociation from the pulsed laser beams is not a resonance process. The dissociation rate is constant over a wide range of laser wavelength (larger than 10 nm).

There could be a possibility that the optical quenching effect is buffer gas dependent. To examine this, the ions were first pumped to form HfH molecular ions. Before applying the pulsed laser to recuperate Hf ions, the inlet valve of hydrogen buffer gas was switched off. The vacuum pressure went down to the base pressure in a few seconds. We started to send the RIS laser pulses to dissociate the HfH molecules. After Hf ions has assumed to be regenerated, the buffer gas was put back to the chamber again. Subsequent measurement showed that the ions were indeed rejuvenated as in the case with hydrogen buffer gas in. This clarified that the photon dissociation induced by the pulsed laser light is independent of the presence of the H_2 buffer gas.

4.3   Isotope-Selective Suppression Technique

As shown above, laser-induced chemical reaction can convert pure Hf^+ ions into HfH^+. At first glance, this seems to be a drawback for laser spectroscopic measurement. In fact this is not a serious problem, since the laser wavelength is always scanning across the resonance. When the laser wavelength is tuned off the resonance, the non-resonance uv laser light will dissociate the HfH^+, which has formed during the time laser is staying in resonance with the trapped Hf ions.

More important is that we can benefit from this laser-induced chemical process. Since only the isotope which is in resonance with the cw uv laser light can be affected by continuous optical pumping, this can allow us to selectively suppress the LIF contribution of a particular isotope by converting those Hf^+ ions into HfH^+ molecules. In laser spectroscopic studies of confined ions in a Paul trap, since the trap has a poor mass selectivity, the ions of a large range of mass can be trapped simultaneously.

Although RIS has been used to selectively ionize particular element, the different isotopes in the sample can still be ionized simultaneously and be trapped. The spectra obtained with ions of different isotopes often show their mixed contributions due to possible hyperfine splittings. The spectrum of a low abundance Hf isotope could be masked by the hyperfine lines of other Hf isotopes with high abundances as demonstrated in Fig.4.8(a), where a weak spectral line from mass A_2 is lying close
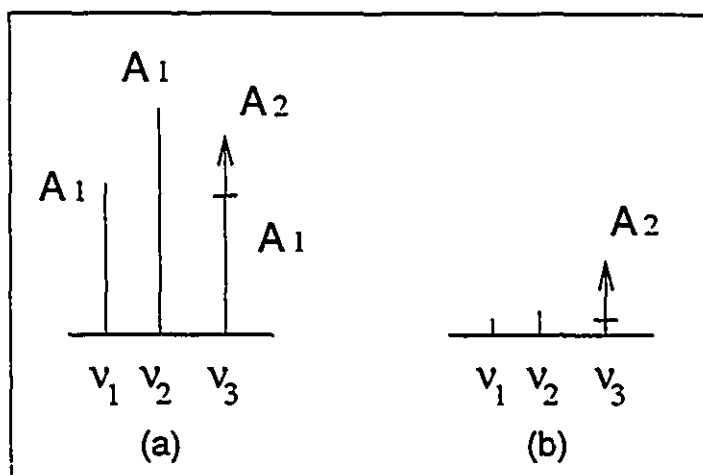
Figure 4.8: A schematic diagram demonstrating an isotope-selective suppression method. (a). The spectral lines from isotopes A_1 and A_2. The weak line from A_2 is mixed with one of the hfs lines from A_1. (b). The spectral lines after suppression of hfs lines from A_1 with optical pumping at ν_1 or ν_2, indicating that the weak signal from A_1 is enhanced.

to one of the strong hfs lines of mass A_1. In this case, suppressing the contribution from mass A_1 would enhance the weak signal from A_2. Experimentally we found that the populations in hyperfine levels are very well in thermal equilibrium through the buffer gas collisions. Optical pumping one of the hyperfine levels resulted in a uniform decrease of all the hyperfine components of a particular isotope. Therefore, by tuning the laser at either ν_1 or ν_2 transition for a few minutes, the unwanted Hf isotope A_1 will convert into HfH$^+$ ions. Subsequent spectroscopic measurement will show that the contribution from the isotope A_1 will have been greatly suppressed. Therefore, the weak signals can get enhanced (see Fig.4.8(b)). This technique, which can be called

the isotope-selective suppression method, has been applied to laser spectroscopic studies of radioactive isotope ^{172}Hf. The weak ^{172}Hf signal has been enhanced after selective suppression of the contributions from the contaminant isotopes ^{177}Hf and ^{179}Hf given in section 7.2.2.

Besides the application in Hf, the isotope selective suppression method is quite possible to be applied to other elements in laser spectroscopic studies using a Paul trap, as long as an optically induced population "trapping" can be found. For example, a fast decay of LIF counting rate due to laser resonance irradiation has been reported in ytterbium [41, 42]. The process is considered to be associated with a long-lived metastable state in Yb$^+$. This can allow the selective suppression method to be applied to Yb$^+$ spectroscopic studies by optically pumping the unwanted Yb isotopes into the long-lived metastable state.

Chapter 5

Trapped Ion Kinetic Motion and Doppler Width Reduction

In trapped ion laser spectroscopy, the Doppler width $\Delta\nu$ resulting from the kinetic motion of the ions is governed by

$$\Delta\nu/\nu_0 \propto v/c \qquad (5.1)$$

where v is the mean velocity of the ions and c is the light speed. To understand the ion motion inside the trap and reduce the Doppler linewidth, a phase-selective laser spectroscopic method has been used in our studies. The spectral linewidths at different RF phases can yield information about the variation of the mean velocity of the ions with the change of the RF phase. In this work, systematic studies of ion kinematics have been done with LIF measurements at different trap operating conditions. The right choice of operating condition improves the spectroscopic resolution and allows the measurement of the hfs and isotope shifts of ions confined in a Paul trap. To begin with, some knowledge about RF phase-space dynamics is presented.

5.1 RF Phase-Space Dynamics

The basic theory of the RFQ trap, given in section 2.1, has described ion motion under the driving RF field. It tells us that initial position and velocity for a single ion determine a fixed trajectory governed by the Mathieu equation. However, when there are many ions inside the trap, the ion motion can be best described by RF phase-space dynamics.

50

Phase-space dynamics can allow us to study the variations of the characteristic quantities —position and velocity— with the passage of time. The so-called phase-space is a six-dimensional space $(\boldsymbol{r}, \boldsymbol{v})$. In Cartesian coordinates. the motion in three orthogonal directions x, y, and z may be considered independently of one another. The phase-space can be treated as three separate phase-planes $(x, \dot{x})$. $(y, \dot{y})$. and $(z, \dot{z})$. It is a very important property that if a group of particles at a certain time t_1 is bounded in phase space by boundary C_1. at time t_2. C_1 will have transformed to a boundary C_2 which will bound the same group of particles. Therefore we only need to study how a boundary in phase space transforms with the time.

It is known that when an ion enters the trap at an initial RF phase ξ_0 ($\xi = \Omega t_0/2$ as used in eqn. (2.12)) with certain value of u and $\dot{u}$, then at phases during subsequent cycles given by

$$\xi = \xi_0 + k\pi, \qquad k = 1, 2, 3, \cdots \tag{5.2}$$

its position and velocity (including the initial condition) will lie on the same ellipse in phase-space. Therefore, if such an ion spent an infinite time in the RFQ trap, values of u and $\dot{u}$ measured at specific phase angle ξ during each cycle would eventually form an ellipse in phase space [24, 25]. This provides a direct way to find the ellipse boundary at different RF phases. The equation of such an ellipse in u, $\dot{u}$ space can be expressed as

$$\Gamma u^2 + 2Au\dot{u} + B\dot{u}^2 = \varepsilon \tag{5.3}$$

where ε is given by

$$\varepsilon = \frac{\text{area of ellipse}}{\pi} \tag{5.4}$$

and

$$B\Gamma - A^2 = 1 \tag{5.5}$$

A, B and Γ are time-dependent quantities. From the diagram shown in Fig. 5.1, we can see Γ and B are related to the maximum velocity and displacement, respectively. The quantity ε, however, is independent of time. That means that the phase-space volume or area occupied by a group of particles is conserved. This is the result of an important law concerning phase-space boundaries and is a consequence of the

51
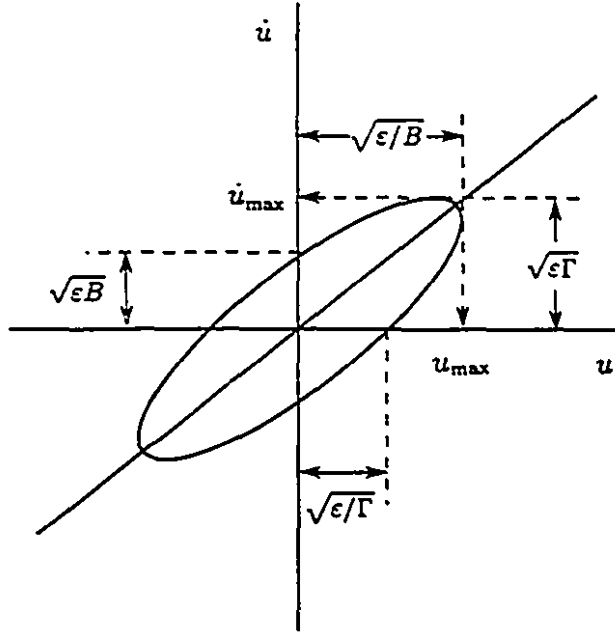
Figure 5.1: Phase-space ellipse showing critical dimensions.

application of Liouville's theorem to the motion of a particle in phase space. The boundary ellipse is sometimes called an *acceptance ellipse* or *emittance ellipse*.

One way to calculate A, B and Γ is by using matrix techniques. If an ion is moving within the quadrupole field with a displacement $u(t_1)$ and a corresponding velocity $\dot{u}(t_1)$ at an initial time t_1, the new displacement $u(t_2)$ and velocity $\dot{u}(t_2)$ at a later time t_2 can be determined by using the state transition matrix thus

$$\begin{pmatrix} u(t_2) \\ \dot{u}(t_2) \end{pmatrix} = M(t_2, t_1) \begin{pmatrix} u(t_1) \\ \dot{u}(t_1) \end{pmatrix} \tag{5.6}$$

It has been shown that for the RF quadrupole field A, B, and Γ parameters are related to the matrix M for the complete cycle by the expression [24, 25]

$$M(\xi_0 + \pi, \xi_0) = \begin{pmatrix} cos\beta\pi + Asin\beta\pi & Bsin\beta\pi \\ -\Gamma sin\beta\pi & cos\beta\pi - Asin\beta\pi \end{pmatrix} \tag{5.7}$$

For any (initial) RF phase, the ellipse parameters can be determined from the elements m_{ij} of the matrix M. Thus

$$B = \frac{m_{12}}{sin\pi\beta} \tag{5.8}$$

52

$$\Gamma = \frac{-m_{21}}{\sin \pi \beta} \qquad (5.9)$$

and

$$A = \sqrt{B\Gamma - 1} \qquad (5.10)$$

in accordance with eqn. (5.5).

Here, β represents the constant relating the secular frequency of ionic oscillation ω_0 to the driving frequency Ω of the applied RF voltage ($\beta = \omega_0/(\Omega/2)$, see eqn. (2.15)). The matrix M for the complete cycle also contains information on the nature of ion motion. The trace of the matrix is given by $m_{11} + m_{22} = 2\cos\pi\beta$. For stable trajectories (real β), the trace of the matrix M must lie between -2 and 2.

To calculate the state transition matrix in a complete cycle, several approaches are possible. In this work, the piecewise-constant or staircase approximation method has been applied to calculate $M(\pi + \xi_0, \xi_0)$. In this approach the applied waveform is divided into a large number of narrow rectangular steps of equal length. Over a certain time period, M may be represented as the product of all such matrices over subintervals within that period. For example,

$$M(t_3, t_1) = M(t_3, t_2) \cdot M(t_2, t_1), \qquad t_3 > t_2 > t_1 \qquad (5.11)$$

Thus the matrix for the complete RF cycle can be obtained from the product of the matrices for fractions of the RF cycle. Now let's come back to see how to calculate the matrices for the narrow rectangular steps.

The general equation of ion motion inside trap has been given earlier in eqn. (2.12). In our approximation during the period ξ_1 to ξ_2, the equation can be represented as

$$\frac{d^2u}{d\xi^2} + h_1^2 u = 0 \qquad h_1 > 0 \qquad (5.12)$$

or

$$\frac{d^2u}{d\xi^2} - h_2^2 u = 0 \qquad h_2 > 0 \qquad (5.13)$$

The position and velocity ($du/d\xi$) at the end of this period are then given by

$$\begin{pmatrix} u \\ \dot{u} \end{pmatrix}_{\xi_2} = \begin{pmatrix} \cos\left[h_1(\xi_2 - \xi - 1)\right] & \{\sin\left[h_1(\xi_2 - \xi_1)\right]\}/h_1 \\ -h_1 \sin\left[h_1(\xi_2 - \xi_1)\right] & \cos\left[h_1(\xi_2 - \xi_1)\right] \end{pmatrix} \begin{pmatrix} u \\ \dot{u} \end{pmatrix}_{\xi_1} = M(\xi_2, \xi_1) \begin{pmatrix} u \\ \dot{u} \end{pmatrix}_{\xi_1}$$

$$(5.14)$$

corresponding to the former case, or

$$\begin{pmatrix} u \\ \dot{u} \end{pmatrix}_{\xi_2} = \begin{pmatrix} \cosh\left[h_2(\xi_2 - \xi - 1)\right] & \{\sinh\left[h_2(\xi_2 - \xi_1)\right]\}/h_1 \\ h_2 \sinh\left[h_2(\xi_2 - \xi_1)\right] & \cosh\left[h_2(\xi_2 - \xi_1)\right] \end{pmatrix} \begin{pmatrix} u \\ \dot{u} \end{pmatrix}_{\xi_1} = M(\xi_2, \xi_1) \begin{pmatrix} u \\ \dot{u} \end{pmatrix}_{\xi_1}$$

$$(5.15)$$

corresponding to the solution from eqn. (5.13). It will then be possible to calculate the state transition matrix $M(\pi + \xi_0, \xi_0)$ using a staircase approximation. In the calculation, the cycle has been divided into 20 000 rectangular steps. The family of phase-space ellipses for ion motion in r directions at the work point $a_z = 0$ and $q_z = 0.374$ is shown in Fig. 5.2, demonstrating the variation of the shape and
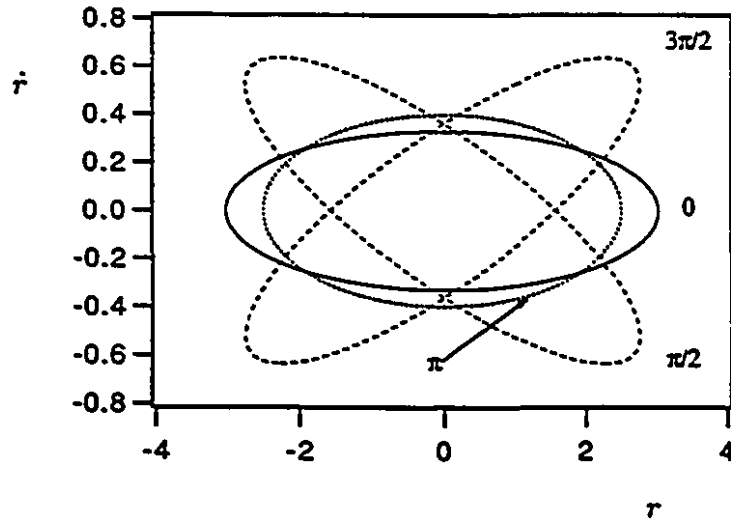
Figure 5.2: A group of phase-space ellipses at different RF phase angles. The trapping condition is $a_z = 0$ and $q_x = 0.374$.

orientation of the ellipse with the change of the RF phase while keeping a constant area. It can be seen that the size of the phase diagram along the $\dot{r}$ axis, which indicates the velocity spread of an ion cloud at the radial direction, changes with the RF phase. At zero RF phase, the ion motion along the radial direction reaches a minimum. This suggests that laser spectroscopic measurement at zero RF phase can be used to improve the spectral resolution.

5.2 $\Delta\nu_r$ Versus the RF Phase Angle

Phase-space dynamics suggests that the velocity spread of the ion cloud, and their spectral linewidth $\Delta\nu_r$ due to ion Doppler motion vary with the RF phase. This variation of the spectral linewidth can be measured by phase-selective LIF de-excitation. To carry out the measurement, the cw uv laser beam is modulated to excite the ions at a particular RF phase during a period (100 ns) much shorter than the RF cycle. Meanwhile, the de-exciting fluorescence photons from those ions are recorded by RF phase-locked coincidence counting. This technique will be referred to as *Phase-Selective LIF*.

In the study, an enriched $^{178}HfO_2$ sample was used. At each RF phase, the LIF spectrum was obtained by scanning the probing uv laser wavelength across the resonance frequency with $\lambda = 340$ nm. Since the even-even Hf isotope gives a single resonance peak and the laser linewidth is negligible, the spectral linewidth corresponds to the velocity spread of the ion cloud in the trap. In Fig. 5.3, the spectra obtained at various RF phases are shown. The spectral linewidths at various phase angles have been derived and plotted in Fig. 5.4. Systematic measurements have been done at two trap operating conditions. One corresponds to a dc bias of zero volts and the other with a dc bias of 28 V. The same number of ions was kept inside the trap for both measurements. From this, one can clearly see the variation of the linewidth with the RF phase, with minima occuring at phase 0 and π.

These experimental width variations can be compared to the theoretical results from the phase-space diagrams. Fig. 5.5 shows the calculated $\sqrt{\epsilon\Gamma}$ at different RF phase, where ϵ for zero dc voltage is set to be 1, while for 28 V dc voltage ϵ is set to be 0.65 to normalize the $\delta\nu_r$ of zero RF phase. The experimental results shown in Fig. 5.4 agree very well with the calculations from phase-space dynamics. It is interesting to note that the calculation indicates different $\delta\nu_r$ at 0 and π phase angles, and these are reproduced in the actual measurements. Further discussion of the change of kinetic energy at different dc voltage and the pseudopotential model can be found in section 5.5.1.
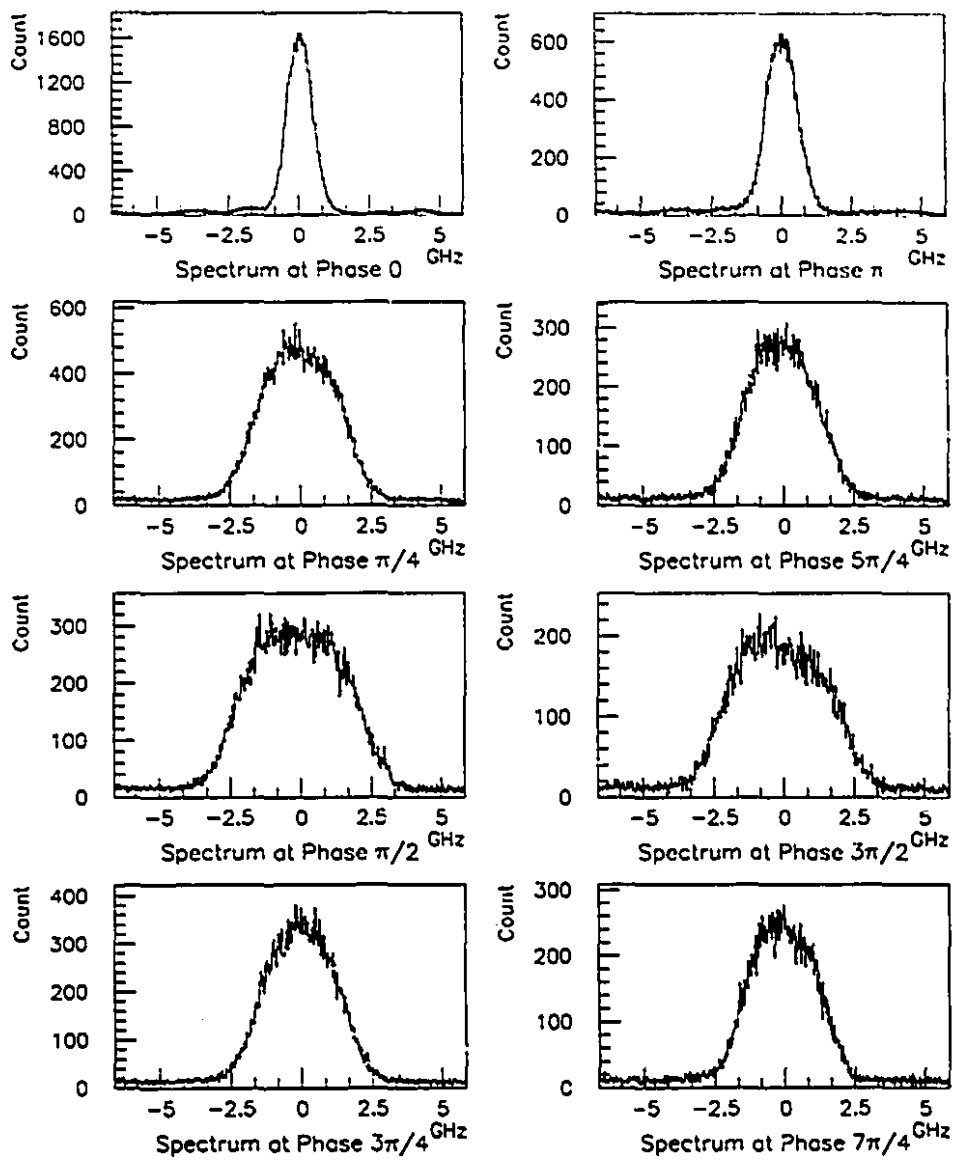
Figure 5.3: A group of laser spectra at different RF phase angles measured by phase-selective LIF. The trapping condition is $a_z = 0$ and $q_z = 0.374$. The variation of the spectrum linewidth is due to the variation of the velocity spread of the ions along the radial direction.
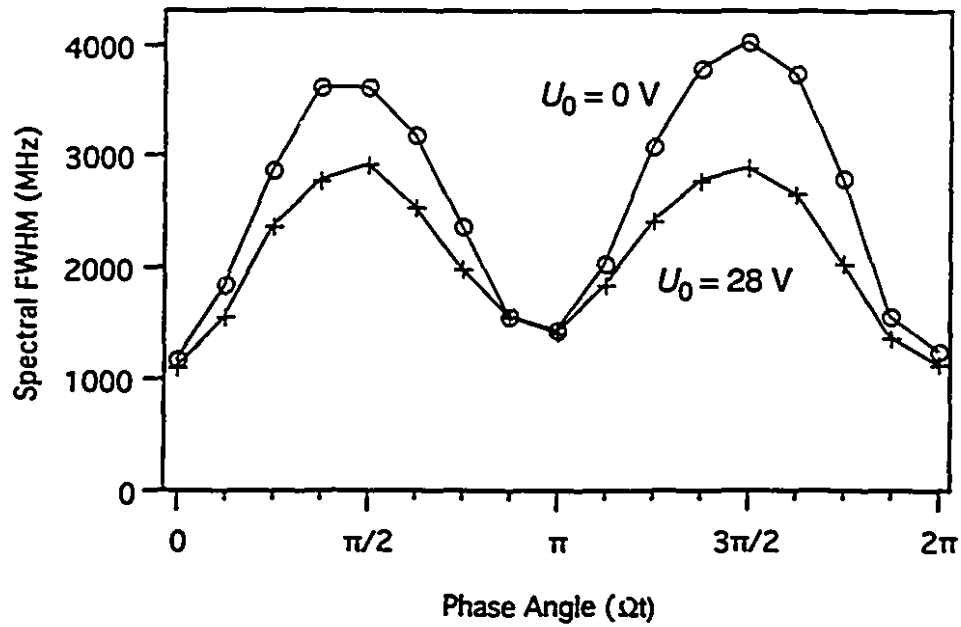
Figure 5.4: Spectral full width at half maximum (FWHM) against RF phase angles. The two curves correspond to $(a_z = 0,\ q_z = 0.374)$ and $(a_z = -0.048,\ q_z = 0.374)$, respectively.
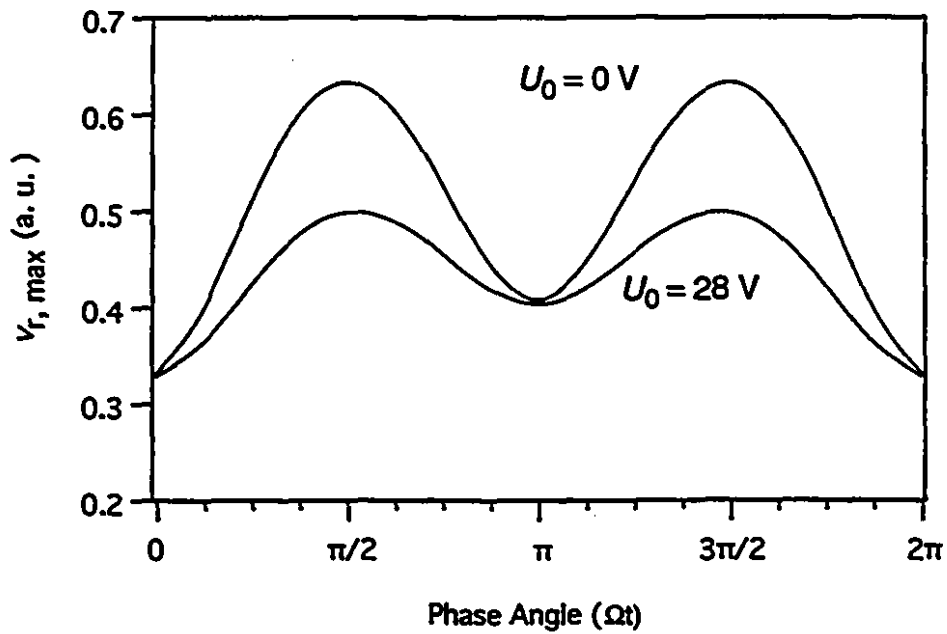
Figure 5.5: Calculated velocity spread in the phase-space ellipse $\sqrt{\varepsilon\Gamma}$ against RF phase angles. The two curves correspond to $(a_z = 0,\ q_z = 0.374)$ and $(a_z = -0.048,\ q_z = 0.374)$, respectively.

5.3 $\Delta\nu_r$ Dependence on the Number of Ions

The phase-space calculation carried out in section 5.1 is in an ideal situation, where the ion motion is only considered to be governed by a pure RF quadrupole field. In a practical trap, a buffer gas is often used to cool the ions, as discussed in section 3.4. The RF motion can result in indirect heating due to the interactions it causes, such as interactions with the background residual gas. There are also Coulomb interactions between the ions themselves. So far there is no theoretical model which accurately includes all these interactions in studies of ion trap kinematics.

With phase-selective LIF, one can measure $\Delta\nu_r$ at each individual RF phase with different trap operating conditions. In particular, the variation of $\Delta\nu_r$ versus the number of ions in the trap can provide valuable information about the Coulomb interaction between the trapped ions. The spectral linewidth with respect to the number of ions was measured at zero, $\pi/2$ and π RF phases by phase-selective LIF. (The effect at RF phase $3\pi/2$ is the same as at RF phase $\pi/2$). In the measurement, the trap was operating at an RF frequency of 400 kHz with trapping parameters $a_z = 0$ and $q_z = 0.374$. A certain number of ions was first loaded into the trap with desorption and RIS laser pulses. The ion load was controlled by adjusting laser power and the number of laser shots. LIF spectra were then acquired at the three different RF phases. Afterward, the ions were ejected to the MCP detector to measure the number of ions. The resultant spectral linewidth versus the number of ions is plotted in Fig. 5.6. Two different features are revealed in the diagram. The $\Delta\nu_r$ measured by phase-selective laser spectroscopy at RF phase angle $\pi/2$ very much depends on the number of ions trapped, indicating that the $\Delta\nu_r$, or the mean velocity of the ions, increases with N. However, the $\Delta\nu_r$ measured at RF phase 0 and π show only a very slight increase with increasing N.

Due to Coulomb interactions, the size of the ion cloud would become larger when more ions are in the trap. If the phase-space diagrams kept the same shapes, the velocity spread at any RF phase should also show an increase proportional to the size of ion cloud. The relatively constant velocity spread observed at zero RF phase implies that not only the phase-ellipse volume but also its eccentricity changes

58
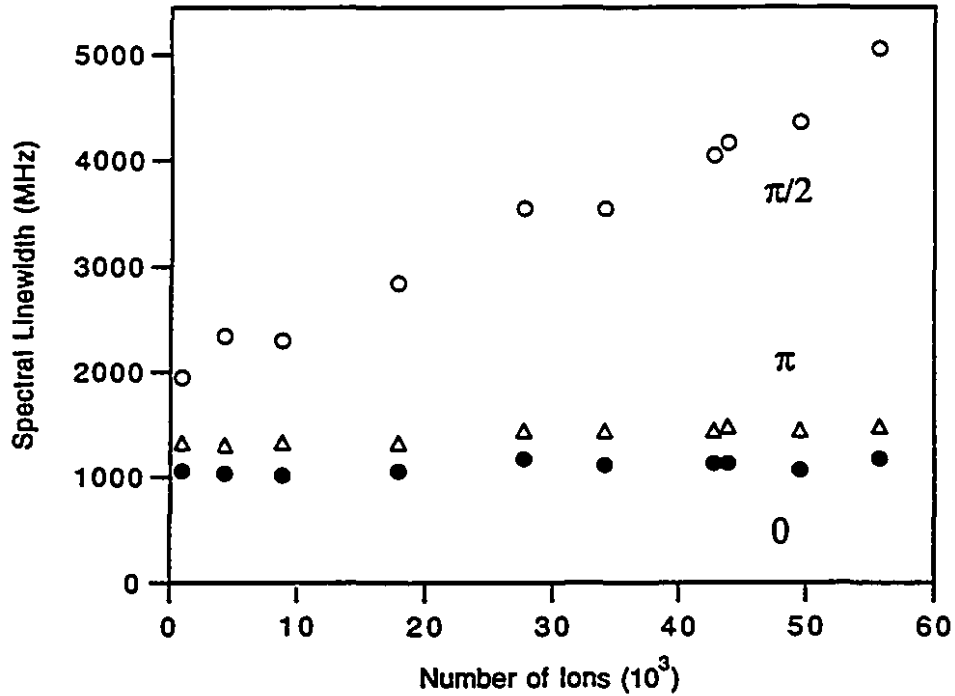
Figure 5.6: Spectral full width at half maximum (FWHM) against the number of trapped ions. The trapping parameters are (a_z=0, q_z=0.374). The measurements have been done at RF phase angles 0, $\pi/2$ and π.

with the number of ions. At zero RF phase, with more ions inside the trap, the phase-space diagram should become elongated in space, resulting in little change of the velocity spread. These changes of the phase ellipses are illustrated in Fig. 5.7. Following the elongated phase ellipse at zero RF phase, as the RF phase changes, the phase-space ellipse changes its orientation and eccentricity. At RF phase $\pi/2$ and $3\pi/2$, the phase-space diagrams show a bigger velocity spread.

Let's have a look at the space charge interaction qualitatively. For simplicity, only the motion along the r direction is considered. Given a uniform charge distribution, the ions within the ion cloud will experience a force proportional to r measured from the trap center, which tries to cancel the restoring force induced by the voltage at the ring electrode. Such a dependence is characteristic of a 1-dimensional quadrupole field (see section 2.1). Therefore the space charge effect on the ion motion along r direction is equivalent to a negative dc voltage $-U'$ added to the ring
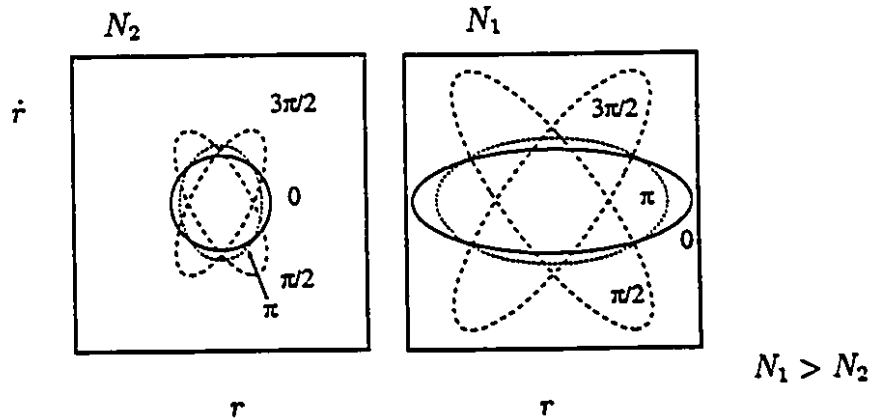
Figure 5.7: Phase-space ellipses at two different numbers of trapped ions. At zero phase angle, a large number of ions is described by a more elongated ellipse. The pictures illustrate that while the velocity spread at zero and π does not change much with respect to the variation of the number of ions, the velocity spread at the phase $\pi/2$ and $3\pi/2$ can vary greatly.

electrode. The more ions inside the trap, the bigger the U', which could cause a bigger change of the phase-space diagram.

It has been generally accepted that when more ions are in the trap, the mean kinetic energy of the ions will increase [29, 43, 44]. This is consistent with our measurements. From Fig. 5.6, it can be deduced that the $\Delta\nu_r$ of the complete RF cycle will increase with the number of ions, since linewidth $\Delta\nu_r$ at RF phase $\pi/2$ and $3\pi/2$ strongly depends on the number of ions trapped. However, previous studies provide no information about the velocity dependence on N at different RF phases. Our experiment results are the first to provide an example of the modification of the phase-space volume due to the space charge effect. It would be interesting to compare our experimental results with calculations with Coulomb force included.

5.4 Ion Temperature Discussion

It has generally been accepted that ion motion in the trap is in a thermal equilibrium, in which the heating and the cooling are balanced. Although the ion temperature concept is used often in the literature to describe ion motion in a trap, different definitions of temperature have resulted in a wide variation in both theoretical and

experimental values reported. Values ranging from room temperature to over 1 eV under similar operating condition have been proposed. A review of works on ion temperature can be found in [29].

Ifflïander and Werth [18] were the first to report optical observation of an ion cloud in a Paul trap under laser illumination. A temperature of about 1 eV for Ba^+ ions in the trap with a potential well depth of 10 eV was deduced from an observed linewidth. Here the temperature in fact refers the mean kinetic energy of the ions. Previous measurements indicated that this energy is related to the pseudopotential well depth by the empirical expression [36]

$$< E_{kin} >= (0.11 \pm 0.01)eD \qquad (5.16)$$

which is obtained at ultra-high vacuum conditions. Here D is the lower value of D_r and D_z. With buffer gas cooling, a further reduction of the ion kinetic energy by a factor of three can be achieved [36]. Therefore, if the ions are cooled with buffer gas, the mean kinetic energy of the ions can be approximated by

$$< E_{kin} >= eD/30 \qquad (5.17)$$

A more recent and more appropriate approach deals with the ion temperature as a statistical quantity. According to Blatt et al. [45], a collection of ions is in thermal equilibrium at a specific temperature of simple harmonic macro-motion in a pseudopotential well, upon which is added an RF micro-motion. The coherent micro-motion does not contribute to the ion temperature but only to the mean kinetic energy. When the particle macro-motion distribution reaches a thermal equilibrium, it can be expressed by a Gaussian for any one of the canonical coordinates [46].

$$dN(v_x) = N\sqrt{\frac{m}{2\pi kT}} \exp\left(-\frac{m}{2kT}v_x{}^2\right) dv_x \qquad (5.18)$$

with

$$\sigma(v_x) = \sqrt{\frac{kT}{m}} \qquad (5.19)$$

where kT is the average thermal energy with ion temperature T. This distribution will actually result after a large number of interactions between a large number of

particles when the interactions randomly distribute a fixed total amount of energy. In this model, the RF micro-motion will distort the phase-space ellipse and change the kinetic energy of ions inside a trap. This superimposed oscillation is in phase with the RF voltage applied to the trap.

Phase-selective LIF provides an easy way to find the statistical temperature of the ions in the trap. As shown in Fig. 5.4, the linewidth at different RF phase varies due to the coherent RF micro-motion. At zero RF phase, the RF micro-motion effect is at a minimum. What remains is the thermal motion. In this way the thermal motion can be isolated from the RF micro-motion. The Gaussian velocity distribution measured at zero RF phase reflects this statistical nature and can be used to determine the ion temperature.

The full width at half maxima (FWHM) revealed by LIF measurements at zero RF phase is found well fixed at about 1 GHz even if the number of ions varies over a large range. With $\lambda = 340$ nm, the ion temperature T deduced from eqn. (5.19) and eqn. (5.1) is 450K and $kT = 0.038$ eV. It is very close to room temperature $T = 293$ K with $kT = 0.025$ eV. The slightly higher value (about 0.013 eV above room temperature 0.025 eV) could be due to the RF heating effect. In our ultra-clean vacuum system, the RF motion should be only slightly modified in phase and amplitude from collisions with the light buffer gas H_2 molecules, resulting in a relatively small RF heating. It is found that over a wide range of trap operating condition, the statistical ion temperature is always relatively fixed and slightly higher than that of the buffer gas.

The 1 GHz spectral resolution obtained is very close to the Doppler width at the room temperature (0.8 GHz). It should be emphasized that the ion temperature should not be confused with the mean kinetic energy. Without phase-selective detection, about 3 GHz spectral linewidth is observed, which corresponds to a mean kinetic energy of 0.3 eV.

5.5   Other Factors Affecting Ion Motion in the Trap

Our phase-selective LIF spectroscopic setup gives us a unique and powerful tool for the study of trapped ion kinematics. Although we felt it unlikely that we could improve our spectral resolution much below the 1 GHz produced by our initial phase-selective LIF measurements, we undertook a systematic study of the measured effects of varying some of the trapping parameters under our control, such as operating voltages, RF frequency and buffer gas pressure, in order to improve our understanding of trapped ion behavior. In many cases the relationship between the trapping parameters and the ion dynamics has never before been experimentally measured.

The measurements have been done two ways. One is just the conventional laser spectroscopic method, in which a cw laser beam is sent into the trap center and the fluorescence counts from the full RF cycle are recorded (referred to as *full cycle LIF* method). The other method is phase-selective coincident counting gated at zero RF phase with a cw probing laser beam.

5.5.1   DC Voltage

Fluorescence linewidths were measured. The number of ions was kept constant. The spectral full widths at half maximum have been compiled and plotted versus the dc bias voltage in Fig. 5.8. The data points represented by an open circle are the results from full cycle LIF, and the data points represented by a solid circle are from phase-selective coincident counting at zero RF phase. The linewidths calculated from eqn.(5.17) are also shown in the diagram. The spectral linewidth measured by full cycle LIF decreases with the increase of the dc bias voltage. On the other hand, the spectral linewidth measured by phase-selective coincidence counting at zero RF phase changes very little with the respect to the dc voltage variation.

The result from zero RF phase can be explained as a small variation of the statistical temperature, which is slightly higher than the room temperature. The variation of the linewidth from the full cycle LIF is due to the RF micro-motion at different operation conditions. This can be compared with the prediction based on the pseudopotential well depth. The experimental result from full cycle LIF mea-
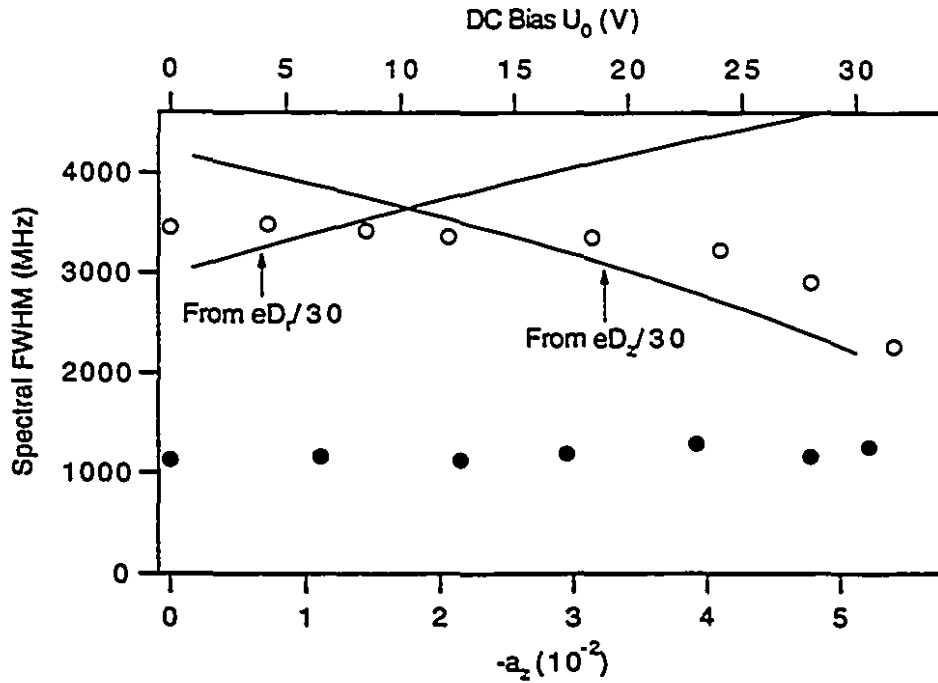
Figure 5.8: Spectrum linewidth versus the dc bias voltage. The solid circles are obtained by coincidence counting at zero RF phase. The open circles are from full cycle LIF. The trap parameter q_z is fixed at 0.374. The curves represent predictions based on the potential well depth.

surements roughly follows the variation of the well depth D, which is the lower value of D_r and D_z.

5.5.2 RF Voltage

Similar measurements have been done while changing the RF voltage. In the measurement, the number of trapped ions was kept constant. The resultant spectral full widths at half maximum are shown in Fig. 5.9. Again the results from full phase LIF are represented by an open circle, and the ones from the coincidence counting at zero RF phase are marked by a solid circle. The smooth curves are derived from the prediction based on the pseudopotential well depth. With the increase of the RF amplitude, the spectral linewidth measured by the full cycle laser spectroscopy increases, indicating an increase of the mean kinetic energy of the ions. Qualitatively, the changes of the mean kinetic energy are consistent with the variation in
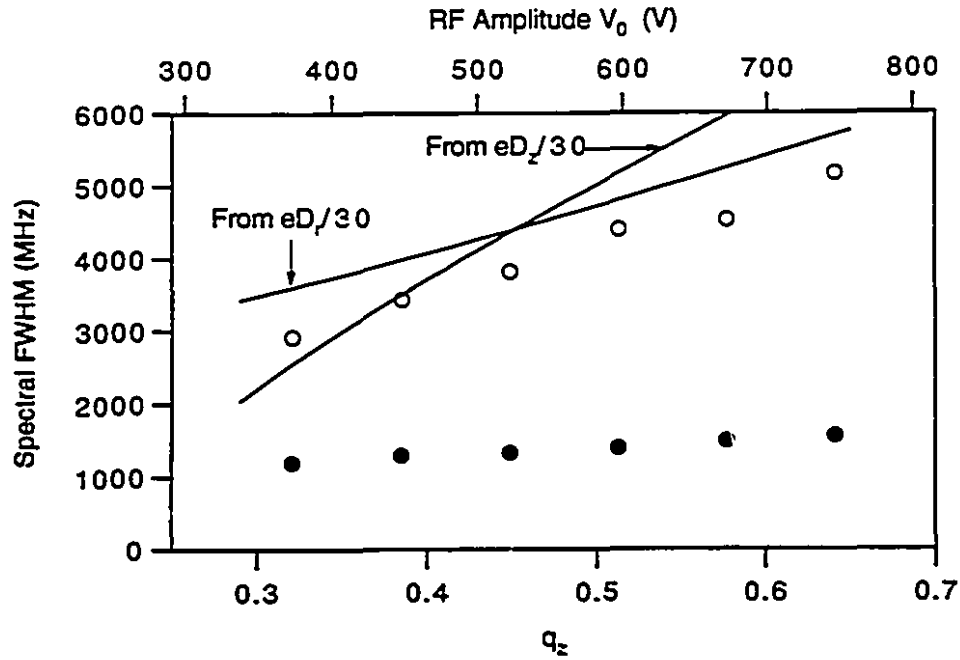
Figure 5.9: Spectrum linewidth versus RF voltage. The solid circles are obtained by coincident counting at zero RF phase. The open circles are from full cycle LIF. The curves represent predictions based on the potential well depth.
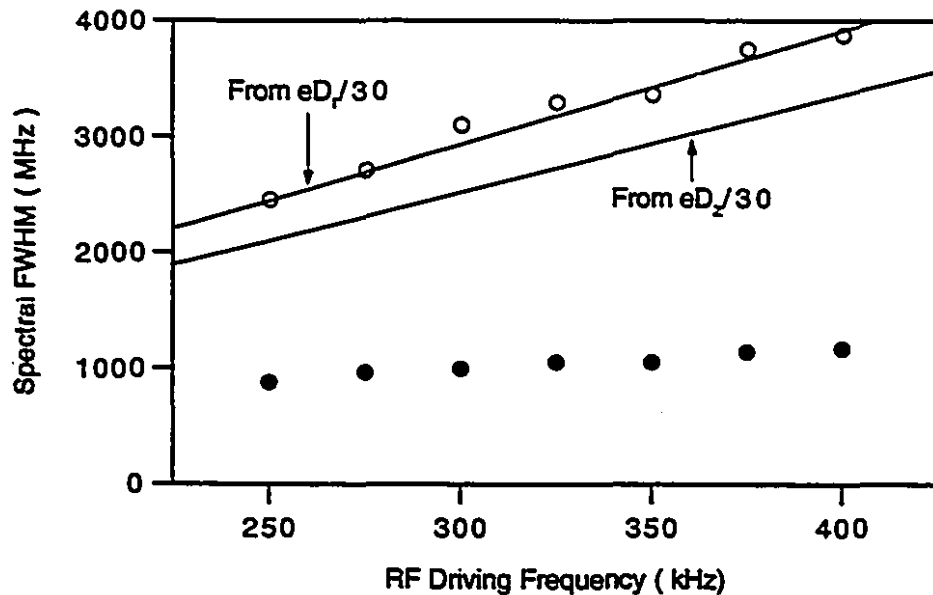
Figure 5.10: Spectrum linewidth versus RF driving frequency. The solid circles are obtained by coincidence counting at zero RF phase. The open circles are from full cycle LIF. The curves represent predictions based on the potential well depth.

the pseudopotential well depth.

On the other hand, with increasing RF voltage it is noticed that the linewidth for the phase-selective coincident counting at zero phase has only a very small increase.

5.5.3 RF Frequency (Constant a_z and q_z)

Laser spectroscopic measurements have been done at different RF frequencies. RF amplitude and dc bias were also adjusted in order to keep the same trapping parameters a_z and q_z. At each frequency, the trap was filled to the maximum load and the spectra were measured by full cycle LIF as well as phase-selective coincident counting at zero RF phase. The results have been plotted in Fig. 5.10. The linewidth based on the potential well depth is also shown by curves in the diagram.

The result from full cycle LIF (open circle) indicates the averaged velocity spread of the ions is decreasing with the decrease of the driving RF frequency. This can be understood by the change of the pseudopotential well depth, which is proportional to Ω^2 as shown in eqn. 2.20 and eqn. 2.21. Our result is consistent with that in [47]. The result from the phase-selective measurement (solid circle) shows that the spectral resolution by phase-selective measurement at zero RF phase can be improved by using a lower driving RF frequency. Typically our trap is operating at 400 kHz and the spectral resolution is about 1 GHz. With the RF driving frequency 250 kHz, we can get less than 900 MHz spectral full width at half maxima, which corresponds to a statistical temperature kT less than 0.031 eV, only 0.006 eV above the room temperature. These results can explain the slightly worse resolution of 1.4 GHz obtained by Rink *et al* [19], where an RF driving frequency of 600 KHz was used.

5.5.4 Buffer Gas Pressure

The effects of buffer gas pressure variations are very hard to analyze independently. The difficulty is that when the buffer gas pressure is too high, the optical pumping induced-chemical process becomes severe due to higher collision rate, which leads

to a decrease of the number of pure Hf^+ ions (see section 4.1). Another factor as mentioned before is that the high buffer gas pressure could lead to an increase of the residual gas content, which could accelerate the oxidation of Hf^+ ions, limiting the pure Hf^+ ion storage time. On the other hand, low buffer gas pressure could reduces quenching of metastable states, and could also affect ion cooling effects.

Here we just give the features with the increase of the buffer gas pressure. In Fig. 5.11 the spectral linewidth versus the buffer gas H_2 pressure is displayed. The spectral linewidth of the full cycle LIF spectrum decreases with the increase of the buffer gas pressure and the linewidth of the phase-selective spectrum changes little, the same way that zero RF phase is insensitive compared with other phases. The change of the linewidth can be explained by the buffer gas cooling effect. Within the pressure range studied, the higher buffer gas pressure would have a better ion cooling effect.

The typical buffer gas pressure in our experiment is about 10^{-3} Pa, which is high enough to meet our requirements both for the collisional quenching and for the ion cooling. Also at this pressure, the chemical process loses are tolerable.
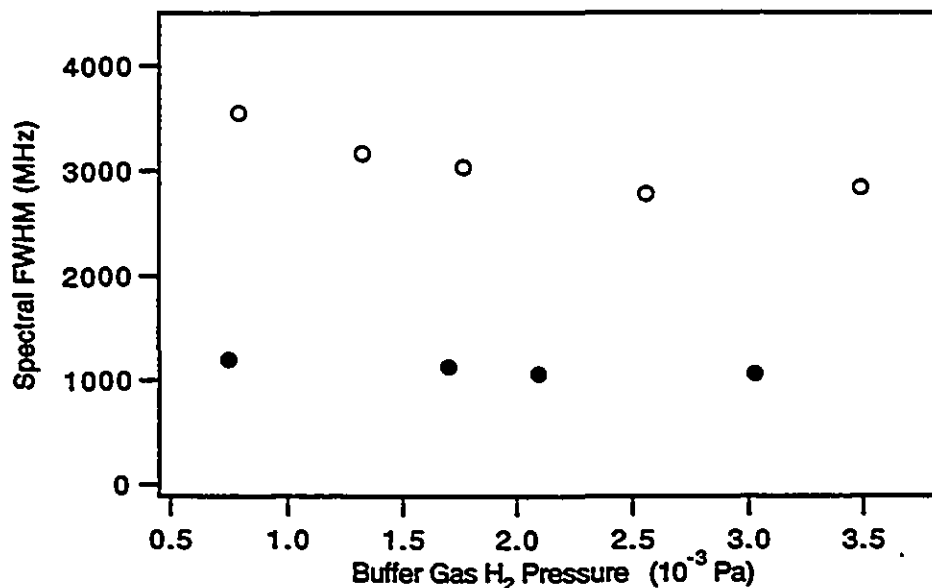

Figure 5.11: Spectrum linewidth versus buffer gas H_2 pressure. The solid circles are obtained by coincidence counting at zero RF phase. The open circles are from full cycle LIF.

5.6 Laser Power Effects

In the development of the phase-selective LIF method, at first the coincidence counting technique without laser modulation was applied in this work. It is a convenient way to get the fluorescence photons at a particle RF phase. Especially, at zero RF phase a narrow Doppler width (about 1 GHz) can be obtained. However, the continuous excitation can lead to a strong optical pumping effect in Hf^+.

In our laser excitation scheme of Hf^+, following the optical excitation from the ground state, an ion can de-excite to the metastable states. The ion at these states need to be quenched by buffer gas collisions, so that a new excitation can be resumed. Therefore the photon counting rate depends on both the excitation rate and the collisional quenching rate. When the laser saturates the optical excitation from the ground state, the photon counting rate will be limited by the quenching rate, which becomes the maximum counting rate one can expect.

In case of cw laser excitation, spectra at different RF phases were measured with ^{178}Hf ions in the trap by the coincidence counting technique. In Fig. 5.12 a group of measurements is shown. Unlike the result shown in Fig. 5.3, some of the spectra yield double peaks. At the phase angle close to $\pi/2$ and $3\pi/2$, the spectra show a great suppression of the signals in the resonance transition, and the linewidths become much bigger. It would seem that the ion motion in the trap is dominated by inward and outward motions, which produce the double peaks. In fact this is completely an optical pumping related process, since the double peaks can disappear either by employing laser modulation at a similar laser power or with cw excitation at a much lower laser power (less than 0.1 mW). Qualitatively the appearance of the suppression of the photon counts at the resonance frequency (see Fig. 5.12) can be explained by collision quenching rate-limited saturation. The photon counts at the resonance frequency are from ions with velocities close to zero near the center of the trap. These ions have less chance to move away from the trap center due to their small kinetic energy, and therefore continuously experience the optical excitation in the full RF cycle. For these ions the effective excitation rate is higher than the quenching rate. At higher laser power the middle portion of the spectra is thus suppressed,
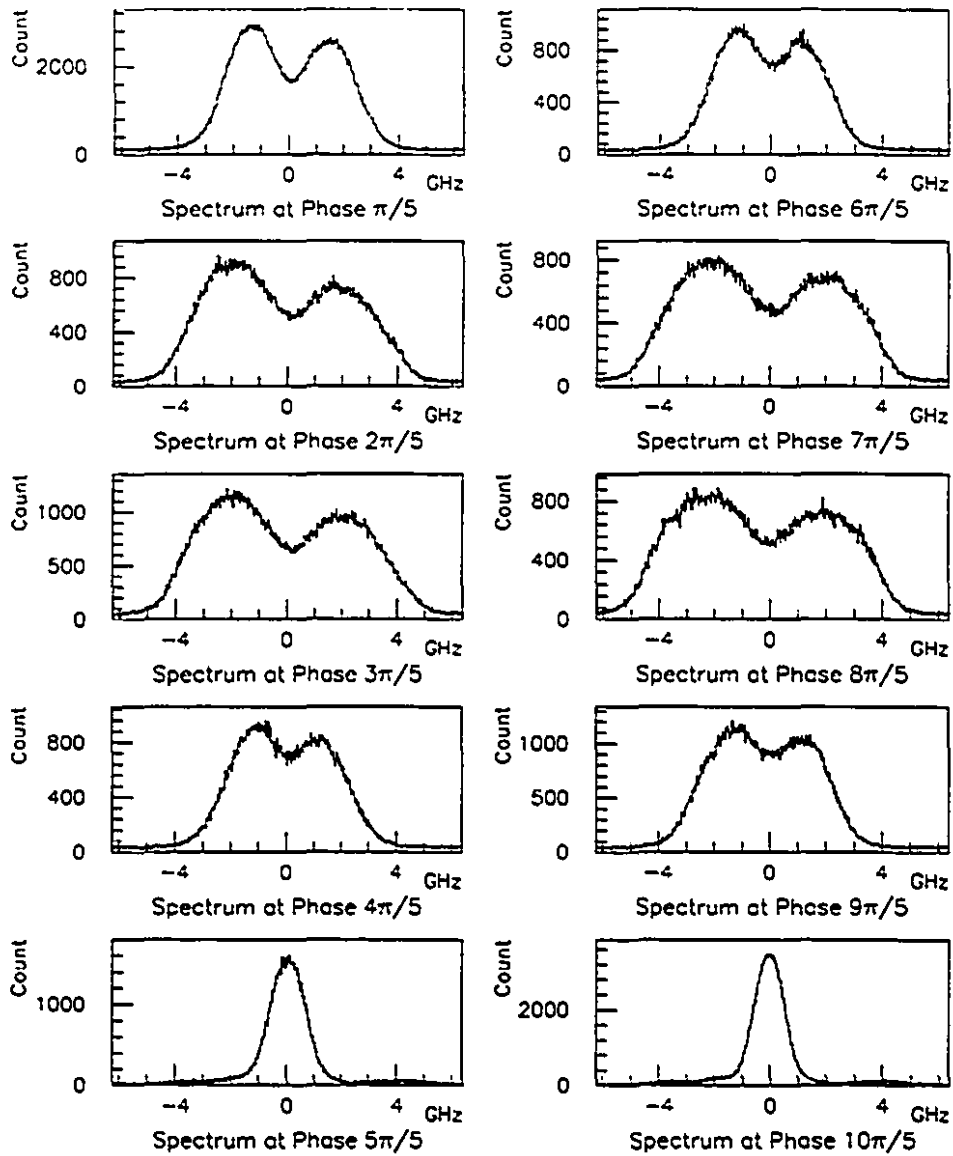
Figure 5.12: A group of LIF spectra at different RF phase angles measured by phase-selective coincidence counting. The trapping condition is $a_z=0$ and $q_z=0.374$. The variation of the spectrum linewidth is due to the variation of the velocity spread of the ions along the radial direction. The central drops in some spectra show the laser-induced saturation effect.

resulting in two humps in the spectrum.

The laser power saturation effect can be further illustrated by full cycle LIF measurements. During the experiment, the same number of ions was kept in the trap. The spectral linewidth versus laser power is displayed in Fig. 5.13 as open circles. The spectral linewidth is increasing with the increase of the laser power showing a
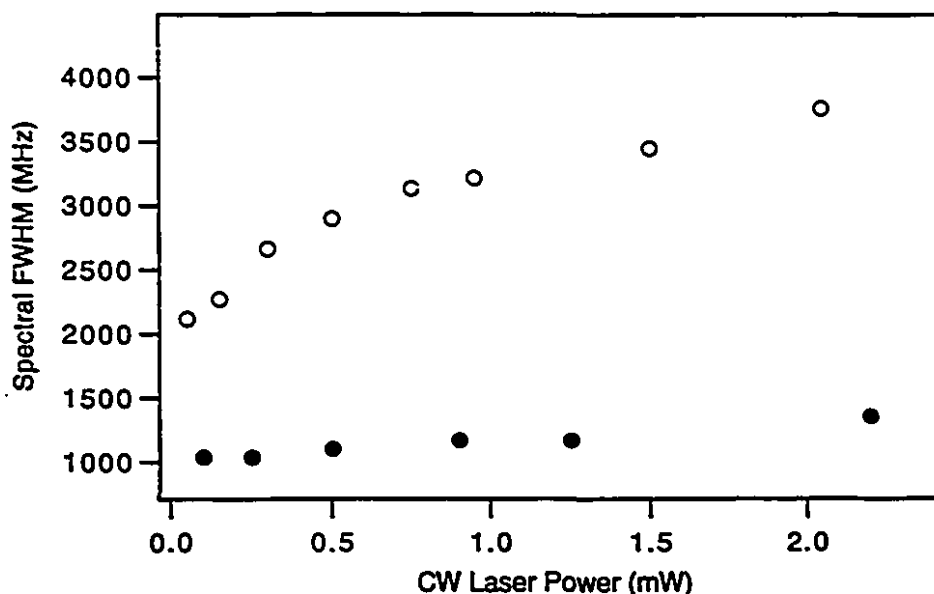
Figure 5.13: Spectral linewidth versus cw uv probing laser power. The measurements were done by full cycle LIF method as well as coincidence counting at zero RF phase.

saturation effect. The linewidth from the spectra at zero RF phase is also shown, which does not change much with the increase of the laser power. However, due to the quenching rate-limited saturation effect, the LIF counting rate is actually reduced by a factor of two at high laser power (1 mW), compared with the one employing phase-locked laser excitation.

It should be emphasized that this kind of saturation effect is not the conventional laser power broadening of an individual transition. It is actually due to the collisional quenching rate-limited process. If laser spectroscopic studies are carried on a two-level system, such kind of saturation effect will disappear. In our Hf^+ experiment, laser modulation can reduce this optical pumping related saturation effect by eliminating unnecessary optical pumping. In addition it can reduce the chemical

Isotope	^{180}Hf	^{179}Hf	^{178}Hf	^{177}Hf	^{176}Hf	^{174}Hf
Natural Abundance (%)	35.2	13.74	27.1	18.6	5.2	0.16

Table 5.1: Natural abundances of hafnium isotopes.

formation of HfH.

5.7 Application to Laser Spectroscopic Studies of Hf isotopes

As discussed in previous sections, phase-selective spectroscopic method at zero RF phase by using cw laser modulation together with coincidence counting can greatly improve the spectroscopic resolution. A spectral resolution of 1 GHz (FWHM) can be obtained. This width corresponds to a slightly higher temperature than the room temperature. It is found that this spectral resolution is relatively fixed when the trapping parameters are changing.

It should be mentioned that phase-selective LIF can also improve the signal to background ratio. The typical background counting rate due to the cw uv incident beam is about 1000 cps. With the coincident gate width of 150 ns, the background counting rate can be reduced to 60 cps. On the other hand, the LIF counting rate obtained by using phase-selective LIF at zero RF phase is typically reduced only by a factor of 4 compared with the full cycle laser spectroscopy. It has been found that about 10 ions of ^{178}Hf isotope in the trap can yield a signal-to-noise ratio 1:1.

Phase-selective laser spectroscopy makes it possible to investigate the hyperfine structure and isotope shifts of Hf$^+$ ions confined in the trap. First, laser spectroscopic measurements were carried out using a stable hafnium metallic sample, containing several stable Hf isotopes with natural abundances as tabulated in Table 5.1. The resultant spectrum is shown in Fig. 5.14, where the peaks of ^{178}Hf and ^{180}Hf are well resolved. However the hyperfine structures of ^{177}Hf and ^{179}Hf mix with each other and bury the contribution from low abundance ^{176}Hf. Further studies were needed to understand the hyperfine structures of both ^{177}Hf and ^{179}Hf.

71
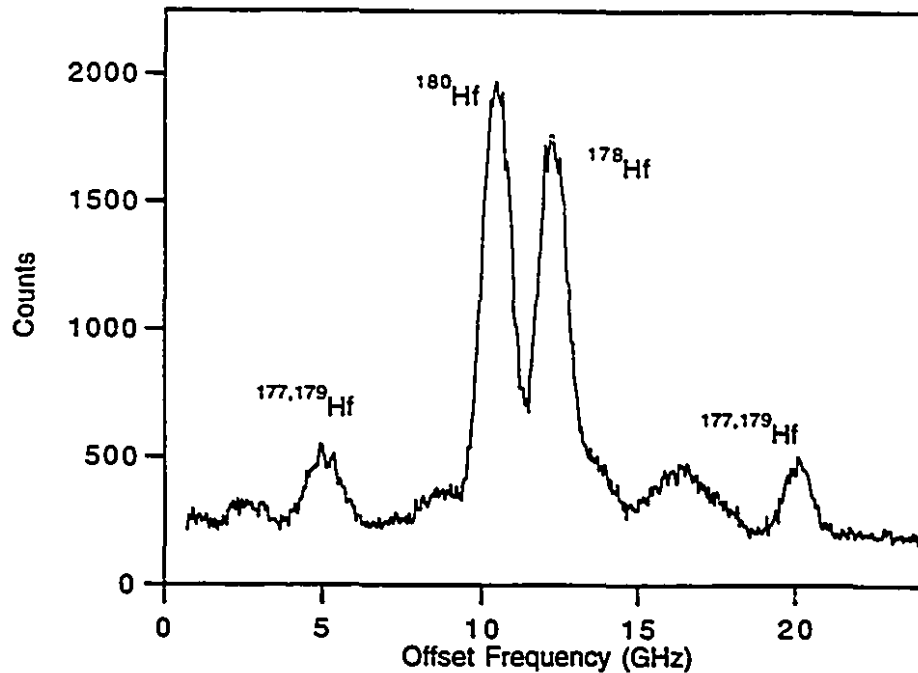
Figure 5.14: Laser spectra obtained from a stable Hf sample.

In summary of the previous chapters, the high sensitivity of the laser spectroscopy together with 1 GHz (FWHM) optical resolution, coupled with the ability to accumulate ions of interest from a weak source make it possible to carry out laser spectroscopic studies of both stable and radioactive isotopes. Starting with the next Chapter, we will concentrate on studies of hyperfine structures and isotope shifts in hafnium isotopes.

Chapter 6

Hyperfine Structures in HfII

In this chapter, after a brief discussion of the basic theory of hyperfine structures, we will go into the measurement and analysis of the hfs of ^{177}Hf and ^{179}Hf. The hfs A, B factors of ^{177}Hf and ^{179}Hf for the two energy levels $a\,^2D_{3/2}$ and $z\,^4F^o_{5/2}$ in HfII have been first deduced by a curve fitting, together with determining the centroids of the hyperfine transitions. From the A, B values, $\overline{H(0)}$ and $<\varphi_{zz}(0)>$ produced by the electrons at the nucleus have been deduced with the known nuclear moments. In addition, our analysis method is found to be very useful to extract weak signals buried under the hyperfine structures of ^{177}Hf and ^{179}Hf.

6.1 Hyperfine Structure

The hyperfine structure (HFS) is due to the interaction between the electrons and the nucleus with finite size. Because of the small ratio of nuclear to atomic radius, it converges very rapidly with powers of this ratio. Thus, besides the leading electric-monopole interaction, only the magnetic-dipole and an electric-quadrupole interactions are of practical importance. Nuclei with non-vanishing magnetic moment μ_I and electric quadrupole moment Q undergo an additional interaction with the electron shell [34]

$$W = W_\mu + W_Q = -\boldsymbol{\mu} \cdot \boldsymbol{H}(0) + \frac{1}{6}\sum_{\alpha\beta} Q_{\alpha\beta}\frac{\partial^2\varphi}{\partial r_\alpha \partial r_\beta} \tag{6.1}$$

where α and β can be x, y or z representing the Cartesian coordinates fixed in space. Here $\boldsymbol{H}$ and φ are respectively the intensity of the magnetic field and the

electrostatic potential created by the electrons at the nucleus. The interaction (6.1) leads to a splitting of a level with angular momentum J into a number of components each of which corresponds to a definite value of the total angular momentum of the atom F.

$$F = I + J \tag{6.2}$$

This splitting is called hyperfine splitting.

6.1.1 Nuclear Magnetic Moments

The magnetic moment of a nucleon is made up of the orbital and spin magnetic moments

$$\mu = g_l l + g_s s \tag{6.3}$$

It is customary to express the magnetic moments of nuclei in nuclear magnetons, i. e. in the units $\mu_N = e\hbar/(2m_p c)$ where m_p is the mass of the proton.

The mean value of μ in a nuclear state with a given value of nuclear spin I is directed along I, therefore $<\mu>$ can be expressed in terms of I

$$<\mu> = g_I I \tag{6.4}$$

The factor g_I is called the gyromagnetic ratio. Magnetic moment of the nucleus is usually understood to be the maximum projection of the magnetic moment in the direction of a field

$$\mu_I = g_I I \tag{6.5}$$

6.1.2 Quadrupole Moments

The electric quadrupole moments $Q_{\alpha\beta}$ are the next important electromagnetic property of a nucleus. In nuclear physics, the operator of the quadrupole moments is the sum over all the protons of the nucleus and is usually expressed as

$$Q_{\alpha\beta} = \sum (3 r_\alpha r_\beta - \delta_{\alpha\beta} r^2) \tag{6.6}$$

The magnitude of the quadrupole moment is given by the mean value of the component Q_{zz} in the state $|I, M = I>$. This magnitude is denoted as

$$Q = <\gamma I M | Q_{zz} | \gamma I M >_{M=I} \tag{6.7}$$

74

where γ represents the spacial dependence of a particular nuclear state. This quadrupole moment can also be called the spectroscopic quadrupole moment Q_s.

In many cases, intrinsic quadrupole moment Q_0 is used. which is determined in a system of coordinates fixed on the nucleus. The quantities Q_s and Q_0 are connected in the following way

$$Q_s = \frac{I(2I-1)}{(I+1)(2I+3)} Q_0 \tag{6.8}$$

From eqn. (6.8), it can be seen that the spectroscopic quadrupole moments only exist for nuclei with spin $I \geq 1$.

6.1.3 Hyperfine Splitting

The first term in eqn. (6.1) is due to the interaction between the nuclear magnetic moment and the electron shell. The mean value of H in a state with a given value of J is directed along J and so

$$W_\mu = -g_I \, \mathbf{I} \cdot a\mathbf{J} = \frac{1}{2}A\{\mathbf{F^2} - \mathbf{J^2} - \mathbf{I^2}\} \tag{6.9}$$

and

$$< \gamma JIFM|W_\mu|\gamma JIFM > = \frac{1}{2}A\{F(F+1) - I(I+1) - J(J+1)\} \tag{6.10}$$

where

$$A = \mu_I \overline{H(0)}/(IJ) \tag{6.11}$$

is the magnetic dipole coupling constant, $\overline{H(0)}$ is the magnetic field produced by the electrons at the site of the nucleus.

The hyperfine splitting from the second term in eqn. (6.1) can be found by averaging over

$$W_Q = \frac{1}{6}\sum_{\alpha\beta} Q_{\alpha\beta}\frac{\partial^2\varphi}{\partial r_\alpha \partial r} \tag{6.12}$$

and

$$< \gamma JIFM|W_Q|\gamma JIFM > = B\frac{\frac{3}{4}K(K+1) - I(I+1)J(J+1)}{2(2I-1)(2J-1)IJ} \tag{6.13}$$

where

$$K = F(F+1) - I(I+1) - J(J+1) \tag{6.14}$$

and B is the electric-quadrupole coupling constant

$$B = eQ_s < \varphi_{zz}(0) > \qquad (6.15)$$

Here $< \varphi_{zz}(0) >$ is the electric-field gradient produced by the electrons at the site of the nucleus.

Thus the full expression for the hyperfine splitting of a level has the form [48]

$$W(F) = AK/2 + B\frac{\frac{3}{4}K(K+1) - I(I+1)J(J+1)}{2(2I-1)(2J-1)IJ} \qquad (6.16)$$

and a hyperfine transition frequency from F to F' can be written

$$\nu_i = \nu_c + W(F') - W(F) \qquad (6.17)$$

where $|F' - F| \leq 1$, ν_c is the center of gravity of the corresponding transition.

The relative line strength of an electric dipole transition between the hyperfine structure components of two different γJ and $\gamma' J'$ is determined by the expression in terms of 6j-symbols [34]

$$R(IJF \rightarrow IJ'F') = (2F+1)(2F'+1)\left\{ \begin{array}{ccc} J & F & I \\ F' & J' & 1 \end{array} \right\} \qquad (6.18)$$

The numerical values of the relative hfs intensities, for I and J between 1/2 and 9/2, are tabulated in [48].

6.1.4 Extracting Nuclear Moments from A and B Factors

From the hyperfine spectrum the A and B factors can be extracted, which contains the information about the nuclear moments as well as $\overline{H(0)}$ and $< \varphi_{zz}(0) >$ produced by electrons at the nucleus. After the A, B factors have been found, $\overline{H(0)}$ and $< \varphi_{zz}(0) >$ need to be determined before one can determine the nuclear moments. On the other hand, if the nuclear moments of a particular isotope have been measured by a method other than laser spectroscopy, $\overline{H(0)}$ and $< \varphi_{zz}(0) >$ can then be deduced from eqns (6.11) and eqn (6.15), respectively. Since $\overline{H(0)}$ and $< \varphi_{zz}(0) >$ are the same for all the isotopes, the following relations can be found for different isotopes i and j from eqn (6.11) and eqn (6.15),

$$\frac{A_i}{A_j} = \frac{\mu_{Ii} I_j}{\mu_{Ij} I_i} \tag{6.19}$$

and

$$B_i / Q_{si} = B_j / Q_{sj} \tag{6.20}$$

It should be noted that eqn (6.19) is only valid when the differential "hyperfine anomaly" between the two isotopes can be neglected. The treatment given for the magnetic interaction in section 6.1.3 is only valid for the ideal case of a point nucleus. For an extended nucleus, we rewrite the hyperfine constant A in eqn (6.11) as [49]

$$A = \mu_I \frac{\overline{H(0)}}{IJ}(1 - \delta)(1 - \varepsilon) \approx \mu_I \frac{\overline{H(0)}}{IJ}(1 - \delta - \varepsilon) \tag{6.21}$$

The first correction δ takes account of the extended charge distribution of the nucleus which changes the electronic wave-function. This is known as the Breit-Rosenthal effect. The second correction ε is due to the finite distribution of magnetic moment over the volume of the nucleus and is known as the Bohr-Weisskopf effect. The differential "hyperfine anomaly" between the two isotopes is defined as

$$\Delta_{ij} = (\delta_i - \delta_j) + (\varepsilon_i - \varepsilon_j) \tag{6.22}$$

Since $\overline{H(0)}$ is the same for different isotopes, from eqn. (6.21) we can form the ratio

$$\frac{A_i}{A_j} = \frac{\mu_{Ii} I_j}{\mu_{Ij} I_i}(1 - \Delta_{ij}) \tag{6.23}$$

Δ_{ij} is usually less than 1% and it often vanishes within the experimental limits of error, although δ and ε can be as high as a few percent [48]. In the ground state $^3F_2$ of HfI, $^{177}\Delta^{179}$ ($^3F_2$)= $-2.4(2.2) \times 10^{-3}$ [50, 51].

6.2 HFS Spectra in ^{177}Hf and ^{179}Hf

6.2.1 Nuclear Moments of ^{177}Hf and ^{179}Hf

For ^{177}Hf and ^{179}Hf, quite a few hfs measurements have been reported in atomic transitions [50, 51, 52, 53]. The nuclear moments of ^{177}Hf and ^{179}Hf have been deduced in previous works. The accepted values [54] are

$$\mu_I^{177} = +.7935(6) \ \mu_N \qquad \mu_I^{179} = -.6409(13) \ \mu_N[50] \tag{6.24}$$

and

$$Q_S^{177} = +3.365(29) \text{ b} \qquad Q_S^{179} = +3.793(33) \text{ b}[55] \qquad (6.25)$$

Büttgenbach *et al.* measured the magnetic moments using the atomic beam magnetic resonance method (ABMR) [50]. In their work, hyperfine constants A, B of the ground state of HfI have been determined with accuracies better than 4×10^{-6}. Then the g_I factors were determined by measuring the resonance frequencies ν_1 and ν_2 of two different transitions at the same magnetic field. In [50], the electric quadrupole moments were also deduced from the theoretical expression for B. Since the electrostatic field gradient produced by electrons is difficult to compute precisely in a multi-electron system, the Q obtained in this way has a large uncertainty (10%), although the B factor has been determined very precisely.

The quadrupole moments given above in eqn (6.25) were determined by measuring the quadrupole hyperfine-splitting energies of muonic M x-rays [55]. In muonic atoms the electrostatic field gradient at the nucleus is produced by a single muon (the electronic contribution is negligibly small) and can be precisely calculated. Thus the deduced quadrupole moments have better accuracies. Ground-state quadrupole moments deduced from muonic X-ray analysis are often used in combination with electron-atom measurements to calibrate the electronic field gradient at the nucleus.

6.2.2 HFS Spectra of ^{177,179}Hf with $a\,^2D_{3/2}$—$z\,^4F^\circ_{5/2}$ in HfII

No hfs results have been reported in Hf ionic transitions prior to this work. Our studies in ^{177}Hf and ^{179}Hf measure the hfs for the ground state $a\,^2D_{3/2}$ and the excited state $z\,^4F^\circ_{5/2}$ in HfII, providing new atomic data about $\overline{H(0)}$ and $< \varphi_{zz}(0) >$ with the known nuclear moments. From our data we can deduce the centroids of the hyperfine transitions, which can be used to extract the isotope shift for the transition investigated. Furthermore, the deduced $\overline{H(0)}$ and $< \varphi_{zz}(0) >$ will be useful for our future studies of the nuclear moments of radioactive Hf isotopes through hfs measurements.

The spins of the nuclear ground states of ^{177}Hf and ^{179}Hf are 7/2, 9/2 respectively. With the optical transition $a\,^2D_{3/2}$—$z\,^4F^\circ_{5/2}$ in HfII, there should be 12

Symbol	^{177}Hf		^{179}Hf	
	$F'-F$	R	$F'-F$	R
a	1—2	23.1	2—3	33.4
b	2—2	23.1	3—3	25.7
c	2—3	15.4	3—4	21.0
d	3—2	11.5	4—3	11.0
e	3—3	33.6	4—4	37.8
f	3—4	8.6	4—5	11.2
g	4—3	31.7	5—4	31.1
h	4—4	34.2	5—5	38.1
i	4—5	3.2	5—6	4.0
j	5—4	60.9	6—5	60.6
k	5—5	23.6	6—6	26.0
l	6—5	100.0	7—6	100.0

Table 6.1: HFS components and their theoretical relative intensities of ^{177}Hf and ^{179}Hf of the transition $a\,^2D_{3/2}-z\,^4F^\circ_{5/2}$ in HfII.

hyperfine spectral lines for each of these two isotopes. Table 6.1 gives all the hyperfine components and their theoretical relative intensities for electric dipole transitions.

In the experiment, to obtain the hfs of ^{177}Hf and ^{179}Hf, enriched ^{177}HfO$_2$ and ^{179}HfO$_2$ samples were tried separately. ^{177}Hf, or ^{179}Hf ions were first loaded into the trap, followed by the scanning of the cw uv laser frequency. Phase-selective laser excitation together with coincident counting techniques were used to obtain the spectra. The hafnium spectra of the ionic transition obtained are shown in Fig. 6.1(a) and Fig. 6.2(a), respectively. The spectrum resolution of about 1 GHz is found adequate to resolve most of the hyperfine components of ^{177}Hf. Deduced hfs components are also shown in Fig. 6.1 and Fig. 6.2. The detailed analysis will be discussed in the next section.

6.3 Analysis of ^{177,179}Hf Hyperfine Structures

In this work, nonlinear curve fitting as a general method has been applied to analyze the ^{177}Hf and ^{179}Hf spectra. First of all, five unknown parameters need to be extracted in eqn (6.17). Those are A and B of the ground state, A' and B' of the excited state
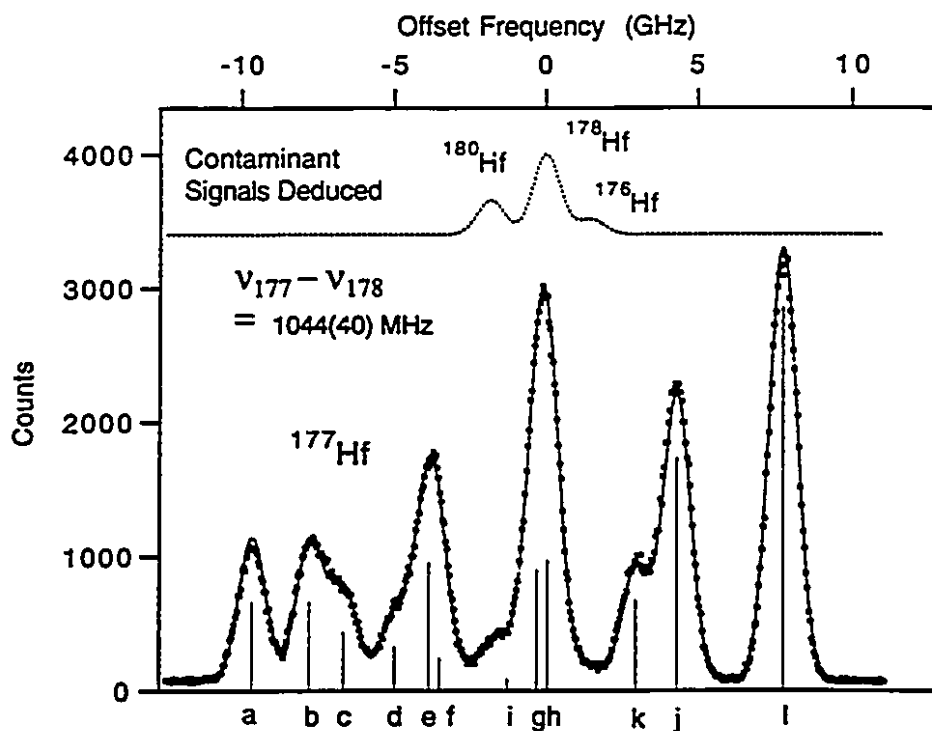
(a). The hyperfine spectrum of ^{177}Hf corresponding to the transition $5d6s^2$ ($a\,^2$D) ($J = 3/2$) — $5d6s(a\,^3$D)$6p$ ($z\,^4$F°) ($J = 5/2$). The experimental data points and the fitted curve are displayed in the diagram. The contributions of the contaminant Hf isotopes ^{180}Hf, ^{178}Hf and ^{176}Hf have been found from the curve fitting and are indicated in the upper trace. The vertical bars represent the deduced hfs lines with the theoretical relative intensities.
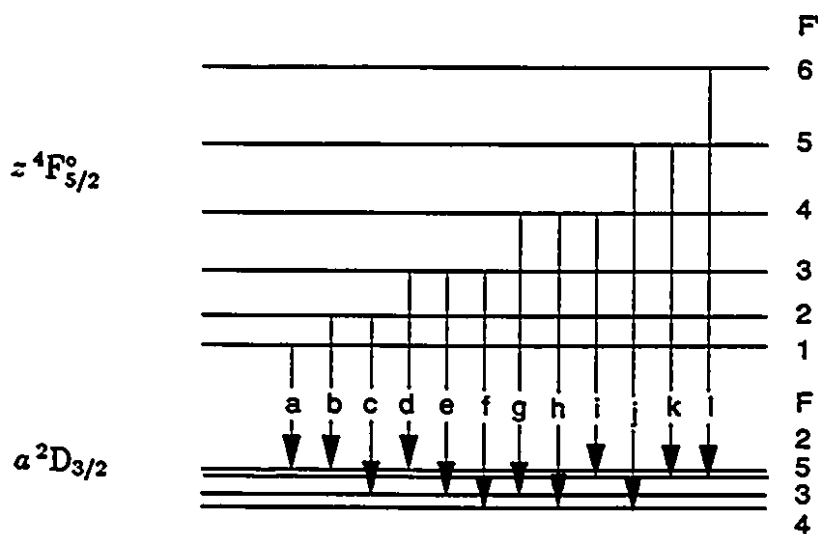
(b). Hfs splitting schemes of ^{177}Hf.

Figure 6.1: Hyperfine spectrum of ^{177}Hf.
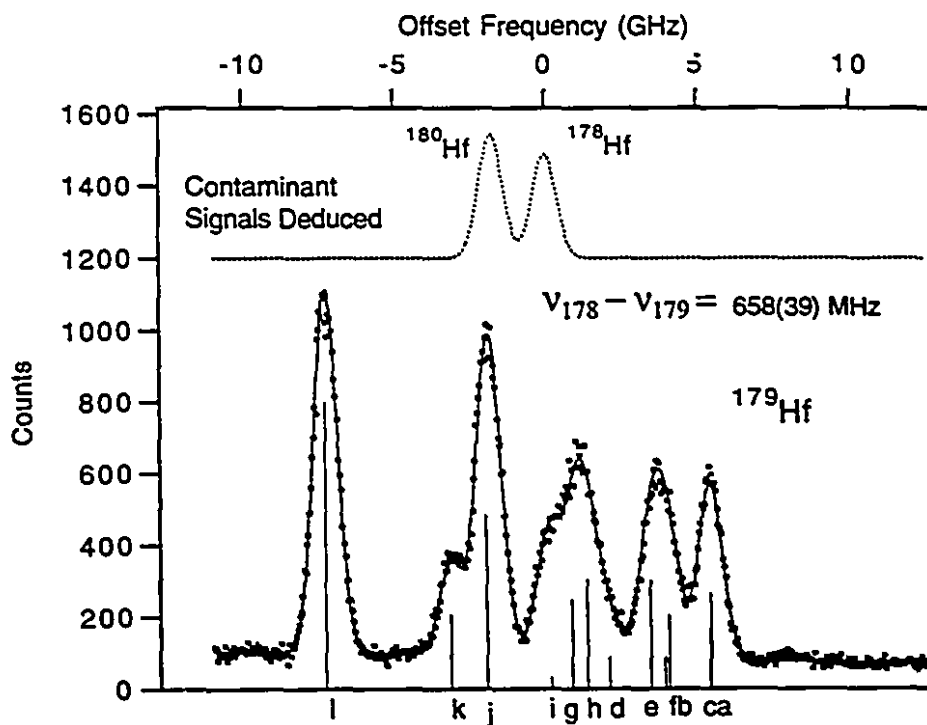
(a). The hyperfine spectrum of ^{179}Hf corresponding to the transition $5d6s^2$ ($a\,^2$D) ($J = 3/2$) — $5d6s(a\,^3$D)$6p$ ($z\,^4$F$^\circ$) ($J = 5/2$). The experimental data points and the fitted curve are displayed in the diagram. The contributions of the contaminant Hf isotopes ^{180}Hf and ^{178}Hf have been found from the curve fitting and are indicated by the upper trace. The vertical bars represent the deduced hfs lines with the theoretical relative intensities.
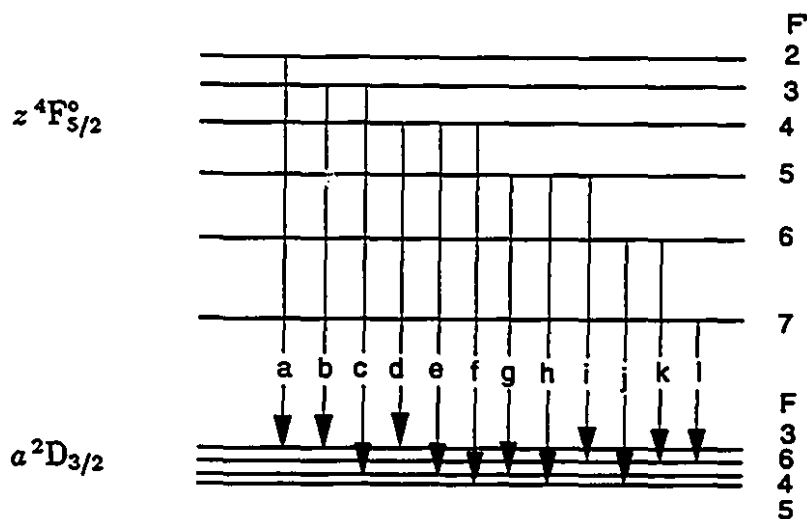
(b). Hfs splitting schemes of ^{179}Hf.

Figure 6.2: Hyperfine spectrum of ^{179}Hf.

and the spectral centroid ν_c. With assumed trial values of A, B A', B' as well as ν_c, all 12 hyperfine transition frequencies ν_i can be calculated from eqn (6.17). The line shape of a single peak can be very well represented by a Gaussian profile. The trial frequencies are then broadened with a common linewidth-related parameter Γ. A reconstructed hfs spectrum could be generated from these 12 Gaussian functions with appropriate amplitudes for each of the hyperfine components. This spectral profile can be expressed as

$$F(\nu) = \sum_{i=1}^{12} Pk_i \exp\left(-\frac{(\nu - \nu_i)^2}{2\Gamma^2}\right) + C_b \qquad (6.26)$$

where ν_i is the ith hyperfine peak position, k_i is the corresponding relative amplitude, P the amplitude for normalization and C_b the background counts. Therefore for hfs analysis, at least 8 unknown parameters need to be found from the curve fitting. Those are A, B, A', B', ν_c, P, C_b and Γ.

In the actual fitting, both the optical pumping effect and neighboring Hf isotope contaminants need to be considered. Although phase-locked excitation has been used to reduce the optical pumping effect, the measured amplitudes of different hfs lines still differ from the relative intensities given in the Table 6.1. To the first order approximation, the line intensities can be modified as

$$k_i = R_i(1 - \alpha(\nu_i - \nu_{min})) \qquad (6.27)$$

where R_i is the relative intensity found in Table 6.1 and factor α accounts for the deviation from R_i due to optical pumping, which adds one more parameter in the curve fitting.

Impurities in the enriched hafnium isotopes also affect the measured spectra. Since the neighboring even-mass isotopes, such as ^{178}Hf, ^{180}Hf and ^{176}Hf, have no hfs splitting, the contribution from small impurities can be comparable to some weak hyperfine lines in ^{177}Hf and ^{179}Hf. This means that some more Gaussian functions with trial intensities and peak positions have to be added into the spectral profile $F(\nu)$ to yield a converged fitting. The program PAW (Physical Analysis Workstation) has been used for the fitting.

82

In the parameter fitting of the hyperfine spectrum of ^{177}Hf, 15 parameters are put in the fitting line profile including six more parameters P^{176}, P^{178}, P^{180}, ν^{176}, ν^{178} and ν^{180} representing the trial contribution from ^{176}Hf, ^{178}Hf and ^{180}Hf contaminants. A successful fitting to the 512 experimental data takes about 1 hour CPU time on a Digital VAX station-4000-60 machine. All the ^{177}Hf lines plus the trial ^{176}Hf, ^{178}Hf and ^{180}Hf give us the fitted curve in Fig. 6.1(a). In the diagram the upper trace shows the contaminant contribution from even-A isotopes. From the parametric fitting, hyperfine coefficients as well as the centroids for isotope ^{177}Hf have been deduced. The results for the hyperfine constants are listed in Table 6.2. And the isotope shift between ^{177}Hf and ^{178}Hf is given in Fig. 6.1(a). The uncertainties in the extracted values are from the statistical errors, as well as the laser calibration errors (0.3%). The deduced hyperfine lines with theoretical intensities are represented by vertical bars in Fig. 6.1(a). The hyperfine splitting of the energy levels involved is given in Fig. 6.1(b).

The ^{179}Hf spectrum has also been analyzed. The result is displayed in Fig. 6.2(a). Again, the contribution from the even-A isotopes has been plotted as the upper trace. It should be pointed out that the contribution from ^{176}Hf (natural abundance 5.2%) has not been considered. Because it is 3 amu away from ^{179}Hf, its contribution is negligible. The extracted A, B factors for ^{179}Hf are also listed in Table 6.2 and the isotope shift between ^{177}Hf and ^{178}Hf is given in Fig. 6.2(a). The deduced hyperfine lines with theoretical intensities are represented by vertical bars in Fig. 6.2(a). The hyperfine splitting of the energy levels involved are given in Fig. 6.2(b).

6.4   Results and Discussions

Successful curve-fitting has been carried out in the analysis of the spectra of ^{177}Hf and ^{179}Hf, which is complicated by the moderate spectral resolution, the mixing of neighboring isotope contaminant signals and the optical pumping effect. In the curve fitting, all the experimental data are used. Therefore precise A and B values can be expected. The accuracies of all the extracted A, B, A' and B' factors are better than 2.5%. In particular the extracted A', B' values of ^{177}Hf in the excited state have

Level	Atomic mass (amu)	Magnetic hyperfine coefficient A (MHz)	Quadrupole hyperfine coefficient B (MHz)	Mean magnetic field $\overline{H(0)}$ (Tesla)	Mean electric field $< \varphi_{zz}(0) >$ (V/m^2)
$5d6s^2$	177	28.7(0.3)	1657(8)	24.9(3)	$2.04(3) \times 10^{22}$
$(a\,^2D_{3/2})$	179	$-17.5(0.9)$	1928(21)	24.2(1.3)	$2.11(4) \times 10^{22}$
$5d6s(a\,^3D)6p$	177	853(3)	$-648(6)$	1235(5)	$-8.00(12) \times 10^{21}$
$(z\,^4F^o_{5/2})$	179	$-540(2)$	$-728(17)$	1243(7)	$-7.96(25) \times 10^{21}$

Table 6.2: Hyperfine coefficients and electro-magnetic field parameters $\overline{H(0)}$ and $< \varphi_{zz}(0) >$ at the nucleus.

accuracies of 0.4% and 1% respectively, which can be used for the future analysis of the nuclear moments of radioactive hafnium isotopes through hfs studies.

From the known nuclear magnetic dipole and electro-quadrupole moments, $\overline{H(0)}$ and $< \varphi_{zz}(0) >$ can be calculated according to eqn (6.11) and eqn (6.15) (omitting the δ and ε corrections), providing new atomic data for the two energy levels $a\,^2D_{3/2}$ and $z\,^4F^o_{5/2}$ in HfII. All these results are summarized in Table 6.2. The good agreement between the two isotopes for the deduced $\overline{H(0)}$ and $< \varphi_{zz}(0) >$, through independent fitting, lends credence to our hfs analysis.

It can be seen from Table 6.2 that the magnetic field at the nucleus produced by the electrons is quite different between the excited state and the ground state. The $\overline{H(0)}$ produced by the excited state is about 50 times bigger than that produced by the ground state, resulting in a big hyperfine splittings in the excited state. This can be understood by the their electron configurations. In the ground state, the contribution is mainly from the d electron, since the two equivalent s electrons have their spins paired. In the excited state, all three electrons including an s electron can contribute. Generally the nuclear magnetic fields for s electron are considerably bigger than p and d electrons, since s electron is more likely to be close to the nucleus. The gradients of the electric fields $< \varphi_{zz}(0) >$ created at the nucleus by the electrons are similar for the two states. In fact, the spherically symmetric charge distribution of the s electron will not contribute to $< \varphi_{zz}(0) >$.

The $\overline{H(0)}$ and $< \varphi_{zz}(0) >$ from the ground state $d_{3/2}$ electron can be estimated semi-empirically using the formula given by [48]

$$< \varphi_{zz}(0) > = k_c^{-1} e \frac{2j-1}{2j+1} \frac{1}{< r^3 >} R_r(l,j) \tag{6.28}$$

where $k_c^{-1} = 4\pi\varepsilon_0$ and $R_r(l,j)$ is a relativistic correction tabulated in [48] with 1.24 for a $d_{3/2}$ electron. The value $\overline{r^{-3}}$ can be obtained from the fine structure splitting $\delta W^0 = 3050.9$ cm^{-1} [56] by

$$\frac{1}{< r^3 >} = k_m^{-1} \frac{\delta W^0}{2\mu_B^2(l+1/2)Z_i H_r(l,Z_i)} \tag{6.29}$$

where $k_m^{-1} = \mu_0/4\pi$, μ_B is the Bohr magneton, Z_i is the effective nuclear charge seen by the electron while inside the electric core and $H_r(l,Z_i)$ is a relativistic correction of 1.03 [48]. It has been found empirically [57] that for an s-orbit $Z_i = Z$, for a p-orbit $Z_i = Z - 4$ while for a d-orbit, $Z_i = Z - 11$. From these values, we obtain $< \varphi_{zz}(0) > = 1.60 \times 10^{22}$ V/m^2. The calculated $< \varphi_{zz}(0) >$ is very close to the value measured from our experiment. About the magnetic field, omitting the δ corrections, the formula can be expressed by [48]

$$\overline{H(0)} = \frac{\delta W^0 l(l+1) F_r(j,Z_i)}{Z_i(l+1/2)(j+1)\mu_B H_r(l,Z_i)} \tag{6.30}$$

where $F_r(j,Z_i)$ is another relativistic correction with a value 1.08 [48] in our case. From the calculation, it is found $\overline{H(0)} = 108$ T. This is about 4 times bigger than the experimental result. However, this simple estimation can give us the correct order of the magnitude about $\overline{H(0)}$ and $< \varphi_{zz}(0) >$ of the ground state.

Finally it should be emphasized that the curve fitting is a very powerful method to unravel the complex spectrum. It allows very weak signals to be extracted. This fact has been demonstrated in the analysis of [177]Hf, where very weak signal from [176]Hf isotope has been successfully deduced. This is very important in the studies of radioactive isotopes, where the dilute radioactive source is often contaminated with stable hafnium isotopes. Further application of curve fitting has been used in the analysis of spectra containing a weak signal from the radioactive isotope [172]Hf, which will be presented in the next chapter.

Chapter 7

Radioactive ^{172}Hf Measurement

In this chapter the radioactive isotope ^{172}Hf measurement is described. The feasibility of our setup to study radioactive isotopes has been demonstrated. The ^{172}Hf ions can be accumulated inside the trap from a weak radioactive source. The overall efficiency of ion injection into the trap from the radioactive sample has been estimated to be better than 10^{-7}. For laser spectroscopic studies, with 20 ions of ^{172}Hf confined in the trap, precise measurement of isotope shift between ^{172}Hf and ^{178}Hf has been performed. In the experiment, it has been found that the radioactive sample used contained strong stable Hf contaminants. An isotope-selective suppression technique has been used to further improve the spectrum of ^{172}Hf.

7.1 ^{172}Hf Sample

7.1.1 Production and Preparation

Radioactive isotope ^{172}Hf has a half life of 1.87 years. The sample used in the experiment was prepared at Institut de Physique Nucléaire, Orsay, France. The ^{172}Hf was produced during production of the high spin isomer ^{178}Hf^{m2} ($T_{1/2} = 31$ years, $I^\pi = 16^+$). The reaction ^{176}Yb(α, 2n) was chosen to produce ^{178}Hf^{m2} [58]. A Yb$_2$O$_3$ target with ^{176}Yb 96% enrichment was used, and the incident α particle energy was 35 MeV. During those production runs, micro-weight quantities of ^{178}Hf^{m2} were produced. At the same time, several other hafnium isotopes including ^{172}Hf were produced from (α, xn) reactions on the contaminant Yb isotopes. Chemical separation of hafnium isotopes from the bulk of the reaction products was carried out by selec-

^{172}Hf Decay		^{172}Lu Decay	
Photon Energy (keV)	Absolute Intensity (%)	Photon Energy (keV)	Absolute Intensity (%)
6.753	1.9±.7	7.411	18.5±1.5
7.650	46±16	8.510	18.9±1.6
8.834	42±17	9.845	3.0 ±0.3
10.248	7±3	51.354	32.1±2.2
23.99	20.3±1.1	52.389	57±4
52.965	33±6	59.316	18.0±1.2
54.070	57±11	61.229	4.9±0.4
61.219	18±4	78.792	11.0±0.4
63.200	4.9±1.0	90.665	5.1±0.3
67.35	5.3±.6		
81.75	4.52±.23		

Table 7.1: Photon energies and relative intensities from decays of ^{172}Hf and ^{172}Lu.

tive chromatographic extraction. Then mass separation was performed and different hafnium radioactive isotopes were collected on Cu foils of high purity (99.99%). For our experiment, the Cu foil containing ^{172}Hf was dissolved in nitric acid and the ^{172}Hf fraction was extracted and deposited on a graphite substrate within an area of 3 mm in diameter. The prepared sample was then transported to Montreal for our measurements.

7.1.2 Radioactivity of the Sample

^{172}Hf decays to ^{172}Lu through electron capture. ^{172}Lu is also a radioactive isotope, decaying again through electron capture, to stable isotope ^{172}Yb with a half life of 6.70 d. After the fabrication of the ^{172}Hf sample, the activity of ^{172}Lu was gradually increasing. At the time when we carried out our measurement one month later, the radioactivity of ^{172}Hf and ^{172}Lu were almost equal. These decay processes result in the emissions of many γ rays and X-rays. Low energy photon emissions (less than 100 keV), together with their intensities are listed in Table 7.1 [59]. Transitions whose absolute intensities below 1% are not shown.

A NaI scintillator detector is used to detect the γ radiation. Fig. 7.1 shows a γ spectrum of the source used for the spectroscopic measurement. The area of the
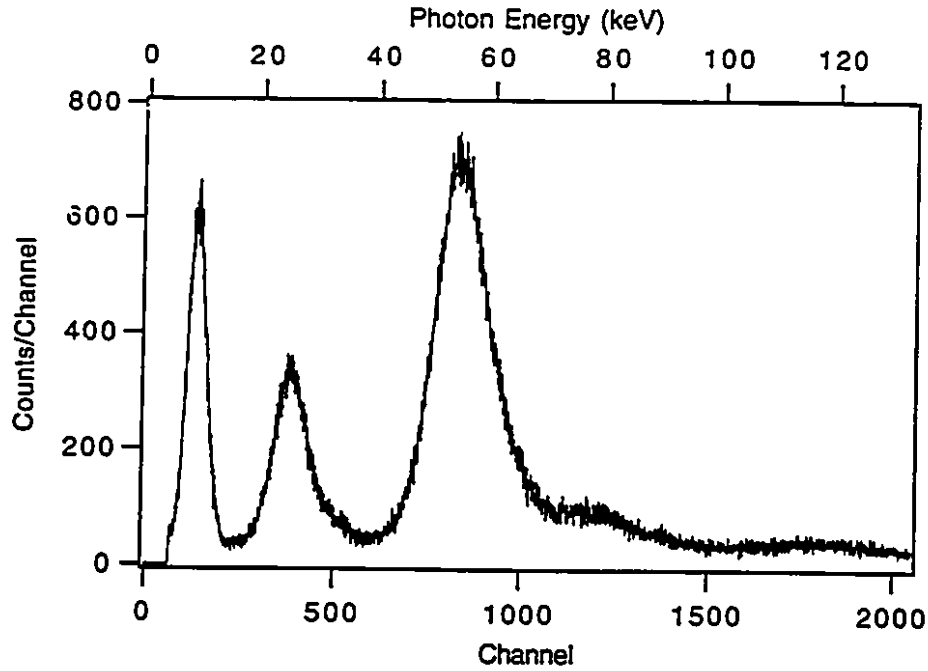
Figure 7.1: γ spectrum of ^{172}Hf measured by a NaI scintillator detector.

peaks around 55 keV has been used to estimate the absolute activity of the source. The number of the ^{172}Hf could be found from the following formula

$$N = \frac{N_c \times T_{1/2} \times 100}{\ln 2 \, \Omega \, \varepsilon_d \, I} \tag{7.1}$$

where N_c is the area counts and $T_{1/2}$ corresponding to the half life of ^{172}Hf, Ω the solid angle of the detector from the radioactive source, ε_d the efficiency of the detector, and I is the total absolute intensity of 100 disintegrations with photon energies mainly 52.965 keV, 54.070 keV, 61.219 keV in ^{172}Hf as well as 51.354 keV, 52.389 keV and 59.316 keV in ^{172}Lu. An ^{241}Am source has been used for the calibration of the detector efficiency and its energy response. In this way, the number of ^{172}Hf atoms in the radioactive source was estimated to be 7×10^{11}.

7.2 ^{172}Hf Spectrum Measurement

7.2.1 Experimental Procedures

By using our ion injection method, any hafnium isotopes in the target substrate will be desorbed and ionized by the laser pulses. As seen before, odd-mass stable isotopes ^{177}Hf and ^{179}Hf are of very complex hfs, which could cover weak signals of interest if the quantity of stable contaminants is larger than that of radioactive isotopes. Before the ^{172}Hf measurement, the trap had been used to study stable hafnium for a long time. In order to get rid of the contaminants of stable hafnium inside the system, the trap assembly had been thoroughly cleaned with an acid mixture before the radioactive ^{172}Hf sample was put in the experimental setup. The acid solution was prepared with the following proportions: 1 liter nitric acid at 54% concentration and 100 c. c. hydrofluoric acid at 65% concentration diluted into 9 liters water. Our trap electrodes had been sitting in the acid for about 10 hours to get rid of the stable hafnium contaminants. After the trap was reinstalled in the system, with the normal ion loading procedure, the Hf ion accumulation from a pure graphite substrate was not seen.

To perform laser spectroscopic study on the radioactive ^{172}Hf, the graphite substrate containing ^{172}Hf isotope was then placed on the target holder. Before the ion injection, each aspect which would affect the ion accumulation had been checked carefully, such as the operation of the trap, the buffer gas pressure, the laser beam alignments and RIS laser wavelength. During the ion accumulation with repeated desorption and RIS laser pulses, the Nd:YAG power was set just below the threshold for stable operation described in section 3.1.1, in order to maximize Hf ion production and to avoid destroying the radioactive target. The accumulation time was usually about 5 minutes with laser repetition rate of 3 Hz.

After the ions have been loaded into the trap, phase-selective LIF at zero RF phase was applied. The modulated cw laser was scanning through the resonance transition with $\lambda = 340$ nm. Each scan took about 1 min, and 10 scans were added up together to give a spectrum from the radioactive hafnium sample (Fig. 7.2). The

spectrum from stable hafnium with natural abundances is also shown in Fig. 7.2 for comparison. It can be seen that the radioactive ^{172}Hf sample contains strong contaminants from stable Hf isotopes. The signal of ^{172}Hf is found to lie near some hfs components of stable ^{177}Hf and ^{179}Hf isotopes. The enhanced ^{176}Hf in the spectrum is due to the fact that ^{176}Hf has been added to the radioactive sample during the chemical separation.

After the spectroscopic measurements, the ions were extracted by applying a negative pulse at the end-cap electrode for ion extraction. The time-of-flight spectrum indicated that about 1000 Hf ions with few contaminants had been confined in the trap. From the composition of the LIF spectrum as shown in Fig. 7.2, it can be estimated that 2% of the trapped ions were ^{172}Hf. Therefore, the ^{172}Hf peak in the laser spectrum was the contribution from about 20 ions.

7.2.2 Application of Isotope-Selective Suppression Technique

The LIF signal from radioactive ^{172}Hf is partially masked by some of the hfs lines of stable isotopes ^{177}Hf and ^{179}Hf. However it was possible to reduce the contributions from ^{177}Hf and ^{179}Hf by an isotope-selective suppression method (see section 4.3). In the experiment, the incident cw uv laser light was first tuned to the strongest hfs line of ^{179}Hf, then of ^{177}Hf for a few minutes, to selectively convert the ^{177}Hf and ^{179}Hf ions into HfH$^+$. Afterwards, The LIF measurement was carried out. Fig. 7.3 displays the spectrum after suppressing the signals from the contaminant isotopes ^{177}Hf and ^{179}Hf. This time a distinct ^{172}Hf peak is shown in the diagram. The contributions from the contaminant isotopes ^{177}Hf and ^{179}Hf have been suppressed by a factor of 4. The residual contribution from the contaminant isotopes ^{177}Hf and ^{179}Hf is due to the presence of the non-resonance photon dissociation induced by the uv probing laser beam. In fact the contaminant contribution was gradually building up during the ten-scan laser spectroscopic measurements.
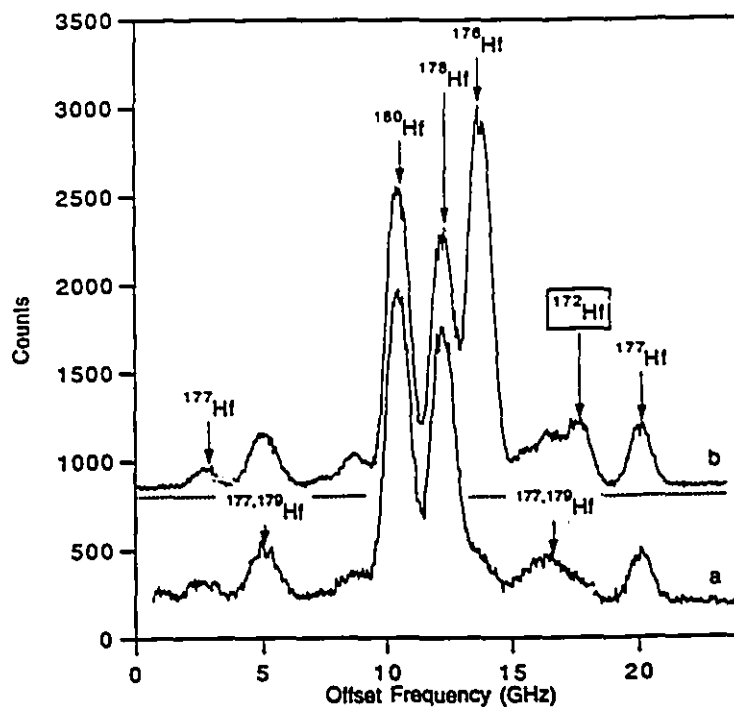
Figure 7.2: LIF spectra obtained with (a) a stable Hf sample and (b) a radioactive ^{172}Hf sample. Curve (b) has been shifted upwards and its zero level is indicated by the dotted line. The enhanced contribution of ^{176}Hf in (b) is due to the fact that ^{176}Hf has been added to the radioactive sample during the chemical separation.
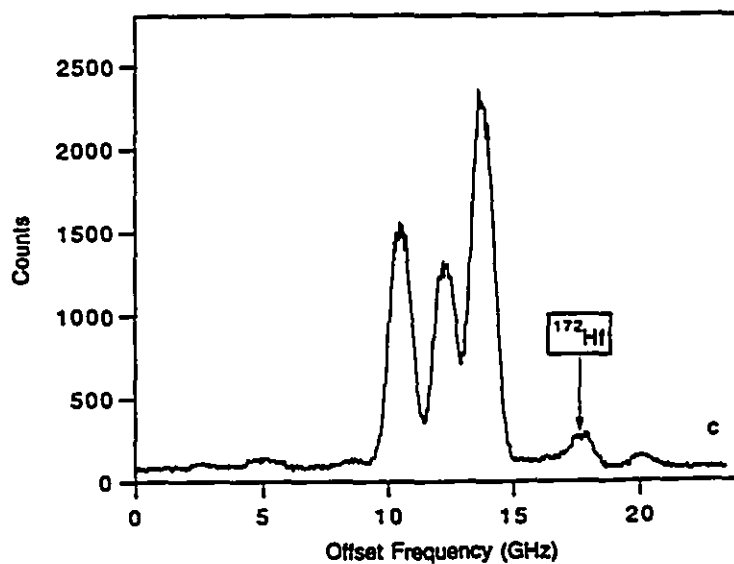
Figure 7.3: LIF spectra obtained with radioactive ^{172}Hf sample after suppression of the contaminant stable isotopes of ^{177}Hf and ^{179}Hf.

91

7.3 Result and Discussions

7.3.1 ^{172}Hf Spectrum Analysis

From the spectra containing the contribution of ^{172}Hf, one should be able to get the signal positions for the radioactive isotope ^{172}Hf as well as the centroids for the stable isotopes $^{176-180}$Hf. An analysis using curve fitting has been done on both of the spectra, with one obtained before, and the other after selective suppression of the contaminant signals of the stable isotopes ^{177}Hf and ^{179}Hf. A fitting spectral profile can be constructed, which contains all the contributions from the isotopes mentioned above. The A and B factors for the ground state and the excited state of ^{177}Hf and ^{179}Hf are fixed parameters as given in Chapter 6. The converged fitting curves have been plotted against the experimental data shown in Fig. 7.4 and Fig. 7.5. The IS between ^{172}Hf and ^{178}Hf has been derived from both spectra. Even though in Fig. 7.4, the ^{172}Hf signal is mixed with some of the hyperfine components from ^{177}Hf and ^{179}Hf, the deduced centroid of radioactive isotope ^{172}Hf is found to be consistent with the one extracted from the spectrum in Fig. 7.5. This shows that with knowledge of the hyperfine structures of ^{177}Hf and ^{179}Hf we can accurately extract the weak ^{172}Hf signal mixed with some of the hyperfine lines of the stable hafnium contaminants.

7.3.2 Sensitivity of Overall System

As stated before, our laser spectroscopic measurement was based on about 20 ions of ^{172}Hf isotope. Even though there is about 50 times as much stable Hf contamination in the ^{172}Hf spectrum, we can still extract the IS very precisely. Considering that contributions from ^{177}Hf and ^{179}Hf could be suppressed about 4 times, therefore even if the number of ^{172}Hf ions (20 ions) were reduced by 4 times, we should still be able to extract the ^{172}Hf peak by applying the isotope-selective suppression method.

The amount of ^{172}Hf can be measured through γ detection. This has allowed us to estimate the overall efficiency of our system, i. e. the ion loading efficiency from the target sample to the ions trapped. After the laser spectroscopic measurements of ^{172}Hf, it was found that less than 3% of the original activity was lost from the
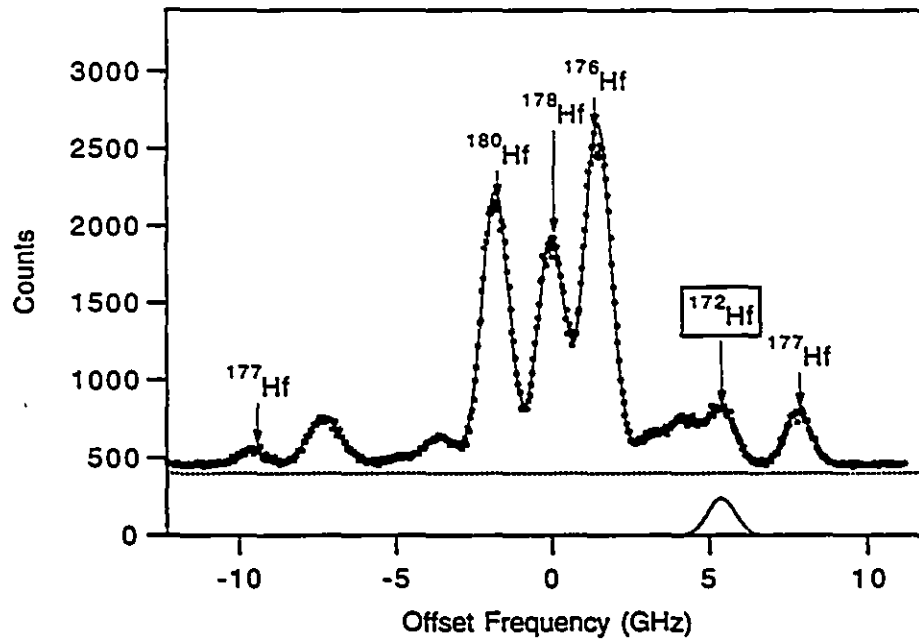
Figure 7.4: Resultant radioactive ^{172}Hf signal in the spectrum which has strong contaminants from stable isotopes of ^{177}Hf and ^{179}Hf.
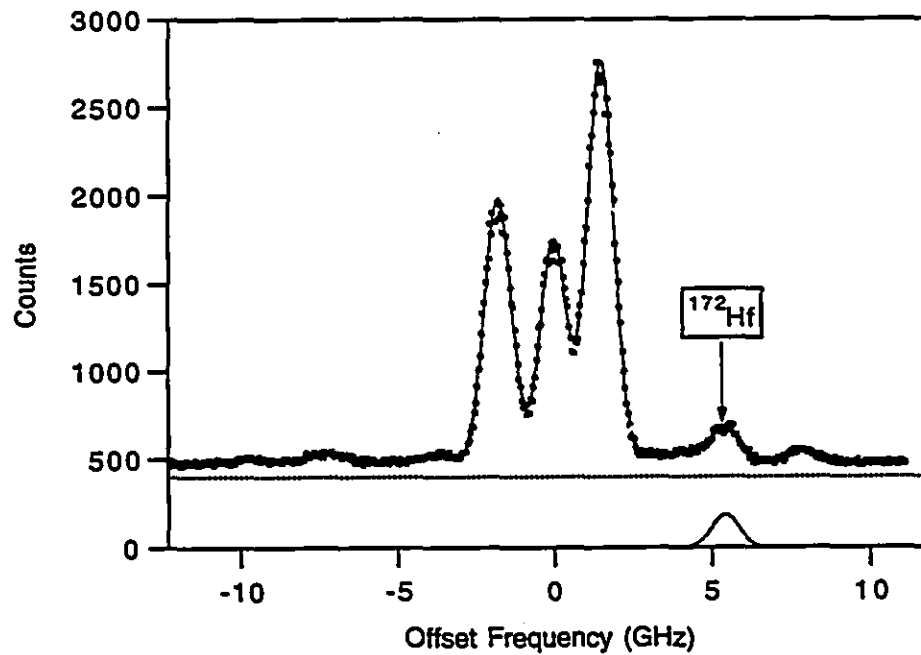
Figure 7.5: Resultant radioactive ^{172}Hf signal from the spectrum after suppression of the contaminants from stable isotopes of ^{177}Hf and ^{179}Hf.

sample. During the course of the measurements, the sample has been subjected to the production process for about 100 times. The overall efficiency for transferring Hf atoms from the target sample to ions stored in the trap can be estimated to be better than 10^{-7}. Considering the solid angle subtended by the RIS laser beams at the laser desorption point, this overall efficiency is quite consistent with the general ionization efficiency achieved by applying the RIS method to laser desorbed samples [60].

Our successful measurement of ^{172}Hf shows that using RFQ traps for laser spectroscopic studies is particularly useful when only a very limited quantity of specific material is available. However the amount of stable isotope contaminants in the sample could still be a limitation. In particular, stable isotope contaminants can give rise to more difficulties for the hfs measurement of radioactive hafnium isotopes. In addition to the isotope-selective suppression method, one possible remedy is to use ion injection and accumulations from an external source. A mass-selective injection mechanism would allow the isotope of interest be loaded into the trap, and would avoid the necessity for the production of pure mass separated target samples.

Chapter 8

$\delta < r^2 >^{AA'}$ in Hf

The isotope shifts of transition $a\,^2D_{3/2} - z\,^4F^\circ_{5/2}$ in HfII are compiled in this chapter. And the nuclear parameters have been extracted from the isotope shifts. The estimated changes in mean-square nuclear charge radii have been compared with the calculations based on the Finite-Range Droplet Model. Before going into the experimental results, some basic theory of isotope shifts is briefly discussed.

8.1 Isotope Shifts

Optical transition frequencies change slightly with respect to different isotopes. This variation is due to the change of the nuclear mass m^A and the nuclear charge distribution. The isotope shift $\delta\nu_i^{AA'}$ of a spectral line between two isotopes with mass number A and A' is made of a mass shift (MS) $\delta\nu_{i,MS}^{AA'}$ and a field shift (FS) $\delta\nu_{i,FS}^{AA'}$ [61]

$$\delta\nu_i^{AA'} = \nu^{A'} - \nu^A = \delta\nu_{i,MS}^{AA'} + \delta\nu_{i,FS}^{AA'} \tag{8.1}$$

8.1.1 The Mass Shift

The Hamiltonian of the atomic system contains the following term

$$\frac{1}{2m^A}(\sum_k P_k)^2 \tag{8.2}$$

where P_k is the momentum of the electron. The mass shift can be given by the following average value

$$\frac{1}{2}\frac{m^A - m^{A'}}{m^A m^{A'}} < (\sum_k P_k)^2 > . \tag{8.3}$$

The mass shift depends on the operator $\sum_{lm} P_l P_m$. This operator can be split into two parts: $\sum_l P_l^2$ and $\sum_{l \neq m} P_l P_m$, which are related to the so-called normal mass shift and specific mass shift, respectively. The normal mass shift $\delta\nu_{i,NMS}^{AA'}$ can be calculated unambiguously as

$$\delta\nu_{i,NMS}^{AA'} = M_{i,NMS}\frac{A'-A}{AA'} = \frac{\nu_i}{1836.1}\frac{A'-A}{AA'} \tag{8.4}$$

where $\nu_i = c/\lambda$ is the optical transition frequency. As to the specific mass shift, it is relevant to the correlation between any two electrons, leading to a collective retroaction onto the nuclear motion,

$$\delta\nu_{i,SMS}^{AA'} = M_{i,SMS}\frac{A'-A}{AA'} \tag{8.5}$$

which has the same A dependence as the normal mass effect.

8.1.2 The Field Shift

The influence of the finite extension of the nuclear charge distribution on the electronic binding energy is usually called the field shift. Generally the expression for the field shift is the following

$$\delta\nu_{i,FS}^{AA'} = F_i(Z)\lambda^{AA'} [62, 63] \tag{8.6}$$

where $\lambda^{AA'}$ is the so-called nuclear parameter approximately equal to $\delta < r^2 >^{AA'}$, and F_i is a purely electronic factor, proportional to the change of the total nonrelativistic electron density $\Delta|\psi(0)|_i^2$ at the point nucleus.

$$F_i = E_i f(Z) = \frac{\pi a_0^3 \Delta|\psi(0)|_i^2}{Z}f(Z) \tag{8.7}$$

where a_0 is Bohr radius, $f(Z)$ is the factor accounting for the relativistic correction to E_i and for the modification of the electronic wave function due to the finite nuclear charge distribution. The $f(Z)$ was taken from the theoretical isotope shift constant $C_{unif}^{AA'}$ for a uniformly charged nuclear sphere of radius $R = 1.2A^{1/3}$ fm by Babushkin [64]. Later Zimmerman et al. have reevaluated the the constant for the isotope pair A, $A+2$ [65, 66], which has been used to evaluate the $f(Z)$ tabulated in [63].

For the very heavy elements we can no longer claim the electronic wave function to be constant over the nuclear volume. It is necessary to expand the nuclear factor into a power series of radial moments which replace $\delta < r^2 >^{AA'}$ by $\lambda^{AA'}$.

$$\lambda^{AA'} = \delta < r^2 >^{AA'} + \frac{C_2}{C_1}\delta < r^4 >^{AA'} + \frac{C_3}{C_1}\delta < r^6 >^{AA'} + \cdots [67] \qquad (8.8)$$

$$= K\delta < r^2 >^{AA'} [68] \qquad (8.9)$$

The coefficients C_i have been calculated using relativistic electron wavefunctions and tabulated [66, 69], and K is close to unity and calculable [68].

8.1.3 General Procedures to Extract $\lambda^{AA'}$

The total IS can be written by

$$\delta\nu_i^{AA'} = (M_{i,NMS} + M_{i,SMS})\frac{A' - A}{AA'} + F_i\lambda^{AA'}. \qquad (8.10)$$

From a nuclear physics point of view we are interested in getting the field shifts, which can be obtained by subtracting the mass shifts. Since $M_{i,NMS}$ is a known quantity, the problem becomes to evaluate the $M_{i,SMS}$ constant. If the SMS has been determined for one line in which the FS does not vanish, then for all other lines SMS and FS can be derived by means of a King plot. For two different transitions, 1 and 2, it follows from the above equation that

$$\frac{AA'}{A' - A}\delta\nu_1^{AA'} = \frac{F_1}{F_2}\frac{AA'}{A' - A}\delta\nu_2^{AA'} + (M_{1,NMS} + M_{1,SMS}) - (M_{2,NMS} + M_{2,SMS})\frac{F_1}{F_2}. \qquad (8.11)$$

$(\frac{AA'}{A'-A}\delta\nu_1^{AA'}, \frac{AA'}{A'-A}\delta\nu_2^{AA'})$ can be plotted for all pairs AA' where data points form a straight line with slope F_1/F_2 and intersection $(M_{1,NMS} + M_{1,SMS}) - (M_{2,NMS} + M_{2,SMS})\frac{F_1}{F_2}$ on the y-axis. Thus the ratio of field shifts and the difference of mass shift factors can be extracted separately from the King plot. It is very common to make comparison of optical with electronic X-ray shifts, or Muonic X-Ray shifts.

For some particular transitions, the specific mass shift can also be estimated by the following [63]

$$\delta\nu_{SMS}^{AA'} = (0.3 \pm 0.9)\delta\nu_{NMS}^{AA'} \qquad \text{for } ns - np \text{ transitions} \qquad (8.12)$$

$$\delta\nu_{SMS}^{AA'} = (0.0 \pm 0.5)\delta\nu_{NMS}^{AA'} \qquad \text{for } ns^2 - nsnp \text{ transitions} \qquad (8.13)$$

As long as the field shifts have been determined, the electronic factor E_i must be found, before nuclear parameters can be extracted. For a transition involving the jump of an ns electron, a common approach is to evaluate the electronic factor of the outer ns electron as well as a so-called screening ratio.

$$E_i = \chi\, E_{ns} = \chi\frac{\pi a_0^3 |\psi(0)|_{ns}^2}{Z} \qquad (8.14)$$

where the screening ratio accounts for the changes in the screening of the inner s electron shells in the transition.

$$\chi = \Delta|\psi(0)|_i^2/|\psi(0)|_{ns}^2 \qquad (8.15)$$

A good estimate of the screening factor can be obtained using Hartree-Fock or Dirac-Fock methods. The E_{ns} may be estimated experimentally from the strength of the Fermi contact field $B_{ns}(0) = 2\mu_0\mu_B|\psi(0)|_{ns}^2/3$ or from the semi-empirical Landé-Goudsmit-Fermi-Segrè (LGFS) formula [48]

$$|\psi(0)|_{ns}^2 = \frac{1}{\pi a_0^3}\frac{Z_i Z_a^2}{n_a^3}\frac{dn_a}{dn} \qquad (8.16)$$

where n_a is the effective quantum number, eZ_a is the effective nuclear charge outside of the atomic core, eZ_i is the effective nuclear charge inside the atomic core and n is the principal quantum number. Both methods produce consistent and reliable values ($\pm 5\%$).

8.2 Extracting $\delta < r^2 >^{AA'}$ from IS in HfII

8.2.1 Measured Isotope Shifts in HfII

From the spectrum of the sample containing radioactive isotope ^{172}Hf, shown in Fig. 7.4, the signal centroids for the radioactive isotope ^{172}Hf as well as the stable isotopes $^{176-180}$Hf have been determined. In addition, The isotope shifts $\delta\nu^{177,178}$ and $\delta\nu^{179,178}$ have also been obtained from analysis of ^{177}Hf and ^{179}Hf spectra with enriched HfO$_2$ samples (see Fig. 6.1 and Fig. 6.2). The isotope shifts deduced have

been compiled in Table 8.1. The uncertainty of IS consists of two parts: (1) The statistical uncertainty of the peak center. (2) the uncertainty from the frequency calibration of the interferometer spectrum (0.3%).

In order to calculate the field shift which is related to the nuclear parameters, the mass shifts must first be determined. The normal mass shifts have been calculated according to eqn (8.4), and are also tabulated in Table 8.1. The determination of the specific mass shifts as well as the electric factors leading to $\delta < r^2 >^{A,A'}$ will be given in the following sections.

8.2.2 King Plot Results

King plots have been used in previous studies of hafnium isotope shifts [52, 53], in which s^2—sp transitions with nearly zero specific mass shifts (eqn 8.13) have been used as reference transitions. In our work, King plots of our transition against two previously studied Hf atomic transitions are shown in Fig. 8.1. In the diagram, $(\frac{A \times 178}{178-A} \delta\nu_1^{A,178}, \frac{A \times 178}{178-A} \delta\nu_2^{A,178})$ are plotted. The normal mass shifts in $\delta\nu^{A,178}$ have been taken away. The uncertainties of the corresponding points are also shown. The straight line is a least-squares fit taking account of the experimental errors in both axes. From the slope of the straight line and the intersection we can deduce the specific mass shift as well as the electronic factor E_i. The results have been compiled in Table 8.2. The E_i and M_{SMS} values obtained from the two different King plots agree very well. However, the uncertainties of these values appear large, mainly due to the uncertainty in our isotope shift measurements.

8.2.3 Absolute $\lambda^{AA'}$ and $\delta < r^2 >^{AA'}$

Since the transition being investigated is of the ns^2—$nsnp$ type, the specific mass shifts can be regarded to be zero with an uncertainty of half the normal mass shifts (see eqn (8.13)), which falls within the error limits given from the King plots tabulated in Table 8.2. Since the uncertainty of the theoretical prediction is much smaller, it is therefore used to evaluate the specific mass shifts. The field shifts in Table 8.1 are obtained after deducting the specific mass shifts in this way.
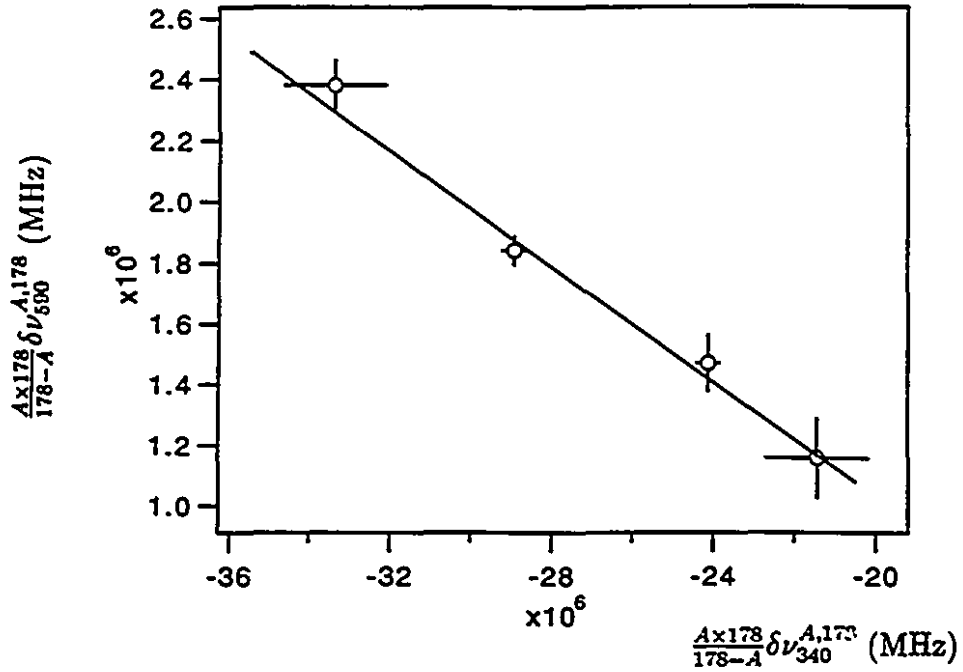
(a)
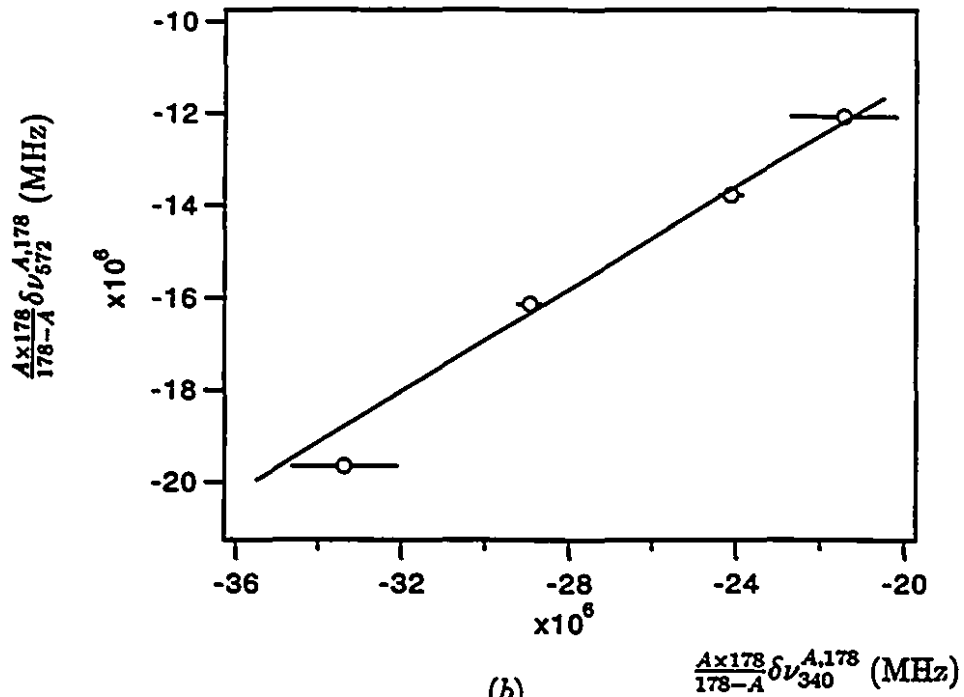
(b)

Figure 8.1: King plot of our experimental data against the results from two other transition lines (a) $d^2s^2\ a\,^3F_3$—$d^2sp\ z\,^5G_3^\circ$ in HfI (b) $d^2s^2\ a\,^3P_2$—$ds^2p\ z\,^1P_1^\circ$ in HfI. In the diagram, $(\frac{A\times178}{178-A}\delta\nu_1^{A,178}, \frac{A\times178}{178-A}\delta\nu_2^{A,178})$ are plotted. The normal mass shifts in $\delta\nu_1^{A,178}$ have been left out.

Besides the estimates from the King plots, the electric factor E_i could also be calculated by the product of an electron factor and a screen factor $E_i = \chi E_{ns}$. The E_{6s} can been determined from the HfII spectrum result presented by Finckh and Steudel [70]. In their work, $n_a^3/Z_a^2(dn_a/dn) = 1.59\pm0.03$ was given for $(5d^2\,6s)$ configuration. We can evaluate the $|\psi(0)|_{6s}^2$ in $5d^2\,6s$ by using the Gouldsmit-Fermi-Segré formula in eqn (8.16), where for s electrons, $Z_i = Z$. Furthermore, from eqn (8.14), we get

$$E_{6s} = \frac{Z_a^2}{n_a^3}\frac{dn_a}{dn} = 0.63(2) \tag{8.17}$$

In [71, 72], Aufmuth *et al.* calculated the modified total electron densities $D = 4\pi|\psi(0)|^2$ at the nucleus in HfII and HfI by means of the Hartree-Fock method. The values needed to evaluate the screening factor χ are given in Table 8.3. The χ can thus be estimated

$$\chi = -[D(5d6s^2a\ ^2D_{3/2}) - D(5d6s(a\ ^3D)6p\ z^4F^o_{5/2})]/D_{6s}(5d^26s) = -1.00 \tag{8.18}$$

with an uncertainty of 5 % from ΔD [71]. The electronic factor E_{340} can therefore be determined to be

$$E_{340} = \chi E_{6s} = -0.63(5) \tag{8.19}$$

This is in agreement with that deduced from the King plot.

With the above parameter E_{340} in eqn (8.19) and nuclear factor $f(Z)=39.908$ GHz/fm^2 [63], the absolute values of the nuclear parameter $\lambda^{A,178}$ can be calculated. By taking the K value in eqn (8.9), which is 0.95 for hafnium [68], the $\delta < r^2 >^{178,A}$ are obtained. Both $\lambda^{178,A}$ and $\delta < r^2 >^{178,A}$ are also tabulated in Table 8.1. Our results for $\delta < r^2 >^{A,178}$ are very close to those results measured by using different optical transitions [19, 52, 53]. The changes in mean-square nuclear charge radii $\delta < r^2 >$ relative to ^{178}Hf from our work have been plotted in Fig. 8.2. The results of ^{174}Hf and ^{182}Hf from the work of [52] are also displayed in Fig. 8.2.
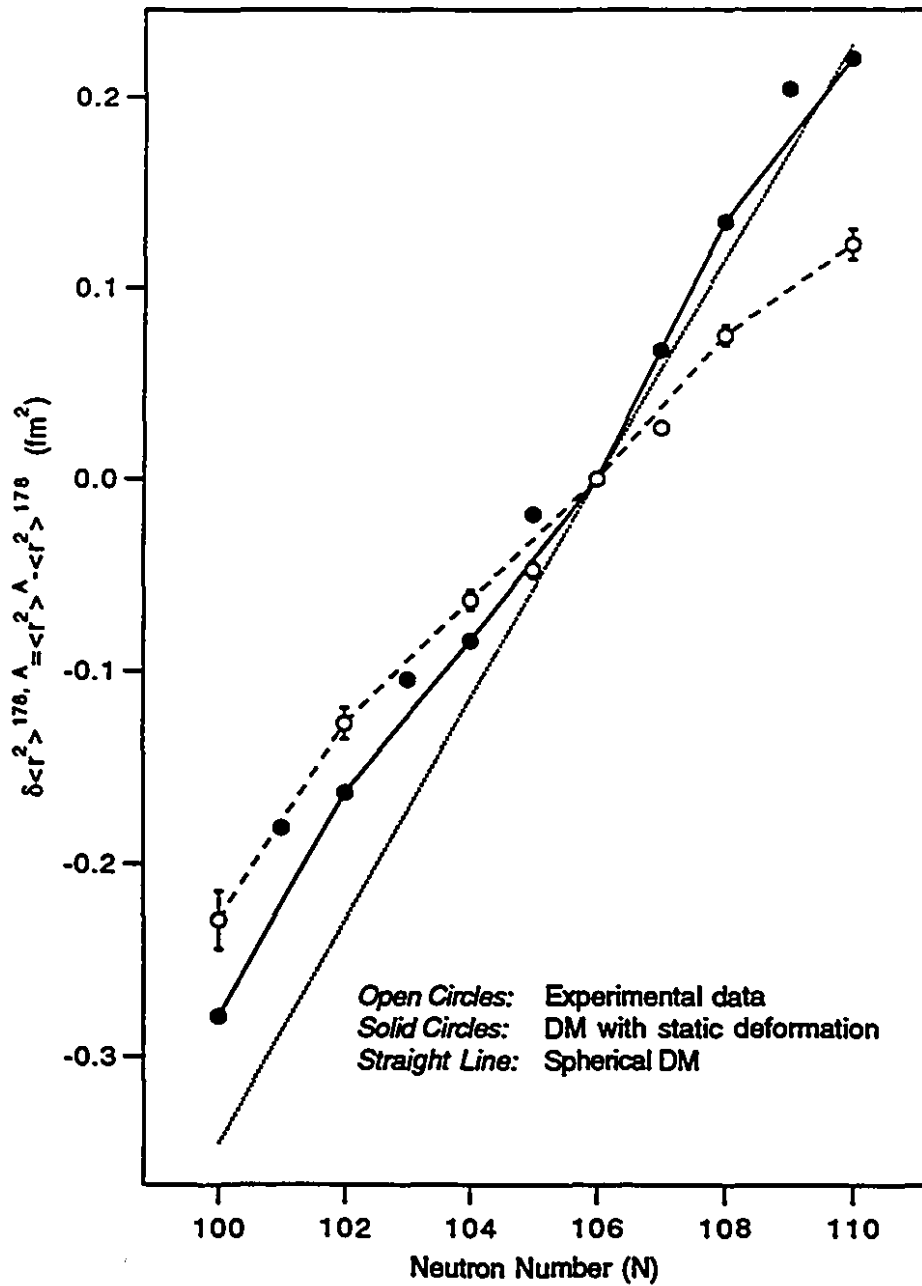
Figure 8.2: Changes of mean square charge radii in Hf isotopes. The estimates from the finite-range droplet model with static deformation parameters are plotted for comparison. Results for spherical nuclei are also shown.

A	A'	$\delta\nu^{AA'}$ (MHz)	$\delta\nu_{NMS}^{AA'}$ (MHz)	$\delta\nu_{FS}^{AA'}$ (MHz)	$\lambda^{AA'}$ (fm^2)	$\delta<r^2>^{AA'}$ (fm^2)	$\delta<r^2>_{Lit.}^{AA'}$
172	178	-5414(39)	94.2	-5508(86)	0.218(14)	0.229(15)	0.242(16) [19]
176	178	-1509(18)	30.7	-1539(34)	0.061(4)	0.064(5)	0.063(4) [52]
177	178	-1044(40)	15.2	-1059(48)	0.042(4)	0.044(4)	0.047(2) [52]
178	179	-658(39)	15.1	-673(46)	0.027(3)	0.028(3)	0.027(2) [52]
178	180	-1776(19)	30.0	-1806(34)	0.071(5)	0.076(5)	0.075(4) [52]

Table 8.1: Isotope shifts and nuclear parameters. $\delta\nu^{AA'} = \delta\nu^{A'} - \delta\nu^A$.

	Transitions	λ (nm)	M_{SMS} (MHz)	E_i
Ref. [52]	$d^2s^2\ a\,^3F_3 - d^2sp\ z\,^5G_3^o$ in HfI	590.3	$-1.8(5) \times 10^6$	$-0.094(10)$
This work	$ds^2\ a\,^2D_{3/2} - dsp\ z\,^4F_{5/2}^o$ in HfII	340	$-3(4) \times 10^6$	$0.53(10)$
Ref. [52]	$d^2s^2\ a\,^3P_2 - ds^2p\ z\,^1P_1^o$ in HfI	571.9	$-4.7(1.1) \times 10^5$	$0.55(6)$
This work	$ds^2\ a\,^2D_{3/2} - dsp\ z\,^4F_{5/2}^o$ in HfII	340	$-4(4) \times 10^6$	$0.53(10)$

Table 8.2: The specific mass shift coefficients and the electronic factors determined by King plots.

8.3 Discussions

8.3.1 Comparisons with Finite-Range Droplet Model Calculations

The droplet model seeks to describe average nuclear properties and can be used to compare experimentally measured changes of mean-square nuclear charge radii. The latest and the most refined droplet-model approach published is the finite-range droplet model (FRDM) [73], combining the droplet model [74, 75] with the folding model surface and Coulomb-energy integrals from the finite-range model [76, 77]. In addition, the finite-range droplet model contains a new exponential term with two new adjustable parameters γ and C. This leads to the substantially improved results obtained in the finite-range droplet model relative to the earlier droplet model. In its 1988 version, FRDM fits 1593 mass-data points with an rms error of 0.769 MeV, with 25 parameters being used. Recently, Buchinger *et al.* have examined the FRDM

E (cm^{-1})	Composition (%)		D (a_0^{-3})[a]	D_{6s} (a_0^{-3})
0	$5d6s^2$ (82.8)	$5d^26s$ (13.6)	536.0	
29405	$5d^26p$ (11.1)	$5d6s6p$ (89.2)	427.2	
$5d^26s$				108.3

[a] Plus an additional constant of $3\,353\,000.0$ a_0^{-3}.

Table 8.3: Modified electron densities D at the nucleus (in atomic unit) in HfII needed to calculate the screening ratio.

formula as well as the extended Thomas-Fermi mass formula, from the point of view of nuclear charge radii [78]. In our work, a calculation based on the FRDM formula has been done for Hf, following the procedure outlined in [78]. The FRDM parameters used in the calculation can be found in Appendix A.

In the calculation of $\delta < r^2 >$ of deformed nuclei with the FRDM, theoretical static deformation parameters β_2 and β_4 are first used. The calculated ground-state deformations have been obtained from [79, 80, 81] by Möller et al. [73]. The changes of mean-square nuclear charge radii from the FRDM have been plotted in Fig. 8.2 to compare with the experimental date. The results from a spherical finite-range droplet model calculation are also shown. It can be seen that the variation of calculated results accounting for deformations of nuclei follows the trend of the experimental data, though the slope from the calculation is bigger than that from the experimental data. The whole picture is that a gradual increase of the deformation from higher mass to lower mass is evident and the variation of the mean square charge radii is relatively smooth. Anastassov et al. [52] infer that their experiments indicate a change in deformation in the region $A > 174$ in Hf, which is not that obvious from our results. Also, it should be pointed out that their ^{174}Hf data point appeared to be plotted higher in their diagram than that shown in their text.

"Odd even staggering" in the changes of mean square nuclear charge radii is an important feature, which reflects the fact that the nuclear charge radii of odd-neutron isotopes are normally a bit smaller (in the order of 10^{-2} fm^2 for the ms radii) than the averages of their even-neutron neighbors. We have also observed this phenomenon.

However, the calculation from the static deformation reveals a reversed staggering, because the β_2 deformation parameters of odd-neutron isotope are bigger than the averages of their even-neutron neighbors. However, the experimental results from ^{176}Hf to ^{180}Hf apparently provide a quite normal odd even staggering. The future measurement of odd-neutron ^{173}Hf and ^{175}Hf could be very interesting to see if there is indeed reversed staggering in Hf. It has been mentioned that the β_4 parameters have been used in the calculation for nuclear charge radii. Nevertheless it is found to be only a very small modification to the final result.

The calculation using the experimental deformation β_2 given from $E2$ transition [82] has been performed. The results, together with the experimental data, are shown in Fig. 8.3. The calculated result for $\delta < r^2 >^{180,178}$ is in very good agreement with the experimental data. However there are discrepancies in the lower mass side. This is not surprising. Since the FRDM parameters were not optimized for the changes of nuclear charge radii, there are always some kinds of deviation from the experimental results of nuclear charge radii, which has been shown in [78].

8.3.2 Comparisons with Neighboring Element Yb Result

In some regions of the chart of nuclides, it has been found that the changes of nuclear charge radii of neighboring elements show "scaling behavior" of $\delta < r^2 >$, such as

$$\delta < r^2 >_Z^{N,N+2} = K(Z')\delta < r^2 >_{Z'}^{N,N+2} \, [3] \tag{8.20}$$

This kind of behavior has allowed development of a modified King plot. Fischer et al. [83] used an assumed scaling behavior of the even-N Ba and Xe isotopes to evaluate the unknown SMS in the Xe transition from the known atomic factors of Ba.

Among the elements which has been studied by laser spectroscopy in a long isotopic chain, Yb (Z=70) is lying most close to Hf (Z=72). The isotopes ^{152}Yb, $^{154-176}$Yb have been measured [3]. The changes of the mean-square nuclear charge radii $\delta < r^2 >_{Yb}^{168,A}$ from [84] are plotted in Fig. 8.4 to compare with the $\delta < r^2 >_{Hf}^{178,A}$ from N=100 to N=106. We can see a very striking similarity for the variations of the nuclear charge radii in the two elements. The variation with respect to the neutron
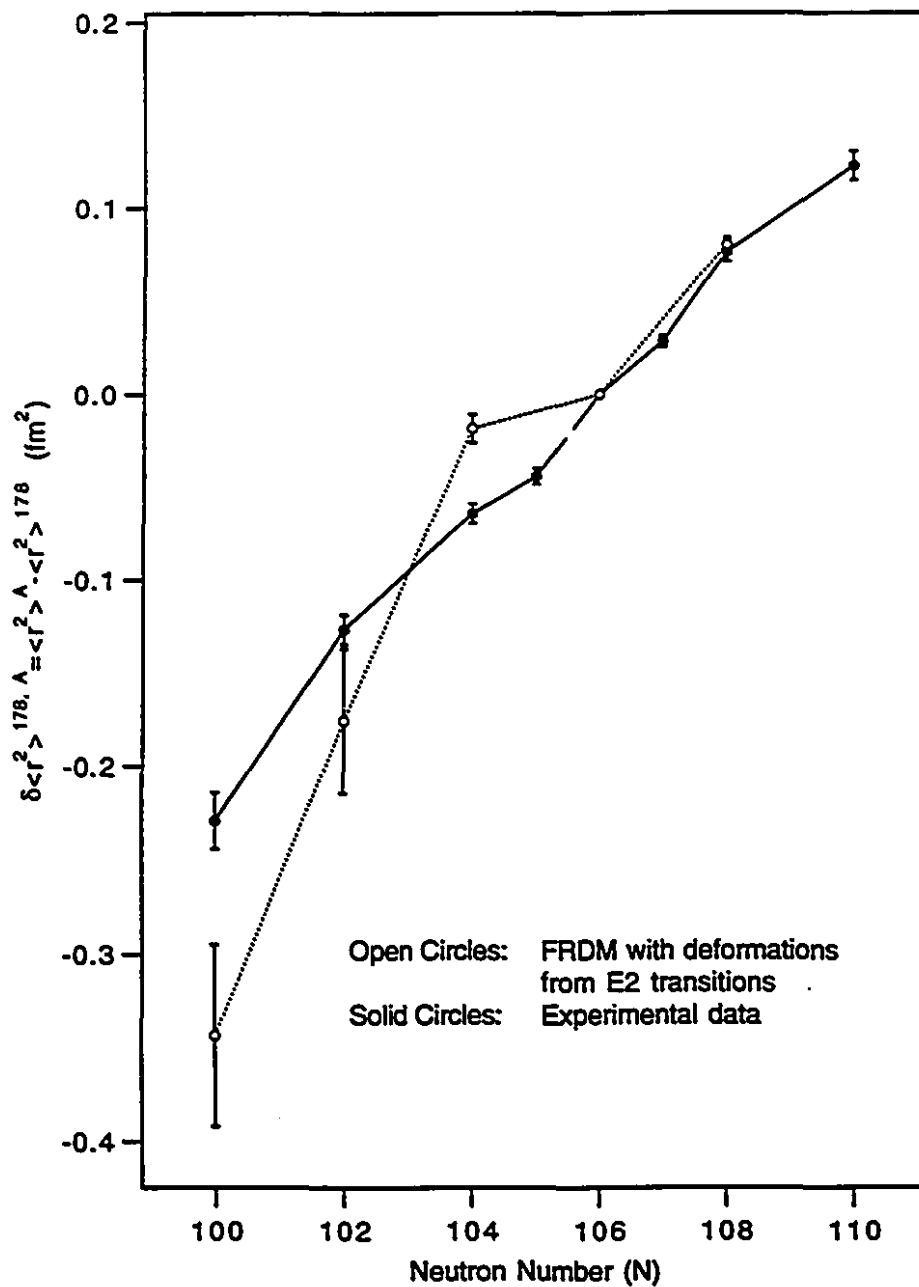
Figure 8.3: Measured changes of mean-square charge radii in Hf isotopes, which are compared with the estimates from the finite-range droplet model with deformation parameters from $E2$ transitions.
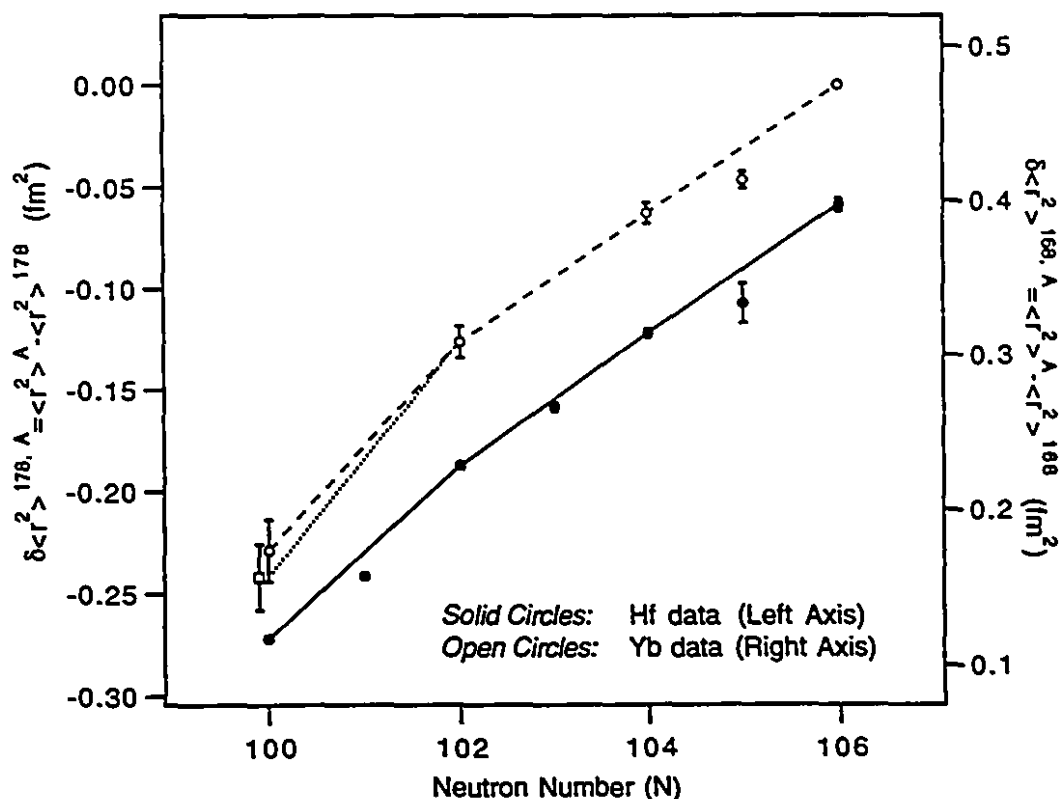
Figure 8.4: Changes of nuclear charge radii in Hf compared with those in Yb.

number is relatively smooth. And both show a very small kink at N=102. This indicates that the changes of nuclear charge radii between $N = 100$ and $N = 102$ are stronger than those for $N > 102$. In fact in the measured Yb isotopic chain [78], there is a general trend that the variation of $\delta < r^2 >$ decreases with increasing neutron number. The hafnium result has similar features. It can be seen (Fig. 8.2) that between $N = 108$ and $N = 110$, the variation of the charge radii for Hf goes lower than that for $N < 108$.

In Fig. 8.4 the result for $\delta < r^2 >_{Hf}^{178,172}$ from [19] is also shown for comparison. From their result, the change of nuclear charge radii between $N = 100$ and $N = 102$ for Hf deviates from the trend given by Yb. In their work, laser spectroscopic measurement was also carried out on trapped ^{172}Hf ions. Another optical transition $5d6s^2$ $(a\,^2D_{3/2})(E = 0$ cm^{-1}) — $5d6s(a^1D)6p$ $(z\,^2D_{3/2}^o)$ $(E = 33181$ cm^{-1}) in HfII with $\lambda = 301$ nm was used in their studies. A spectral resolution of 1.4 GHz was

obtained, and the hfs of ^{77}Hf and ^{179}Hf could not be resolved. These factors might have affected their determination of the centroid of the ^{178}Hf signal, which were mixed with the contribution from ^{177}Hf and ^{179}Hf isotopes. In our work, the hfs of ^{177}Hf and ^{179}Hf have been analyzed and the IS between ^{172}Hf and ^{178}Hf can be very reliably extracted. The determined $\langle r^2 \rangle^{178,172}$ should represent an improved and more reliable result.

8.3.3 Conclusion

We have examined the variation of Hf nuclear charge radii of ^{172}Hf, ^{174}Hf, $^{176-180}$Hf and ^{182}Hf. Among them, ^{172}Hf and ^{182}Hf are radioactive isotopes. Our measurement of ^{172}Hf updates the previous measured result. And the $^{176-180}$Hf results we obtained quite agree with those published. In the analysis, ^{174}Hf and ^{182}Hf are taken from the work of [52]. It is found that the changes of mean-square nuclear charge radii $\delta \langle r^2 \rangle^{178,A}$ gets stronger when the neutron number is decreasing. The relatively smooth variations of $\delta \langle r^2 \rangle^{178,A}$ in Hf isotopic chain are similar to those revealed in Yb. From the comparison with the FRDM, the calculation yields a correct trend for $\delta \langle r^2 \rangle^{178,A}$ in Hf isotopes. However it can not quantitatively fit the experiment results. The reversed odd even staggering from the calculation is noted, which differs from the experimental results for Hf isotopes investigated.

Chapter 9

Summary

In this work, we have developed a setup making use of a Paul trap for laser spectroscopic studies of hfs and IS of radioactive isotopes. The sample is placed near the inner surface of the ring electrode. Ion injection is realized by a Nd:YAG laser pulse to desorb the target material followed by a synchronized RIS pulse to selectively ionize the vaporized atoms inside the trap. A uv beam from an intra-cavity frequency doubler of a cw ring laser is used to probe the ions, and LIF is monitored for spectroscopic measurements. The stored ions can be extracted and their mass spectrum determined by time-of-flight detection. The system is installed in an ultra-high vacuum chamber with a base pressure better than 5×10^{-8} Pa. The setup has successfully been applied to investigate stable and radioactive hafnium isotopes. In the experiment, the HfII transition $a\,^2D_{3/2} - z\,^4F^\circ_{5/2}$ with wavelength $\lambda = 340$ nm has been used for laser-induced fluorescence measurements. Hydrogen buffer gas with a pressure of about 10^{-3} Pa is used to cool the ions and to quench the optical pumping effect. Hf ion storage times of one hour can be readily achieved with the H_2 buffer gas.

The ion injection approach makes the setup unique. Since RIS is characterized by its element selectivity and high ionization efficiency, ions of a specific element can therefore be loaded into the trap efficiently. Also, this technique allows ion accumulation in the trap from a very dilute source through successive heating and RIS laser pulses. The accumulation of hafnium ions in the trap from a weak sample has been demonstrated with an efficiency of 10^{-7}.

In the experiment, many interesting phenomena related to chemical processes

in the trap have been observed. The ion-ejection time-of-flight spectrum proves to be a convenient way to study the ion chemical conversion. Our one-hour ion storage time is limited by the chemical reaction of Hf^+ at the ground state with reactive residual gases, resulting in the formation of hafnium oxides. The decay of the LIF signal during continuous resonance excitation is found to be due to laser-induced HfH^+ formation, involving a chemical reaction from collisions between buffer gas hydrogen and Hf^+ ions in an excited metastable state. It is also observed that the HfH ions can be dissociated by laser beams. Based on the laser-induced formation of HfH^+, an isotope-selective suppression method has been developed which can be used to enhance a weak signals mixed with contributions from other contaminant isotopes.

The kinetic motion of the confined ions has been studied by LIF. The buffer gas cooling time after the creation of the ion cloud has been determined experimentally, and the ion-molecule collision cross section deduced is consistent with theoretical expectations. The ion kinetic energy dependence on various factors has been studied, including the RF phase and frequency, trap operating voltages, the number of ions trapped and buffer gas pressure. The effect of the RF phase is examined by phase locked-excitation coupled with coincidence counting. The studies clearly indicate that ion motion along the r direction reaches its minimum at zero RF phase. The statistical temperature defined by the ion motion at zero RF phase is relatively constant, slightly higher than the room temperature. However, the superposed coherent RF micro-motion very much depends on the trap operating conditions, as does the mean kinetic energy of the ions. The effect of space charge on the ion motion has also been studied. It is found that space charge will modify the shape of the phase-space diagram at different RF phases. The mean velocity of the ions increases with the increase in the number of trapped ions N. However the velocity spreads at RF phases zero and π change little.

Phase-selective LIF at zero RF phase can be used to improve the spectral resolution. A resolution of 1 GHz has been obtained which is slightly higher than the Doppler width at the room temperature (0.8 GHz for ^{178}Hf) — a factor of three improvement compared with full cycle LIF. With the improved spectral resolution,

110

hfs of ^{177}Hf and ^{179}Hf have been studied experimentally. A successful approach using non-linear curve fitting has been established to analyze the hfs of ^{177}Hf and ^{179}Hf. The hfs A and B constants for both the ground state and the excited states have been extracted. Our deduced electromagnetic fields at the nucleus provide new experimental data for atomic physics. These data can be used for studies of nuclear moments of radioactive Hf isotopes from their hfs of the same transition.

The IS of the radioactive ^{172}Hf has been carried out with a sample containing 7×10^{11} ^{172}Hf atoms. The ^{172}Hf laser spectrum has been obtained with about 20 ^{172}Hf ions mixed with about 1000 stable Hf contaminant ions in the trap. An isotope-selective suppression method has been successfully applied to the measurement of ^{172}Hf to enhance the ^{172}Hf signal by reducing the contribution from the contaminants of stable ^{177}Hf and ^{179}Hf isotopes. With the understanding of the hfs of ^{177}Hf and ^{179}Hf, the weak ^{172}Hf signal mixed in the hfs components of ^{177}Hf and ^{179}Hf can been extracted very precisely. The deduced change of nuclear charge radii $\delta < r^2 >^{172,178}$ has updated the previous measurement. Our experimental determination of the changes of mean-square nuclear charge radii with neutron number together with the existing data in the literature have been discussed and compared with the variation obtained from Finite-Range Droplet Model calculations. The measured variation is relatively smooth and is similar to that reported in neighboring element Yb.

In conclusion, this thesis covers several aspects from instrumentation development to laser spectroscopic studies of hfs and IS of stable and radioactive Hf isotopes. In addition, the experimental setup provides a means to study chemical processes and ion kinematics in the trap. With its new capability to accumulate ions of a particular element in the trap from a weak source, our setup will permit study of previously unaccessible radioactive isotopes, including refractory and transuranium elements. Further effort to develop an on-line setup would make the present setup more promising. This could further improve the ion injection efficiency and make it easier to eliminate possible contaminant isotopes before ion injection into the trap.

Appendix A

Some Parameters in Finite-Range Droplet Model

Parameter	Value		Definition of parameter
r_0	1.16	fm	nuclear-radius constant
C	230	MeV	pre-exponential compressibility-term constant
γ	1.44		exponential compressibility-term range constant
a_2	23.00	MeV	surface-energy constant
e^2	1.4399764	MeV·fm	electronic charge squared
K	240	MeV	compressibility constant
a	0.68	fm	range of Yukawa-plus-exponential potential
a_{den}	0.7000	fm	range of Yukawa function used to generate nuclear charge distribution
Q	29.4	MeV	effective surface stiffness constant
J	32.5	MeV	symmetry energy constant
L	0	MeV	density symmetry constant
$\delta < r^2 >_d$	2.9403	fm^2	$\delta < r^2 >$ from surface diffuseness
r_p	.80	fm	proton root-mean-square radius .

Table A.1: Finite-range droplet model parameters used to calculate mean-square nuclear charge radii.

Bibliography

[1] E. W. Otten, Treatise on Heavy-Ion Science vol. 8: Nuclear Far From Stability, Ed. D. A. Bromley, Plenum Press, New York (1989) Ch. 7.

[2] J. E. Crawford, in Proc. of Int. Conf. on Nucl. Shapes and Nucl. Struct. at Low Excitation Energies, Antibes, France, Ed. M. Vergnes, D. Goutte, P. H. Heenen, and J. Sauvage. Editions Frontière (1994) p. 143.

[3] J. Billowes and P. Campbell, J. Phys. G: Nucl. Part. Phys. 21 (1995) 707.

[4] E. G. Nadjakov and K. P. Marinova, At. Data and Nucl. Data Tables, 56 (1994) 133.

[5] S. L. Kaufman, Opt. Commun. 17 (1976) 309.

[6] W. A. Wing, G. A. Ruff, W. E. Lamb, J. J. Spezeski, Phys. Rev. Lett. 36 (1976) 1488.

[7] G. D. Alkhazov, A. E. Barzakh, V. P. Denisov, V. S. Ivanov, I. Ya. Chubukov, V. N. Fedoseev, V. S. Letokhov, V. I. Mishin and S. K. Sekatsky, Hyperfine Interact. 61 (1990) 1335.

[8] J. K. P. Lee, J. E. Crawford, Z. Raut, G. Savard, G. Thekkadath, H. T. Duong and J. Pinard, Nucl. Instrum. Methods Phys. Res. B26 (1987) 444.

[9] U. Krönert, St. Becher, Th. Hilberath, H.-J. Kluge, C. Schulz, Appl. Phys. A44 (1987) 339.

[10] H.-J. Kluge, Hyperfine Interact. 74 (1992) 287.

[11] W. Paul, O. Osberghaus, and E. Fischer, Forschungsber. Wirtsch. Verkehrsministeriums Nordrhein-Westfalen No. 415 (1958); E. Fischer, Z. Physik 156 (1959) 1.

[12] W. Neuhauser, M. Hohenstatt, P. E. Toschek, and H. Dehmelt, Phys. Rev. A22 (1980) 1137.

[13] J. C. Bergquist, W. M. Itano, and D. J. Wineland, Phys. Rev. A36 (1987) 428.

[14] H. Knab, K. H. Knöll, F. Arbes, O. Becker and G. Werth, Hyperfine Interact. 74 (1992) 67.

[15] W. Nagourney, N. Yu, and H. Dehmelt, Opt. Commun. 79 (1990) 176.

[16] R. Blatt, P. Gill and R. C. Thompson, J. Mod. Opt. 39 (1992) 193.

[17] R. C. Thompson, Meas. Sci. Technol. 1 (1990) 93.

[18] R. Ifländer and G. Werth, Metrologia 13 (1977) 167.

[19] J. Rink, B. Gorski, W. Kälber, G. Meisel, H.-J. Mielke, H. Rebel, and M. Schubert, Z. Phys. A342 (1992) 487.

[20] W. Kälber, G. Meisel, J. Rink, and R. C. Thompson, J. Mod. Opt. 39 (1992) 335.

[21] L. Davey, F. Buchinger, J. E. Crawford, Y. Ji, J. K. P. Lee, J. Pinard, J. L. Vialle, W. Z. Zhao, In Proc. Int. Symp. on Resonance Ionization Spectroscopy and its Application, USA, Inst. Phys. Conf. Ser. No. 128 (1992) 305.

[22] N. Boos, F. Le Blanc, M. Krieg, J. Pinard, G. Huber, M. D. Lunney, D. Le Du, R. Meunier, M. Hussonnois, O. Constantinescu, J. B. Kim, Ch. Briançon, J. E. Crawford, H. T. Duong, Y. P. Gangrski, T. Kühl, B. N. Markov, Yu. Ts. Oganessian, P. Quentin, B. Roussiére, and J. Sauvage, Phys. Rev. Lett. 72, 2689 (1994).

[23] N. Boos, M. Krieg, G. Huber, J. Pinard, H. T. Duong, F. Le Blanc, M. Hussonnois, J. B. Kim, O. Constantinescu, B. Roussiére, J. Sauvage, Ch. Briançon, D. Ledu, R. Meunier, Th. Kühl, J. E. Crawford, Yu. Ts. Oganessian, Y. P. Gangrski, B. Gorski, B. N. Markov, in *proc. of 6th Int. Conf. on Nuclear Far From Stability & 9th Int. Conf. on Atomic Masses and Fundamental Constants, Berkastel-Kues, 1992*, Inst. Phys. Conf. Ser. No 132: Section 2, p. 217.

[24] P. H. Dawson (editor), *Quadrupole Mass Spectrometry and its Applications* Elsevier Science, Amsterdam, Oxford,New York (1976).

[25] R. E. March and R. J. Hughes, *Quadrupole Storage Mass Spectrometry*, John Wiley & Sons, New York, Chichester, Brisbane, Toronto, Singapore (1990).

[26] S. Guan and A. G. Marshall, J. Am. Soc. Mass Spectrom. 5 (1994) 64.

[27] R. D. Knight and M. H. Prior, J. Appl. Phys. 50 (1979) 3044.

[28] J. F. O'Hanlon, *A User's Guide to Vacuum Technology*, 2nd Edition, John Wiley & Sons, New York, Chichester, Brisbane, Toronto, Singapore (1989).

[29] M. D. N. Lunney, F. Buchinger and R. B. Moore, J. Mod. Opt. 39 (1992) 349.

[30] G. S. Hurst and V. S. Letokhov, Phys. Today 147 (1994) October 38.

[31] G. S. Hurst and M. G. Payne, *Principles and Applications of Resonance Ionization Spectroscopy*, Adam Hilger, Bristol, Philadelphia (1988).

[32] V. S. Letokhov, *Laser Photoionization Spectroscopy*, Academic, Orlando, New York (1987).

[33] C. L. Callender, P. A. Hackett and D. M. Rayner, J. Opt. Soc. Am. B5 (1988) 1341.

[34] I. I. Sobel'man, *Introduction to the Theory of Atomic Spectra*, Pergamon Press, Oxford, New York, Toronto, Sydney, Braunschweig (1972).

[35] H. G. Dehmelt, in *Advances in Laser Spectroscopy* Vol. 95 of *NATO Advanced Study Institute Series B: Physics*, edited by F. T. Arecchi, F. Strumia, and H. Walther (Plenum, New York, 1984).

[36] H. Schaaf, U. Schmeling, and G. Werth, Appl. Phys. (1981) 249.

[37] F. G. Major and H. G. Dehmelt, Phys. Rev. 170 (1968) 91.

[38] L. S. Cutler, R. P. Giffard, and M. D. McGuire Appl. Phys. B36 (1985) 137.

[39] J. Yoda, and K. Sugiyama, IEEE Trans. Instrum. Meas. 38 (1989) 521.

[40] A. A. Madej and J. D. Sankey, Phys. Rev. A 41 (1990) 2621.

[41] H. Lehmitz, J. Hattendorf-Ledwoch, R. Blatt and H. Harde, Phys. Rev. Lett. 62 (1989) 2108.

[42] K. Sugiyama and J. Yoda, IEEE Transactions on Instrumentation and Measurement 42 (1993) 467.

[43] M. D. N. Lunney, PhD thesis, McGill University (1992).

[44] L. S. Cutler, C. A. Flory, R. P. Giffard and M. D. McGuire, Appl. Phys. B39 (1986) 251.

[45] R. Blatt, P. Zoller, G. Holzmüller and I. Siemers, Z. Phys. D 4 (1986) 121.

[46] R. B. Moore and M. D. N. Lunney, in *Pratical Aspects of Ion Trap Mass Spectrometry Vol. II: Ion Trap Instruments*, R. E. March and J. F. J. Todd, eds. CRC Press, Boca Raton (1995).

[47] I. Siemers, R. Blatt, Th. Sauter, and W. Neuhauser, Phys. Rev. A38 (1988) 5121.

[48] H. Kopfermann, *Nuclear Moments*, Academic Press, New York (1958).

[49] P. Jacquinot, R. Klapisch, Rep. Prog. Phys. 42 (1979) 733.

[50] S. Büttgenbach, M. Herschel, G. Meisel, E. Schrödl and W. Witte, Z. Phys. 260 (1973) 157.

[51] W. G. Jin, M. Wakasugi, T. T. Inamura, T. Murayama, T. Wakui, H. Katsuragawa, T. Ariga, T. Ishizuka and I. Sugai, Phys. Rev. A52 (1995) 157.

[52] A. Anastassov, Yu. P. Gangrsky, B. K. Kul'djanov, K. P. Marinova, B. N. Markov, S. G. Zemlyanoi, Z. Phys. A348 177 (1994).

[53] J. Schecker, A. Berger, J. Das, S. Dutta, G. Gwinner, C. H. Holbrow, T. Kühl, T. Lauritsen, G. D. Sprouse, and F. Xu, Phys. Rev. A46, 3730 (1992).

[54] P. Raghavan, At. Data Nucl. Data Tables 42 (1989) 189.

[55] Y. Tanaka, R. M. Steffen, E. B. Shera, W. Reuter, M. V. Hoehn and J. D. Zumbro, Phys. Rev. C29 (1984) 1830.

[56] C. E. Moore, *Atomic Energy Levels*, NSRDS-NBS 35 Vol. III (1971).

[57] R. G. Barnes, and W. V. Smith, Phys. Rev. 93 (1954) 95.

[58] Yu. Ts. Oganessian, S. A. Karamian, Y. P. Gangrski, B. Gorski, B. N. Markov, Z. Szeglowski, Ch. Briançon, D. Ledu, R. Meunier, M. Hussonnois, O. Constantinescu and M. I. Subbotin, J. Phys. G: Nucl. Part. Phys. 18 (1992) 393.

[59] E. Browne and R. B. Firestone, Ed. V. S. Shiriey, *Table of Radioactive Isotopes* John Wiley & Sons, New York (1986).

[60] J. K. P. Lee, G. Savard, J. E. Crawford, G. Thekkadath, H. T. Duong, J. Pinard, S. Liberman, F. Le Blanc, P. Kilcher, J. Obert, J. Oms, J. C. Putaux, B. Roussière, J. Sauvage, and the ISOCELE Collaboration, Nucl. Instrum. Methods Phys. Res. B34 (1988) 252.

[61] W. H. King, *Isotope Shifts in Atomic Spectra*, Plenum Press, New York (1984).

[62] K. Heilig and A. Steudel, Atomic Data and Nuclear Data Tables 14 (1974) 613.

[63] P. Aufmuth, K. Heilig and A. Steudel, Atomic Data and Nuclear Data Tables 37 (1987) 355.

[64] F. A. Babushkin, Sov. Phys. JETP 17 (1963) 1118.

[65] D. Zimmermann, Z. Phys. A321 (1985) 23.

[66] S. A. Blundell, P. E. G. Baird, C. W. P. Palmer, D. N. Stacey, G. K. Woodgate and D. Zimmermann, Z. Phys. A321 (1985) 31.

[67] E. C. Seltzer, Phys. Rev. 188 (1969) 1916.

[68] G. Torbohm, B. Fricke, A. Rosén, Phys. Rev. A31 (1985) 2038.

[69] S. A. Blundell, P. E. G. Baird, C. W. P. Palmer, D. N. Stacey and G. K. Woodgate, J. Phys. B: At. Mol. Phys. 20 (1987) 3663.

[70] K. Finckh, A. Steudel, Z. Phys. 141 (1955) 19.

[71] P. Aufmuth, I. Henneberg, A. Siminski, and A. Steudel, Z. Phys. D–Atoms, Molecules and Clusters 18 (1991) 107.

[72] P. Aufmuth, R. Kirsch, A. Steudel and E. Wöbker, Z. Phys. D – Atoms, Molecules and Clusters 7 (1987) 153.

[73] P. Möller, W. D. Myers, W. J. Swiatecki and J. Treiner, At. Data Nucl. Data Tables 39 (1988) 225.

[74] W. D. Myers and W. J. Swiatecki, Ann. Phys. 54 (1969) 395.

[75] W. D. Myers and W. J. Swiatecki, Ann. Phys. 84 (1974) 18.

[76] H. J. Krapper, J. R. Nix, and A. J. Sierk, Phys. Rev. C20 (1979) 992.

[77] K. T. R. Davies, A. J. Sierk, and J. R. Nix, Phys. Rev. C13 (1976) 2385.

[78] F. Buchinger, J. E. Crawford, A. K. Dutta, J. M. Pearson and F. Tondeur, Phys. Rev. C49 (1994) 1402.

[79] P. Möller and J. R. Nix, At. Data Nucl. Data Tables 39 (1988) 213.

[80] P. Möller and J. R. Nix, Nucl. Phys. A361 (1981) 117.

[81] P. Möller and J. R. Nix, At. Data Nucl. Data Tables 26 (1981) 165.

[82] S. Raman, C. H. Malarkey, W. T. Milner, C. W. Nestor, P. H. Stelson, At. Data Nucl. Data Tables 36 (1987) 1.

[83] W. Fischer, H. Hühnermann, G. Krömer, and H. J. Shaäfer, Z. Phys. 270 (1974) 113.

[84] Ch. Schulz, E. Arnold, W. Borchers, W. Neu, R. Neugart, M. Neuroth, E. W. Otten, M. Scherf, K. Wendt, P. Lievens, Yu. A. Kudryavtsev, V. S. Letokhov, V. I. Mishin, V. V. Petrunin and the ISOLDE Collaboration, J. Phys. B: At. Mol. Opt. Phys. 24 (1991) 4831.